
POLITECNICO DI MILANO
DEPARTMENT of CIVIL AND ENVIRONMENTAL ENGINEERING
DOCTORAL PROGRAMME

---

# Inversion of geophysical properties

# from the EnKF analysis of satellite data over semi-arid regions

Doctoral Dissertation of:
**Ju Hyoung, Lee**

# Contents

# Prologue

I give special thanks to all of the people who academically, financially, spiritually, and emotionally supported me throughout my PhD years: Drs. Mancini, Kerr, Sakov, Su, Timmermans, Pellarin, Ravazzani, Lee in UNESCO at Paris who shared her PhD experience, the philosopher Do-ol who passionately encouraged the Korean young generations, my family who has shown a high regard for my PhD study and my friends in Milano, Toulouse, Enschede, and Africa who have spent a happy time together with me. I also thank all the immortal artists still alive in their art works including painting, literature and music and inspiring my studies, and Dr. William Tiller who profoundly inspirited me. My work was based upon the efforts of the people who sweated for establishing the local stations in Tibet, Benin, Mali, and Niger sites. I thank everyone who helped me to fulfill my research interests through the WMO international research programs and scholarships, and several anonymous journal reviewers of my manuscripts.

"The world's best designers spend 90% of their time serving the interests of the richest 10% of customers"

- Out of Poverty, by Dr. Paul Polak

# Abstract

As more and more satellites, specifically designed for hydrological monitoring, have been recently launched, the needs of satellite data utilization study are increasingly growing in the fields of hydrology, atmospheric science and geoscience. The development of inverse method is intended for such research needs. Main objective of this thesis is to propose the method inverting geophysical parameters from the measurements after filtering out the measurement errors, by means of data assimilation, specifically Ensemble Kalman Filter (EnKF). Significance of this method lies in overcoming the limitations of empirical formulations. The globally available satellite data-based inversion method appropriately addresses the characteristics in the extreme climatic conditions misestimated by means of empirical formulations. This thesis is organized as follows: EnKF was implemented with Surface Energy Balance System (SEBS)-retrieved sensible heat flux, and Synthetic Aperture Radar (SAR) and Soil Moisture and Ocean Salinity (SMOS)-retrieved surface soil moisture products. These EnKF analyses were further used as the reference data in the inverse method. The inversion of aerodynamic roughness in the SEBS model was conducted with the Tibet- Global Energy and Water cycle Experiment (GEWEX) Asian Monsoon Experiment (GAME) datasets. The inversion of soil hydraulic input variables in the Soil Vegetation Atmosphere Transfer (SVAT) model was implemented with the Tibet-GAME and GEWEX-Analyses Multidisciplinaires de la Mousson Africaine (AMMA) datasets.

Prior to an inverse modelling, the EnKF scheme for filtering out satellite errors was explored and assessed because those observation errors may adversely affect the parameter inversion minimizing a mismatch between simulation and observation. Two different schemes of stationary and sequential EnKF were compared to examine whether observation error correction can replace the time-evolution of sequential ensemble. Because the stationary ensemble-based Ensemble Optimal Interpolation (EnOI) scheme is a computationally cost-effective but suboptimal approach, the two-step stationary EnKF scheme empirically defining the observation errors by means of L-band Microwave Emission of the Biosphere (L-MEB) radiative transfer model-based SMOS L2 processor was suggested, in contrast to a sequential EnKF assuming global constant *a priori* error. The result suggested that the sequential EnKF scheme consuming a longer record of satellite data may not be required if the SMOS brightness temperature errors in EnOI are empirically adjusted. The operational merit of the two-step stationary EnKF scheme lies within a short analysis time step, when compared with the Cumulative Distribution Functions (CDF) matching requiring a long record (usually, at least one year) of satellite data and the sequential EnKF scheme. Additionally, there is no need to assume a slow evolution or a global constant for the observation error parameter in the observation operator of EnKF or to define the length of the localising function for reducing sampling errors.

The EnKF analysis of heat flux and soil moisture was further employed for inverting geophysical properties. The first geophysical parameter inverted was aerodynamic roughness height. It is a key input required in various models such as land surface model, energy balance model or weather prediction model. Although the errors in heat flux estimations are largely dependent on an accurate optimization of this parameter, it remains uncertain, mostly because of non-linear relationship of Monin-Obukhov Similarity (MOS) equations and uncertainty in the vertical characterization of vegetations. Previous studies determined aerodynamic roughness using a traditional wind profile method, remotely sensed vegetation index, a minimization of cost function over MOS equations or a linear regression. However, these are the complicated procedures presuming high accuracy for other related parameters embedded in MOS equations. In order to avoid such a complicated procedure and reduce the number of parameters in need, a new approach inverting aerodynamic roughness height from the EnKF-analysis of heat flux was suggested. To the best of knowledge, no previous study has applied EnKF to the estimation of aerodynamic roughness. In adition, the inversion was applied for soil hydraulic input variables of SVAT model. The performance of SVAT model is largely constrained by uncertainties in spatially distributed soil and hydraulic information, which is mainly because any Pedo-Transfer Function (PTF) estimating soil hydraulic properties is empirically defined. Accordingly, its applicability is limited. To overcome this limitation, a new calibration for inverting soil hydraulic variables from EnKF-analyzed SAR and SMOS surface soil moisture products over the Tibet-GAME and the AMMA datasets was suggested. When inverted surface variables were used, these calibrated SVAT model demonstrated a better match with the field measurement and a non-linear relationship between surface and root zone soil moisture.

This thesis is organized as follows. In Chapter 1, the site description and research background are introduced. In Chapter 2, EnKF is explored for acquiring the reference data used in parameter inversion. In Chapter 3, the inversion of aerodynamic roughness from the EnKF analysis of heat flux is presented. In Chapter 4, the inversion of land surface variables from the EnKF analysis of soil moisture is illustrated. The conclusion and summary are provided in Chapter 5.

CHAPTER 1

# Introduction

## 1.1. Research significance of the semi-arid regions

There are several ways for estimating the same surface variable. One retrieves the signals of satellite. Another simulates a model. The other goes to the field and measures that. For various reasons, heat flux, especially latent heat and soil moisture in arid regions are significantly misestimated by all the methods of field measurement, model and satellite retrieval. First, it was previously argued that the latent heat measured by the eddy covariance method contains a large degree of errors, because the quantity of humidity or vapor pressure in dry soils is too small, compared to temperature gradients, to accurately estimate them, demanding a higher degree of measurement accuracy than the wet conditions (Boulet et al., 1997, Jochum et al., 2005, Prueger et al., 2004, Weaver et al., 1992). Additionally, the dry soils are the main source of brightness temperature errors of satellite, usually reporting a large discrepancy from the field measurements (Escorihuela et al., 2010). The strong soil moisture gradients generated by rain fallen on dry soils are also the source of large errors in satellite retrieval algorithm. Finally, uncertainty in soil and hydraulic properties in dry and sandy soils largely limits the performance of the SVAT land surface model. The original land surface parameterization did not consider the contribution of vapor phase transfer in dry soils (Braud et al., 1993). The soil property such as wilting point determined from soil maps-based PTFs is largely uncertain in dry and sandy soils, being significantly propagated to the

estimation of input parameters (Pellarin et al., 2009). Therefore, the arid regions are the very condition that requires the data assimilation in order to mitigate several errors arising from both model and measurement. This thesis suggested the inversion of parameters from the data assimilation final analysis, after filtering out the errors often found in such a climatic condition. A site description of each arid region is provided in following Sections.

### 1.1.1. The Naqu region in cold and semi-arid Tibetan Plateau

The Tibetan Plateau as the source of all large rivers in Asia plays a major role on land surface circulation all over the Asian continents. This region is also called the 'Third Pole', because it is the world's highest and largest cryosphere, except the North and South Poles (Ma et al., 2009). The climate changes and hydrological processes due to the recent glacial retreat have received much attention from a broad range of international scientific community. The experiments are based upon one of Tibetan Observation and Research Platform (TORP) under the frame of GEWEX, consisting of 21 research and 16 observation stations.

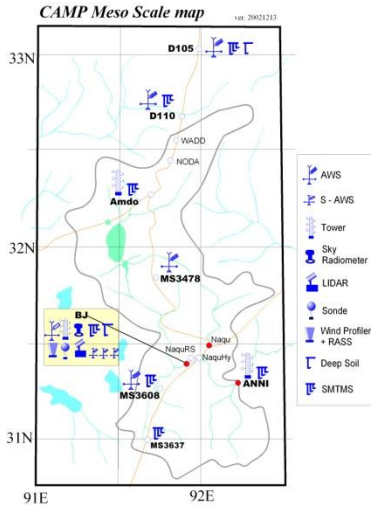


Figure. 1. Observation system of the GAME–Tibet experiment (Ma et al., 2009)

As denoted as "BJ" in Figure 1, this local station is situated at a latitude of 31.3686 N and a longitude of 91.8987 E (Ma et al., 2009). This area is the flat plain sparsely surrounded by rolling hills. The approximate elevation is 4509 m above the mean sea level. The soil contains large amounts of organic matter, and is covered with gravel at the soil surface (Su et al., 2011). Soil texture was observed as loamy sand. The soil layer is well-drained but has the underlying impermeable permafrost layers. This semi-arid region is subject to intense rainfall (300 mm, approximately) during the Asian Monsoon season. It is the cold area showing the air temperature of usually less than 10℃ (van der Velde, 2010). The main land cover is the grassland. In 2006, at BJ station, several meteorological datasets were collected, such as wind

speed, relative humidity, air and land surface temperatures, soil temperature, incoming and outgoing short wave and long wave radiation, rainfall, and soil moisture contents at depths of 0.05 and 0.20 m (van der Velde et al., 2009). Soil moisture profile was measured with 0.10 m long ECH2O impedance probes manufactured by Decagon Devices (type: EC-10) (Su et al., 2011). Measurement error was previously reported as 0.029 m3/m3 (van der Velde, 2010). Rainfall measured around this station was previously shown by (Lee et al., 2012b). In addition to a BJ station, they have additional soil moisture station named "Naqu", which measured surface soil moisture at the depth of 0.025 m (van der Velde et al., 2012). It resided beside a BJ station. Rainfall measured in this station was previously shown (Lee et al., 2012b).

The Naqu region usually exhibits a dramatic change in the vertical gradients of temperature and humidity in the atmospheric boundary layer (ABL) around onsets of Monsoon period (Sun et al, 2006, 2007). As ground surface temperature increases with a decrease in air temperature, convective activity and sensible heating is accelerated, resulting in Monsoon climate (Wen et al., 2010). Around this time, local grass proliferates and LAI starts increasing at the onsets of Monsoon, and decreases in winter, while albedo conversely alters. Accordingly, aerodynamic roughness parameters in this site make a seasonal change, being governed by various aerodynamic and thermodynamic characteristics. Aerodynamic roughness over Tibetan plateau was explored by various approaches such as traditional wind profile method using eddy covariance instruments, flux-variance method, and vegetation index (Choi et al., 2004, Lee et al., 2012a, b, Ma et al., 2002, 2005, 2008, Su et al., 2002, 2005, Yang et al., 2003, 2008).

1.1.2. The Benin and Niger sites in hot and semi-arid West Africa

The Sahara is the largest desert in the world, except the polar areas. Strong latent heat released from the Inter-Tropical Convergence Zone (ITCZ) including West Africa is one of the major solar heating sources on the globe. It is related to a regional circulation such as rainfall in West Africa and Atlantic hurricane frequency (AMMA-ISSC, 2010). Owing to the Meso-scale Convective System (MCS) developed by a large potential temperature gradient between the Sahara on the North and the Gulf of Guinea on the South, the rainfall in West Africa exhibits a negative gradient from the South to North, resulting in the development of the similar spatial variability in vegetation and soil moisture (Boulain et al., 2009; Ramier et al., 2009). The northeasterlies transport dry air to the Sahara, while the southwesterlies from the Atlantic Ocean deliver moisture to the Sudanian Savannas (Descroix et al., 2009; Lebel et al., 2010). Other large-scale factors influencing the West African Monsoon (WAM) include Azores anticyclone over the Atlantic Ocean, the Libyan anticyclone over the Inter-Tropical

Convergence Zone (ITCZ) and Saharan thermal heat-low as well as the cold-tongue (a rapid decrease of tropical eastern Atlantic sea surface temperature, coinciding with the onsets of WAM) being developed around the Gulf of Guinea (Lebel et al., 2009, 2010; Nguyen et al, 2011; Peugeot et al., 2011; Séguis et al., 2011).

To investigate the influence of the land surface condition on the climate change in West Africa, several research works have been conducted under the Analyses Multidisciplinaires de la MoussonAfricaine Couplage de l'AtmosphèreTropicale et du Cycle Hydrologique (AMMA- CATCH) frame (Boulain et al., 2009; Cappelaere et al., 2009; Descroix et al., 2009; Lebel et al., 2009; Mougin et al., 2009; Ramier et al., 2009). Other studies examined the moisture transport and atmospheric interaction on the meso to synoptic scale (Lebel et al., 2010; Peugeot et al., 2011; Séguis et al., 2011). In this context, Taylor et al. (2011) addressed the significance of soil moisture spatial patterns on meso to synoptic scale. The boundary layer convection activity largely enhanced in dry soils diminishes the intensity of the African Easterly Jet (AEJ, the easterlies with the maximum seasonal mean wind speed), which consequently weakens the development of MCSs. On the other hand, the latent heat indirectly influenced by wet surface conditions contributes to the Sahelian rainfall, which is further related to Atlantic hurricane frequency (AMMA-ISSC, 2010). In short, a spatial distribution of soil moisture conditions largely influences the development of energy transfer as well as WAM. Thus, in terms of moisture transport, atmospheric circulation and weather forecast, the acquisition of reliable soil moisture spatial patterns on the meso-scale is very significant in West Africa. However, several previous studies found that there are several limitations in directly applying the SVAT scheme into very dry and sandy soils. In order to simulate the meso-scale soil moisture in Niger, Pellarin et al. (2009) re-calibrated the soil and hydraulic parameters of Interactions between Soil-Biosphere-Atmosphere (ISBA) land surface model with several reference data such as Advanced Microwave Scanning Radiometer for Earth Observing System (AMSR-E) data and MSG-SEVIRI (Meteosat Second Generation – Spinning Enhanced Visible and Infra-red Imager) land surface temperature products. By minimizing a mismatch between simulated and observed brightness temperature, they re-calibrated equilibrium surface volumetric soil moisture $\theta_{geq}$ and wilting point information originally formulated by PTFs (Montaldo and Albertson, 2001). Braud et al. (1993) and Giordani et al. (1996) also found that soil coefficient parameterization in ISBA models needs to be modified, due to vapour phase transfer in dry soils. They newly formulated the soil surface variable $C_1$ as functions of land surface temperature and wilting point. However, some recent studies suggested that a validity of the ISBA soil coefficient parameterization by Braud et al. (1993) and Giordani et al. (1996) is limited. Due to the overestimation by these previous studies, Juglea et al. (2010) re-calibrated several soil hydraulic parameters according to Cosby et al. (1984) and Boone et al. (1999), and could finally make a better estimation of

soil moisture. In practical terms, because such recalibration approach is inefficient, Calvet and Noilhan (2000) previously proposed a renormalization method, and successfully retrieved root zone soil moisture by performing a variational assimilation with surface soil moisture data.

To acquire spatially distributed soil moisture data over West Africa, several studies previously employed the satellite. Zribi et al. (2009) validated the 11 years of European Remote Sensing (ERS) scatterometer-retrieved surface soil moisture data over the Sahelian region with the field measurements and Advanced Synthetic Aperture Radar (ASAR) products. The results were in good agreements, and also well-matched with precipitation activity. Pellarin et al. (2009) also retrieved meso-scale soil moisture in West Africa. They employed the brightness temperature measurements from Advanced Microwave Scanning Radiometer for Earth Observing System (AMSR-E) and the land surface temperature measurements from Meteosat Second Generation (MSG) for calibrating a land surface model by minimizing a mismatch between the measurements and the simulations with microwave emission models. Saux-Picart et al. (2009) compared the ASAR soil moisture and MSG land surface temperature measurements with the soil moisture field measurements in the Niger site. They concluded that it is more effective to use MSG land surface temperature data for retrieval of the surface soil moisture than ASAR products. They suggested the vegetation effect and the under-representation of landscape heterogeneity as the cruxes of ASAR-retrieved surface soil moisture products.

| Site | Longitude (° décimal) | Latitude (° décimal) | Profondeur (cm) | Commentaire |
|---|---|---|---|---|
| Wankama 1 | 13°38.853' N | 2°38.022' E | 5, 5 | Jachère |
| Wankama 2 | 13°38.628' N | 2°37.805' E | 10-40, 40-70, 70-100, 105-135 | Mil |
| Banizoumbou | 13°31.294' N | 2°37.737' E | 5, 5 | Mil |
| Tondikiboro | 13°33'N | 2°42'E | 5, 5, 10-40, 40-70, 70-100, 105-135 | Brousse tigrée |


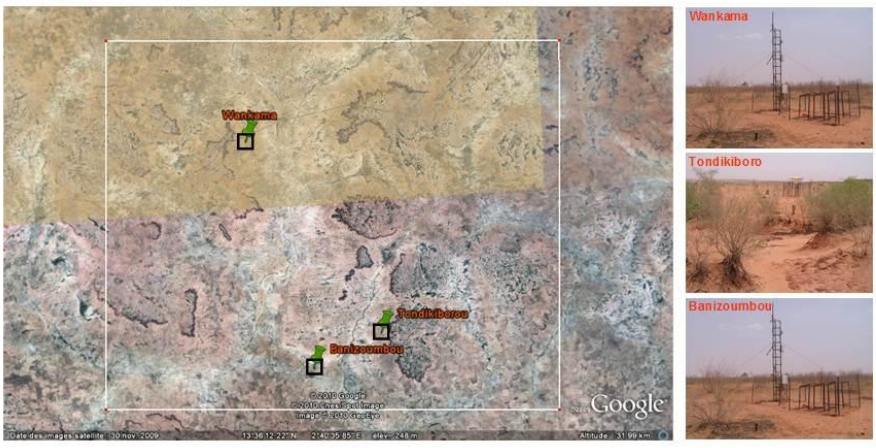

(a)

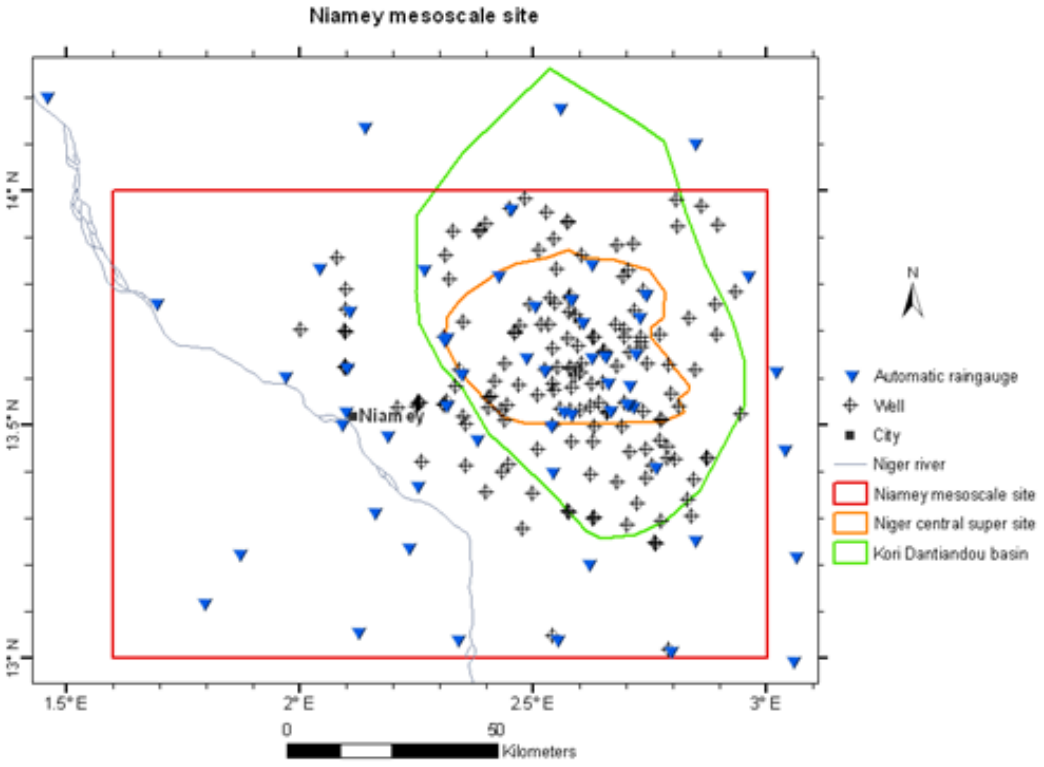


(b)

Figure 2. The Niger region: (a) Wankama site; (b) meso-scale network

To further address those issues stated above, this study have monitored the soil moisture with the AMMA-CATCH (Couplage de l'Atmosphère Tropicale et du Cycle Hydrologique) field campaign data. They were located in the Niger (Wankama region, 50 km East of Niamey) and Benin (Djougou region) sites, as shown in Figure 2 and 3, respectively. A detailed description of the rain gauge network and soil moisture measurement was provided by Cappelaere et al. (2009) for the Niger site, and by Séguis et al. (2011) for the Benin site.

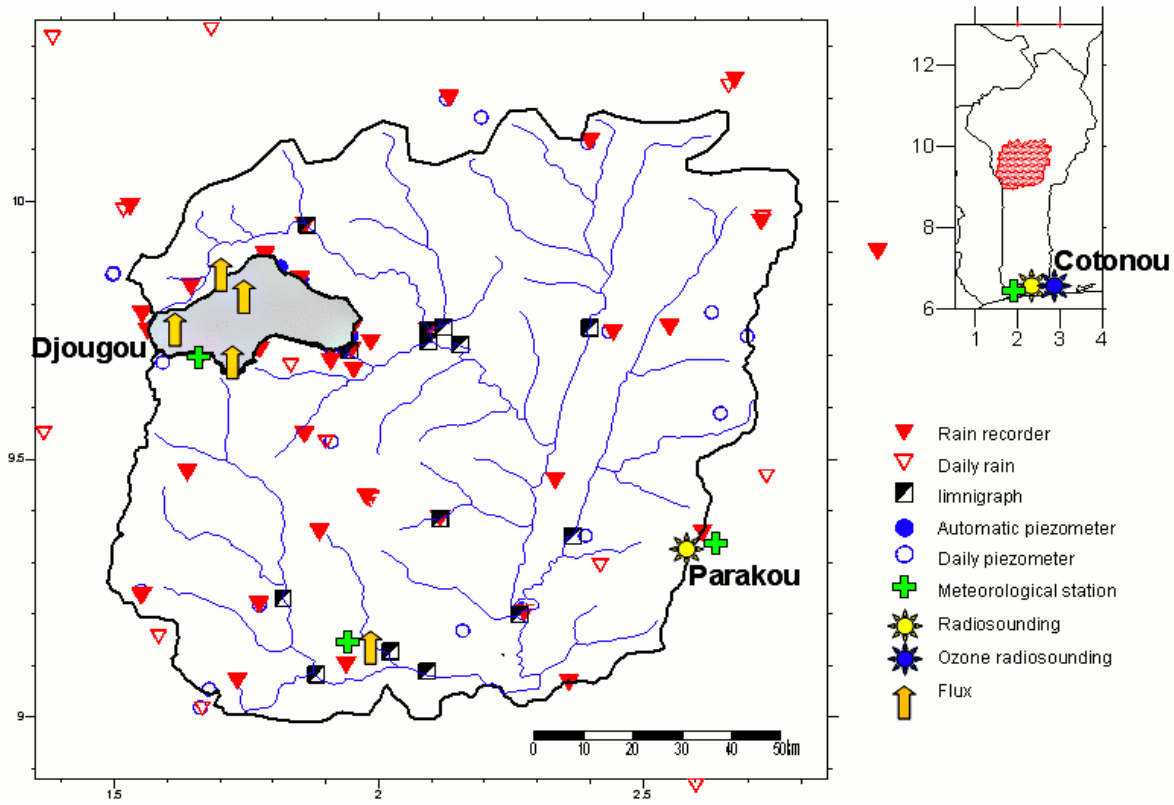


Figure 3. The Benin region: Djougou sites

## 1.2. Significance of inverse method for parameter estimation

Aerodynamic roughness height is a significant parameter to a variety of models such as numerical weather prediction model (e.g. AROME), wind atlas model (WAsP), land surface model (e.g. NOAH, CLM), or other hydrological models. The error in the parameter can be propagated through the model and become a major error source in the model output. The estimation of aerodynamic roughness is usually performed in neutral or near-neutral conditions when turbulent transfer coefficient for humidity and temperature is considered to be equivalent, while other researchers suggest to include all the atmospheric stability conditions or to use turbulent data under unstable and highly convective condition only (Kohsiek et al., 1993, Yang et al., 2003). However, in several cases, the factor of atmospheric stability is not readily corrected by Monin-Obukhov similarity (MOS) formulations, on account of some measurement error or inapplicable assumption of horizontal surface homogeneity – for example, in case of sparsely vegetated area, less equilibrated boundary layer can be developed above the surface (Foken and Wichura, 1996, Prueger et al., 2004). Accordingly, such approach produces high standard deviation and scatteredness in aerodynamic roughness height estimates (Yang et al., 2008).

To circumvent these uncertainties in momentum flux attributes and to infer aerodynamic roughness height at large scale from geometric characteristics, several previous studies employed remotely sensed Vegetation Index (VI) (e.g. LAI or NDVI). However, VIs also have a degree of uncertainty in determination of the aerodynamic roughness. First, VI tends to saturate at high LAI values above 3 to 4. Due to reflectance, cloud effect and landscape misclassification, remotely sensed LAI is sometimes attenuated by 41%, losing vertical characteristics of vegetation (Yang et al.,2006). Additionally, according to nutrient nourishment or vegetation species, vegetation has different sensitivities to VI so that each different vegetation species presents different ranges of maximum and minimum VI over similar aerodynamic roughness height. For instance, some tall coniferous trees have similar LAI level with low crops, while some low crops such as rice indicate high LAI values of 5 to 6 over 1 to 2 m high canopy (Chen et al., 2005). In case of deciduous forest that its chlorophyll contents diminish in the fall, LAI thus decreases such that aerodynamic roughness can be underestimated unlike tropical evergreen forest. Therefore, parameterization relying on remotely sensed Vegetation Index only is sometimes not agreeable with field observed aerodynamic roughness, especially as it is very difficult to retrieve canopy height with remote sensing measurements alone. This uncertainty stemming from the use of VI can be propagated into the roughness height estimation, which can lead to a large error in heat flux estimation. Accordingly, there is a limit to VI approach.

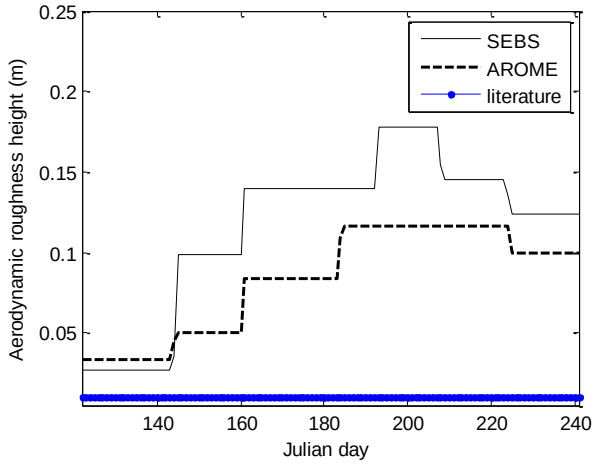


Figure 4. Bias in aerodynamic roughness height over short grassland: from AROME (i.e. MODIS LAI/6), original SEBS and literature value (Beljaars et al.,1983)

Figure 4 is an illustrative example of the bias associated with several aerodynamic roughness estimations. Not only does remotely sensed VI have uncertainty but literature

value also contains a degree of uncertainty arising from low temporal variation. Although MODIS NDVI in BJ station has changed from 0.17 to 0.53 and MODIS LAI has evolved from 0.2 to 0.7 from Julian day of 140 to 240, aerodynamic roughness from literature or landscape map is time-invariant, neglecting its vegetation effect by Monsoon activity. In addition, the AROME and SEBS model overestimated this parameter by 5 times or more. If selecting a larger domain size than the one used in Figure 4, the aggregated VI estimation changed by 0.2 for the NDVI, and by 1.0 for the LAI, implying that the VI aggregation (or resampling) regieme may also influence on aerodynamic roughness estimation. On the other hand, Yang (2003) argued that heat transfer is also affected by ground surface characteristic such as temperature difference between land surface and air or momentum flux probably more than vegetation effect, according to dual-source model study over energy partition. In the same context, Tuang (2003) attempted to find optimal aerodynamic roughness in MOS theory using a linear regression between momentum velocity or potential temperature and displacement height, while Ma (2000) minimized a cost function over potential temperature, wind velocity, and heat flux (Yang et al, 2002). However, this approach is affected by measurement errors of several parameters (i.e. wind velocity, stability correction parameter, potential temperature, or Obukhov length etc) involved in MOS formulations. For example, Obukhov length estimated by MOS formulation iteration has sometimes a discrepancy from eddy covariance methods. Therefore, the inverse method for estimating the aerodynamic roughness can be a very promising method to innovatively overcome those limitations.

This thesis also inverted the SVAT model input used for the estimation of soil moisture. Soil moisture is a very important climatic state variable for hydrological and meteorological circulation. Although the spatial distribution of surface soil moisture has been successfully estimated from satellite data, the estimation of root zone soil moisture is not straightforward. Some previous remote sensing studies have used the proxies such as vegetation index, latent heat or precipitation data from low resolution data of passive microwave sensors, while others have employed a simple exponential filter to infer the root zone soil moisture content directly from remotely sensed surface soil moisture (Dunne and Entekhabi, 2006; Anguela et al., 2008; Crow et al., 2008; Loew et al., 2009). However, the applicability of such approaches are limited in that a direct use of remotely sensed surface attributes or single proxy values are incapable of accounting for complex interactions between atmospheric exchanges and heat flux in deep soil layers (Martinez et al., 2008; Lee et al., 2012a). Especially, if the soil layer is highly stratified or vertically heterogeneous in terms of soil and hydraulic properties, the root zone soil moisture cannot be directly predicted from the surface soil moisture or other remotely sensed surface attribute.

To account for complex energy-water interactions that occur as a result of soil, vegetation, and atmospheric exchange, the SVAT model can be employed to estimate the soil moisture profiles. The main obstacle of this model is that it requires several spatially distributed soil hydraulic input parameters (Beven and Franks, 1999). The most common approach in the acquisition of this information is to utilize clay and sand maps of ECOCLIMAP, based upon Food and Agriculture Organization (FAO) datasets (Champeaux et al., 2005). They are widely applied to the empirical PTFs, due to the global availability of the FAO soil maps and the simplicity of its implementation (Noilhan and Mahfouf, 1996). However, this approach has several limitations. Firstly, previous studies have cast doubt on whether any PTF can predict spatially distributed soil hydraulic properties due to the obscure relationships between soil survey data and soil hydraulic properties (Schaap et al., 1998; Gutmann and Small, 2007; Brimelow et al., 2010). This is because any PTF was empirically parameterized so that they usually shows mis-estimation, when applied to other extreme climatic conditions or different soil compositions. Other uncertainties also exist in the FAO soil map itself for various reasons, such as limited surveys, misclassifications, coarser spatial resolutions for the application of SAR data, or inconsistencies with other resources (Maria and Yost, 2006). Finally, the SVAT land surface parameterizations suggested by Noilhan and Mahfouf (1996) rely solely on the clay fraction. However, the high organic matter content present at the Naqu site also influences the estimation of soil hydraulic properties, as numerous previous studies have discussed the contribution of other factors such as organic matter or bulk density (Hall et al., 1977; Batjes, 1996; Timlin et al., 1996; da Silva and Kay, 1997; Mayr and Jarvis, 1999; Federer et al., 2003; Saxton and Rawls, 2006; Brimelow et al., 2010; Reichert et al., 2010).

One potential strategy to overcome the limitations and uncertainties described above would be to determine the spatially distributed land surface properties without relying on the empirical PTFs, site-specifically defined. For this reason, a stochastic inverse method has been previously suggested and applied to several ground water transport and land surface model studies. Here, an inverse method is referred to as an optimization that minimizes mismatches between observed and simulated values (Zhou, 2011; Li et al., 2012). Gutmann and Small (2007) suggested that an inverse method is appropriate for estimating several land surfaceinputs in the NOAH land surface model. In that study, an inverse method was used to select the very soil hydraulic parameters, from several other candidates, that provided the best fit to field measurements. These results were also compared with the soil texture approach discussed above. They concluded that an inverse method was better than soil texture approach. They also suggested that an inverse method could be applied to remotely sensed soil moisture data in the future. Hendricks-Franssen and Kinzelbach (2008) and (2009) used an EnKF for a Monte-Carlo type inverse calibration so that they calibrated the input

parameters of transient flows or transport model with reduced computational costs. For the establishment of ensemble pools, they stochastically produced several input parameters such as hydraulic conductivity and porosity. Kunstmann (2008) and Intsiful and Kunstmann (2008) also applied an inverse stochastic model to the calibration of several SVAT input parameters including aerodynamic roughness height, and soil moisture at wilting point, and field capacity, as in SVAT-PEST (Parameter EStimation Tool) (Goegebeur and Pauwels, 2007). Pauwels et al. (2009) successfully retrieved several land surface parameters of land surface model from SAR surface soil moisture.

In contrast to several previous hydrological studies that applied an EnKF into the determinations of state variables such as surface soil moisture or land surface temperature, this study attempted to adopt the EnKF scheme to the rarely explored topic of parameter estimation (Margulis et al., 2002; Reichle et al., 2002, Reichle, 2008; Li et al., 2010). EnKF was used to reduce any potential satellite retrieval errors or field measurement errors that may be adversely propagated into parameter estimation and to adjust any systematic difference between the observations and land surface model structures.

CHAPTER 2

# Ensemble Kalman filter methods

## 2.1. Data assimilation

Soil moisture is an important climatic variable governing the partitioning of heat flux and water circulation (Margulis et al., 2002). On the meso-scale, to predict the monsoon precipitation, latent heat, or sometimes even hurricane, a spatial pattern of soil moisture should be accurately estimated (AMMA-ISSC, 2010; Taylor et al. 2011). The best way to acquire the spatial analysis is to exploit the satellite data, due to its global accessibility. Margulis et al. (2002) and Reichle (2008) discussed that remote sensing data is interfered by the effects of vegetation, fluctuations in surface elevation, precipitation occurrence, soil texture, topography, land use, and a variety of meteorological variables, suggesting the needs for soil moisture data assimilation (Evensen, 2003; Reichle et al., 2002; Reichle, 2008). Huang et al. (2008) employed the EnKF method to assimilate *in-situ* surface soil moisture field measurement, and low-frequency passive microwave brightness temperature data into the Simple Biosphere Model (SiB2) land surface model. They applied their EnKF scheme to the Tibetan Plateau, and found that EnKF significantly improved the soil moisture estimation, and successfully dealt with a non-linear relationship between model operator and observation operator. Margulis *et al*. (2002) updated the NOAH land surface model states with the L-band passive microwave brightness temperature data. They have assessed the performance of

EnKF with the innovation, and finally concluded that EnKF significantly improved the soil moisture estimation better than the open-loop (Dunne & Entekhabi, 2006). Galantowicz *et al.* (1999) assimilated the L-band radiobrightness temperature data into a soil heat and moisture diffusion model for the better estimation of surface soil moisture. They suggested that a sequential Kalman filter is an effective way that can replace an inverse algorithm to relate brightness temperature to physical parameters, because the Kalman Filer compares the predicted simulations with the observations through innovation steps. Crow et al. (2008) assimilated the remotely sensed thermal data as soil moisture proxy into a water balance model, and concluded that they improved the estimation of root zone soil moisture (Dunne & Entekhabi, 2006, Hoeben & Troch, 2000, Loew et al., 2009). Houser et al. (1998) assimilated the microwave radiometer data into a TOPmodel-based Land-Atmosphere Transfer Scheme (TOPLATS). They developed the four-dimensional data assimilation scheme to relate the surface attributes to sub-surface layers, and finally improved the estimation of root zone soil moisture.

Some studies applied it to various problems such as a correction of rainfall estimation or a prediction of run-off (Crow & Ryu, 2009; Reichle, 2008). Others conducted the in-depth studies relative to *a priori* error covariance. To optimize *a priori* error covariance, de Lannoy et al. (2009) introduced an adaptive covariance correction method to an EnKF. They estimated the adaptive second-order *a priori* error for the purpose of tuning the variance, while they assimilated the soil moisture field measurements to the Community Land Model. Kumar et al. (2008) used two different land surface models (i.e., Catchment and NOAH) to compare the performance of soil moisture EnK scheme. It was found that the EnKF results were just comparable, suggesting the significance of the accurate specification of the erroneous parameters and model representation. Several EnKF studies applied to the non-hydrological fields also previously discussed *a priori* error covariance or introduced forecast-model bias correction methods (Dee & da Silva, 1998; Keppenne et al., 2005; Zhang & Anderson, 2003).

### 2.2. Performance of sequential EnKF

In application of SAR backscattering to soil moisture, *a priori* roughness information is required as a key input of backscattering simulation models such as the Integral Equation Model (IEM). In the backscattering simulation models, roughness is usually described as the surface root mean square (RMS) height, the correlation length, and an AutoCorrelation Function (ACF) (Verhoest et al., 2008). They are usually estimated from the field measurements of surface height. However, it is well-known that it is difficult to accurately estimate soil roughness (Lievens et al., 2009; Mattia et al., 2003 & 2006, Ulaby & Batlivala,

1976). Contact instruments such as a pin profiler or a meshboard disturb the land surface before achieving the accurate roughness and are affected by parallax errors or profile lengths (Mattia et al., 2003). Non-contact instruments such as a laser, photogrammetry, acoustic backscatter, infrared, and ultrasonic equipment are often interfered with other external sources (e.g. wind effects), and sometimes cannot distinguish the effects by topography from by optical reflectivity (Huang & Bradford, 1992). Additionally, SAR surface soil moisture data is currently operational on a global scale. Accordingly, the local field measurements of soil roughness may be less applicable to a larger spatial scale, due to a scale problem (Lievens et al., 2009; van der Velde, 2010, van der Velde et al., 2012). Thus, as usual, *a priori* assumption is made for roughness information such as RMS height, correlation length and ACF, considering them as known inputs in backscattering simulation models (Rahman et al., 2007). After a thorough literature review for soil moisture retrieval from SAR, Satalino *et al*. (2002) concluded that the SAR retrieval errors are mainly due to roughness (i.e. inversion error), whose variations largely change a relationship between soil moisture and backscattering coefficient. They estimated the SAR retrieval errors arising from roughness to be approximately 6 % in case of ERS instrument.

Objective of this Section is to quantitatively address the roughness inversion errors in SAR retrievals, and to assess to what extent the sequentiality of the EnKF ensembles can solve the roughness errors. This study will be useful in an operational sense. If the performance of EnKF is just comparable to EnOI, then EnOI can be recommended to save a computation cost. In addition, the findings of this Section would be useful for other satellite data assimilation studies since it was previously discussed that the performance of data assimilation may be limited if the satellite observation is significantly contaminated with undefined errors (Reichle, 2008). This Section is organized as follows. In Section 2.2.1, the site description and data source are presented. In Section 2.2.2, two different EnKF schemes are described. The detailed method for SVAT model used as the forecasts is provided in Section 4.2. In Section 2.2.2.3, the AIEM retrieval algorithm required for SAR soil moisture observation is described. The results and discussions are provided in Section 2.2.3, where a comparison between sequential EnKF and stationary EnKF is provided at a point-scale and at a SAR spatial scale, after characterizing the roughness error in SAR data.

### 2.2.1. Site description & SAR data

The study domain was defined as an area of 3 km × 3.5 km around the BJ station described in Section 1.1.1, and Figure 1. For the retrievals of surface soil moisture, Environmental Satellite (ENVISAT) Advanced Synthetic Aperture Radar (ASAR) data operated at C-band (5.331 GHz) and various incidence angles (16–43°) was used. The VV-

polarized wide swath 1P mode image has a medium resolution of 150 m and a grid spacing of 75 m. This corresponds to more than 4000 SAR pixels approximately in the study domain defined above. The ASAR data was acquired approximately at 3:50 am (UTC) for descending mode and at 3:50 pm (UTC) for ascending mode on Day of Year (DoY) 216, 219, 221, 222, and 224. These days were selected because they were under optimal conditions for roughness study. During that period, the study site was on the driest condition during the season, according to the field measurements. The backscattering measurements acquired for these days were considered to be governed by roughness rather than dielectric constant.

2.2.2. EnKF schemes

2.2.2.1. Sequential EnKF

A detailed description of EnKF theory and algorithm itself was previously provided (Anderson, 2001; Evensen, 2003; Margulis et al., 2002). In this paper, as the alternative of the standard EnKF, we focused on the Deterministic EnKF (DEnKF) without making observation perturbations. The difference between this and the standard EnKF is briefly illustrated here.

First, the state ensemble in the standard EnKF is updated with the following relationship.

$$x^a = x^f + \mathbf{K}(d - \mathbf{H}x^f) \qquad (1\text{-}1)$$

where, $x^a$ is the analysis, $x^f$ is the forecast, **K** is the Kalman gain to determine the relative weights between the forecasts and the observations, **D** is the perturbed synthetic vector of observation d, and **H** is the observation sensitivity matrix. **K** is further formulated as follows:

$$\mathbf{K} = \mathbf{P}^f\mathbf{H}^T(\mathbf{H}\mathbf{P}^f\mathbf{H}^T + \mathbf{R})^{-1} \qquad (1\text{-}2)$$

where, $\mathbf{P}^f$ is the forecast error covariance matrix, and **R** is the observation error covariance matrix. Instead of solving equations, the standard EnKF uses a Monte Carlo method for estimating error covariance **P**, as follows (Zhang & Anderson, 2003):

$$\mathbf{P} = \frac{1}{m-1}\sum_{i=1}^{i=m}\left(X_i - x\right)\left(X_i - x\right)^T = \frac{1}{m-1}AA^T \quad \text{where, } i=1\ldots m \qquad (1\text{-}3)$$

where, x is ensemble mean $x = \frac{1}{m}\sum_{i=1}^{i=m} X_i$, $m$ is the ensemble size, $X_i$ is the $i^{th}$ ensemble

member of model states, and A is the ensemble anomaly (e.g., $A_i=X_i-\mathbf{x}$). The standard EnKF has a premature reduction problem in ensemble spread without adding synthetic perturbations **D,** leading to the underestimation of error covariance. The DEnKF solves such an underestimation problem, without the random perturbation of observations. If halving **K**, one matches the prior model error covariance with a theoretical form of the standard Kalman filter. In other words, if the observations are not perturbed (i.e. **D**=0), and the half of Kalman gain (i.e. $\frac{1}{2}\mathbf{K}$) is used, the prior error covariance and anomaly become as follows (Sakov & Oke, 2008; Whitaker and Hamill, 2002):

$$A^a=A^f-\frac{1}{2}\mathbf{K}\mathbf{H}A^f \qquad (1\text{-}4)$$

$$\mathbf{P}^a=(1-\mathbf{K}\mathbf{H})\,\mathbf{P}^f+\frac{1}{4}\mathbf{K}\mathbf{H}\mathbf{P}^f\mathbf{H}^T\mathbf{K}^T \qquad (1\text{-}5)$$

This analyzed model error covariance in equation (1-5) has the additional term $\frac{1}{4}\mathbf{K}\mathbf{H}\mathbf{P}^f\mathbf{H}^T\mathbf{K}^T$ to a theoretical form of the standard Kalman filter $(1-\mathbf{K}\mathbf{H})\,\mathbf{P}^f$. It was previously suggested that the formula of DEnKF in (1-5) showed a better performance with a less computational cost and a better convergence than the standard EnKF (Sakov & Oke, 2008; Sakov et al., 2010; Sun et al., 2009).

2.2.2.2. Stationary EnKF

The EnOI scheme was devised from EnKF (Counillon & Bertino, 2009; Evensen, 2003). The theoretical basis is identical with the sequential EnKF, except that EnOI uses the stationary ensembles, assuming their statistical validity over a given time.

2.2.2.3. The AIEM retrieval for the SAR soil moisture observations

The retrieval algorithm was carried out by comparing the simulated backscattering with the measurements. To acquire the ASAR-measured backscattering, the images were calibrated with the Next ESA SAR Toolbox (NEST) software (Laur et al., 2004). They were terrain-corrected (SRTM) and processed with multi-look correction and speckle filtering. In parallel with these ASAR measurements, an Advanced Integral Equation Method (AIEM) model also simulated the backscattering coefficients for a wide range of roughness conditions and incidence angles as well as dielectric constant values generated in Look Up Table (LUT) (Fung, 1994, Shi et al., 1997, Ulaby et al., 1982, van der Velde, 2010, van der Velde et al.,

2012). In detail, the AIEM model computes the backscattering coefficients $\sigma^o$ as the sum of the Kirchhoff, the complementary, and the cross term, as follows (Chen et al., 2003, Shi et al., 1997, Huang et al., 2008):

$$\sigma_{pp}^{o} = \frac{k^2}{2}\exp[-s^2(k_z^2 + k_{sz}^2)]\sum_{n=1}^{\infty} s^{2n}\left|I_{pp}^{n}\right|^2 \frac{W^n(k_{sx}-k_x, k_{sy}-k_y)}{n!} \quad (2\text{-}1)$$

Where, $I_{pp}^{n}$ is a function of the Kirchhoff coefficient, and complementary field coefficient of re-radiated fields propagated through two different mediums, $W^n$ is the Fourier transform of the $n^{th}$ power of the normalized surface correlation function. In addition, $k_x = k\sin\theta\cos\varphi$, $k_y = k\sin\theta\sin\varphi$, $k_z = k\cos\theta$, $k_{sx} = k\sin\theta_S\cos\varphi_S$, $k_{sy} = k\sin\theta_S\sin\varphi_S$, $k_{sz} = k\cos\theta_S$, where $k$ is the wave number, $\theta_s$ and $\varphi_s$ are zenith and azimuth angles of the sensor, respectively. $\theta$ and $\varphi$ are zenith and azimuth angles of scattering, respectively. In equation (2-1), $s$ is the RMS height. Subscript *pp* indicates the polarization. To consider a spatial variability, the AIEM includes the term of surface height at different locations (i.e. a phase factor) in Green's function and its gradient for multiple-scattering, implying that the upward and downward re-radiations are accounted for Chen et al. (2003). In contrast, a traditional IEM makes several assumptions that the dependency of Kirchhoff coefficients on a slop term is negligible and the local angle can be replaced by some other angles such as incidence angle, ignoring the spatial variability (Fung, 1994).

To characterize the surface roughness of the grassland on site, an exponential ACF was selected in the AIEM model (Rahman et al., 2007). After simulating the backscattering in the forward mode, soil roughness was inverted by matching the AIEM-simulated backscattering coefficients with the ASAR data measured at three different incidence angles (van der Velde, 2010, van der Velde et al., 2012). Due to a scale dependency of roughness, this inverse method was used, instead of using field-measured roughness (Ulaby et al., 1982, Verhoest et al., 2008). When using ASAR data acquired at three different incidence angles on adjacent days, the time-invariance of roughness was assumed for these days (Mattia et al., 2006, Su et al., 1997, Verhoest et al., 2008).

To perform the roughness experiments, several roughness ranges were generated in LUT based upon different *a priori* assumptions. As shown in the "cl scheme" column of Table 1, four different ranges of *a priori* correlation length information with different minimum and maximum values, as indicated in square brackets, respectively were generated in LUT with the same increment of 0.2. Four cl schemes used the same s scheme #2. Similarly, four different ranges of *a priori* RMS height information with different minimum and maximum

values, as indicated in square brackets, respectively were generated in LUT with the same increment of 0.02. Four s schemes used the same cl scheme #4. Here, a smaller increment was used for the s scheme, because of the high sensitivity of SAR data to the RMS height (Sano et al., 1999). For example, in Table 1, the cl scheme #1 generated the LUT ranging from 0.05 to 5.05 with an increment of 0.2. Similarly, the s scheme #1 established the LUT ranging from 0.05 to 0.95 with an increment of 0.02. Lastly, soil moisture was converted from the dielectric constant inversely determined in a similar manner to roughness. The accuracy of this algorithm was previously reported as 0. 037 $m^3/m^3$, approximately (van der Velde et al., 2012).

Table 1. Various *a priori* roughness information ranges used in LUT

| No. | cl scheme | s scheme |
|---|---|---|
| 1 | [0.05,5.05] | [0.05,0.95] |
| 2 | [0.1,5.1] | [0.1,1.0] |
| 3 | [0.3,5.3] | [0.3,1.2] |
| 4 | [0.4, 5.4] | [0.4,1.3] |

*Four different cl schemes used the same s scheme #2, while four different s schemes used the same cl scheme #4.

2.2.3. Discussions & Results

2.2.3.1.Error propagations of roughness to the soil moisture retrievals

To quantitatively assess the error propagations of *a priori* roughness information, it was investigated how backscattering was converted to soil moisture. Figure 5 corresponds the ASAR-measured backscattering used in a retrieval algorithm to surface soil moisture retrieved by various roughness conditions. Except roughness conditions (i.e. RMS height and correlation length), all other experimental conditions such as ACF, soil dielectric constant, polarization, incidence angle or frequency were same. Because soil moisture was spatially unevenly distributed in a study domain, the subset area showing relatively higher backscattering was selected (if backscattering is too small, its error propagation is too small to be effectively shown here). In addition, DoY 221 was selected in Figure 5, because it was on the driest condition. It was anticipated that a backscattering coefficient would be mainly affected by roughness rather than soil dielectric constant.

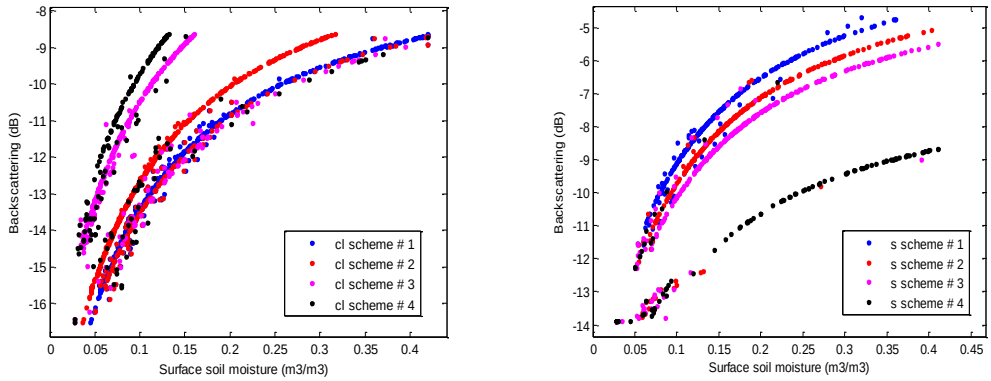


(a) (b)

Figure 5. A change in relationships between ASAR backscattering and soil moisture retrieved with (a) various cl schemes; (b) various s schemes. Wet subset area.

In general, both roughness schemes of RMS height and correlation length showed the similar exponential relationship between backscattering and soil moisture. However, the detailed relationship such as a slope or a dispersion of data points was different in each roughness scheme (Satalino et al., 2002, Sano et al., 1999). In Figure 5, soil moisture decreased as correlation length increased, while it increased as RMS height increased. The propagations of the cl schemes to soil moisture were larger due to their larger increment of 0.2 than the s scheme of 0.02 (Table 1). However, despite of a smaller increment in the s schemes, their propagations to soil moisture became considerably large at s scheme #4 (i.e. the highest minimum of several s schemes: 0.4). Consequently, their overall propagations of a change from the s scheme #1 to #4 was just comparable to that from the cl scheme #4 to #1. For example, at the same backscattering of -11 dB, an increase in RMS height from the the s scheme #1 to #4 increased soil moisture by 0.1120 $m^3/m^3$ at most, while an increment in correlation length from the cl scheme #1 to #4 decreased soil moisture by 0.1256 $m^3/m^3$ at most. This suggested the large error propagation of the RMS height when going beyond the optimal range. This finding is supported by previous studies suggesting that a higher accuracy is required for the RMS height than the correlation length (Lievens et al., 2009, Rahman et al., 2007). In addition, van der Velde *et al*. (2012) previously estimated the similar roughness over the same study site at the RMS height of 0.38 and the correlation length of 1.7. This justified that the s scheme #4 ranging from 0.4 to 5.4 largely propagated soil moisture in Figure 5-b, because a range of roughness exceeded the optimal value of RMS height.

Table 2. The spatial averages of different schemes. Unit: $m^3/m^3$

| Scheme No. | 1 | 2 | 3 | 4 |
|---|---|---|---|---|
| | Roughness [cm] | | | |
| cl scheme | 1.069 | 1.088 | 1.102 | 1.366 |
| s scheme | 0.218 | 0.246 | 0.365 | 0.438 |

| | Soil moisture [$m^3/m^3$] | | | |
|---|---|---|---|---|
| cl scheme | 0.1247 | 0.1230 | 0.1393 | 0.1356 |
| s scheme | 0.1449 | 0.1356 | 0.1080 | 0.1054 |

As discussed above, Table 2 also shows that the propagations of the RMS height to soil moisture were larger, despite of their smaller increment than the cl schemes. However, the trend that soil moisture increased as the correlation length increased and RMS height decreased is somehow opposite to Figure 5 mainly representative of the wet subset only. It is because a spatial average in Table 2 estimated the entire study area including both wet and dry subset area. Here, wet area is defined as the area at a latitude of 31.375 to 31.385, while dry area is defined as the remaining area other than the wet subset area. As shown in Figure 6-b, s scheme #4 overestimated soil moisture in the wet subset with the smaller area, being consistent with Figure 5-b. However, it mostly estimated the lowest soil moisture in the dry subset with the larger area. This led to the lowest spatial average as shown in Table 2.

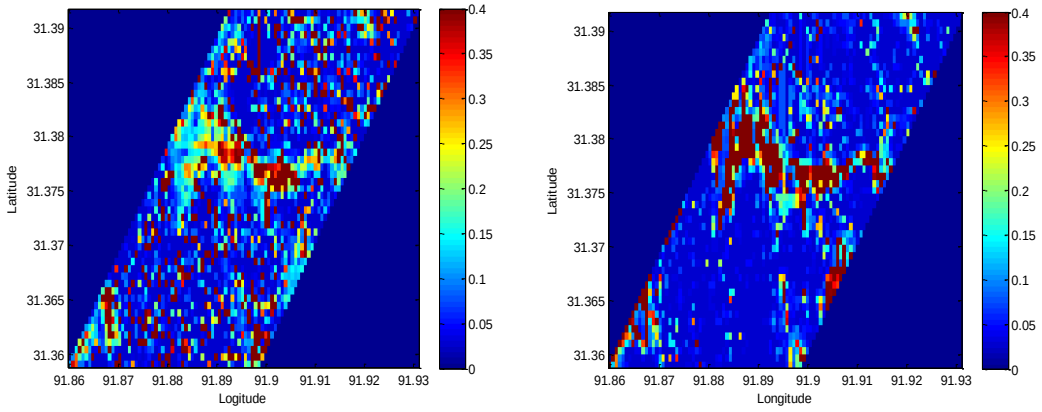


(a) (b)

Figure 6. Soil moisture estimated by the roughness scheme of:
(a) cl scheme # 4; (b) s scheme #4. DoY 221. Unit: $m^3/m^3$

As briefly mentioned above, a spatial distribution of soil moisture was very different in each roughness scheme. For example, each roughness scheme estimated different spatial patterns for run-off (i.e. soil moisture higher than or comparable to the saturated level of 0.42). As indicated by red color in Figure 6, the cl scheme # 4 reported several run-off data in the dry area rather than the wet area, while the run-off spike points suggested by the s scheme #4 were limited to the wet area only. Considering that there have been no rainfall events for several days before and after DoY 221, that the field measurements recorded the driest condition on this day during the season, and that the only difference between Figure 6-a and Figure 6-b was the roughness scheme, it is evident that several run-off data reported in different locations of each figure were mainly caused by roughness inversion errors. It was

also noted that optimal roughness is highly dependent on soil moisture. In specific, different optimal roughness scheme was suggested for each area. The cl scheme # 4 might be more optimal to the wet area, while s scheme #4 represented the dry area better. In other words, the roughness is in inverse relationship to soil moisture. This finding is in accord with (Escorihuela et al., 2007).

2.2.3.2.Error propagation of ASAR-measured backscattering to the soil moisture retrievals

To more systematically assess the magnitude of roughness inversion error propagations, the results in 2.2.3.1 were further compared with other sources of retrieval errors. In addition to geophysical parameter errors such as soil roughness, backscattering measurement is also one of the error sources in SAR retrievals. It can be introduced for various reasons such as calibration error, rainfall events or vegetation attenuation. Especially, in arid and semi-arid regions covered with vegetation as in the Tibetan Plateau of this study site, it is possible that the backscattering signal coming from the vegetation can be added to or subtracted from the moisture in the underlying soils, leading to the measurement errors (Bindlisha & Barros, 2000, Scipal, 2002, Taconet et al., 1996). Due to such multiple scatterings from vegetation and soil (jointly and separately), the backscattering is non-linearly related to soil moisture.

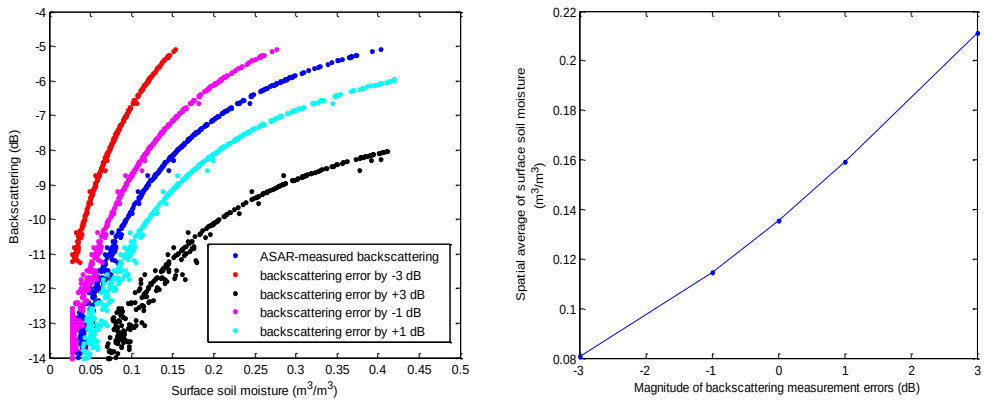


(a) (b)

Figure 7. (a) Relationship between ASAR backscattering in various hypothetical errors and soil moisture retrieved correspondingly; (b) the spatial average of surface soil moisture retrieved with different backscattering error magnitudes used in (a). DoY 221.

In this study, the magnitude of such backscattering errors hypothetically ranged from ±1 dB to ±3 dB (Mattia et al., 2006, Satalino et al., 2002). The same DoY 221 was selected to

compare the backscattering error propagations with the roughness ones measured in Section 2.2.3.1. According to variations in backscattering measurement used for minimizing its mismatch with simulated backscattering, the retrieved surface soil moisture was widely spread, because the relationships between backscattering and soil moisture changed although the same roughness condition of the s scheme #2 was used in SAR retrievals. The error propagation to surface soil moisture was different, depending on whether ASAR backscattering was overestimated or underestimated. As shown in cyan and black-colored dots of Figure 7-a, when the ASAR-measured backscattering was overestimated by +1dB and by +3dB (e.g. due to calibration error or rainfall error by standing water), the retrieved surface soil moisture was largely different because the inverted roughness changed and accordingly the relationship between backscattering and retrieved soil moisture altered. For example, the same ASAR backscattering of −11 dB retrieved the soil moisture at 0.072 $m^3/m^3$ with the original ASAR backscattering, at 0.0952 $m^3/m^3$ with the ASAR backscattering added by a hypothetical error of +1dB, and at 0.16 $m^3/m^3$ with the ASAR backscattering added by a hypothetical error of +3dB. In other words, if the backscattering was erroneously overestimated by +3 dB, soil moisture accordingly was overestimated by 0.088 $m^3/m^3$. This error propagation is smaller than the *a priori* roughness error propagation measured at the same ASAR backscattering value of -11dB, as discussed in Section 2.2.3.1. The error propagation of the ASAR backscattering underestimation (e.g. vegetation attenuation) was smaller than this. For example, as shown in pink and red-colored dots of Figure 7-a, if the ASAR backscattering erroneously attenuated by a hypothetical error of 1dB and 3 dB, accordingly the same ASAR backscattering of −11 dB retrieved the soil moisture at 0.056 $m^3/m^3$ and at 0.032 $m^3/m^3$, respectively, in contrast to the soil moisture retrieved with the original ASAR backscattering of 0.072 $m^3/m^3$. In other words, soil moisture was underestimated by 0.04 $m^3/m^3$ if ASAR backscattering was erroneously attenuated by 3dB, suggesting that the error propagation of ASAR backscattering attenuation is smaller than the backscattering overestimation and much smaller than *a priori* roughness errors. In short, the magnitude of error propagation is roughness errors, ASAR backscattering overestimation, and attenuation in descending order (Satalino et al., 2002, van der Velde et al., 2012).

In Figure 7-b, as the ASAR measurement backscattering error was added, its spatial average of soil moisture linearly increased. By the ASAR backscattering measurement errors of ±1 dB, a spatial average of surface soil moisture altered by 0.0224 $m^3/m^3$. Similarly to a point-scale analysis above, the propagation of the overestimated ASAR backscattering to a spatial average of soil moisture was larger than the attenuated errors. Additionally, the results were also compared with roughness. According to the linear relationship between ASAR backscattering and soil moisture shown in Figure 7-b, the error propagation of the RMS height (i.e. a spatial average of soil moisture decreased by 0.0395 $m^3/m^3$ as the roughness

schemes changed from the s scheme #1 to #4, see Table 2) correspond to the ASAR backscattering errors of – 1.79 dB. The error propagation of the correlation length (i.e. a spatial average of soil moisture increased by 0.0146 $m^3/m^3$ as the roughness conditions changed from the cl scheme #1 to #3, see Table 2) corresponds to the ASAR backscattering errors of +0.6618 dB.

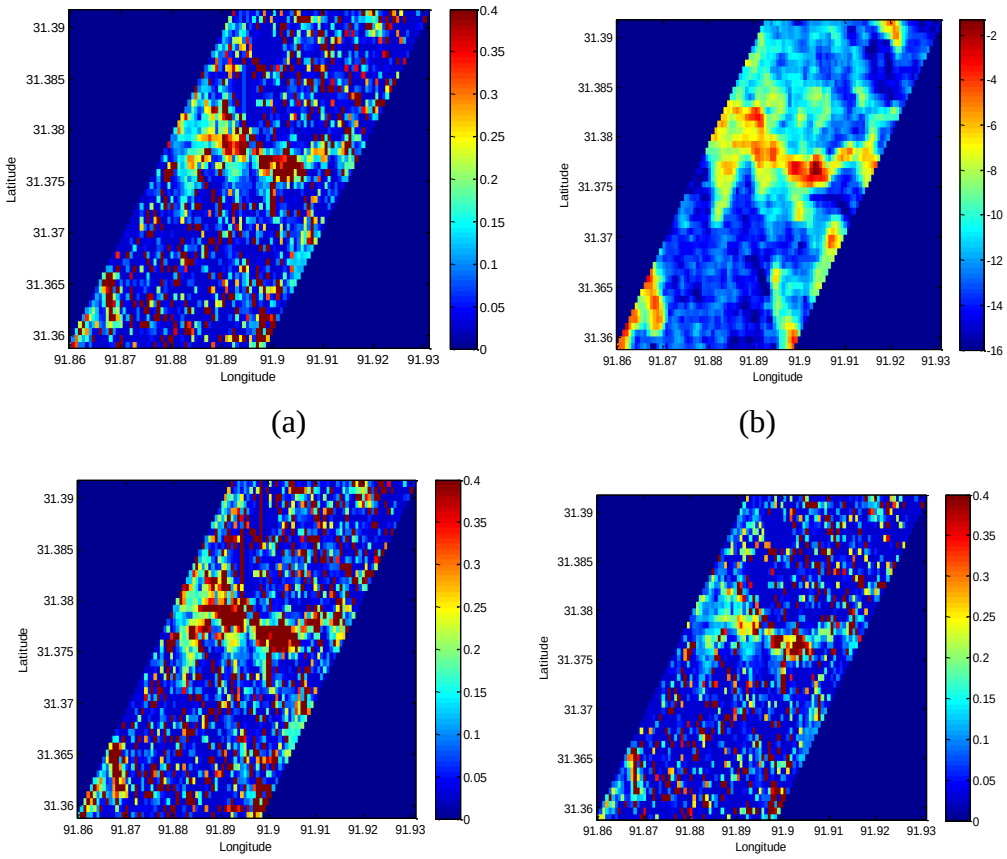


Figure 8. a) soil moisture retrieved from original ASAR backscattering; b) original ASAR backscattering; c) soil moisture retrieved from the hypothetical backscattering error of +1 dB; d) soil moisture retrieved from the hypothetical backscattering error of -1dB. DoY 221. Unit for (a), (c) and (d): $m^3/m^3$, Unit for (b): dB.

A spatial variability in soil moisture was illustrated in Figure 8-c for the ASAR measurement backscattering hypothetically overestimated by 1 dB, and in Figure 8-d for the backscattering error hypothetically underestimated by 1 dB. The spatial average of additive backscattering error scheme was higher at 0.1592 $m^3/m^3$ than that of the original SAR retrieval (Figure 8-a) at 0.1356 $m^3/m^3$, while the spatial average of subtractive backscattering error scheme was lower at 0.1144 $m^3/m^3$ than the original scheme. However, run-off errors in the dry area were

noted, as indicated by several red spike points in both Figure 8-c and d, regardless of the ASAR backscattering error schemes. In addition to this, considering that both the original ASAR backscattering measurement (before applying any roughness scheme, Figure8-b) and a certain roughness condition of s scheme #4 (Figure 6-b) did not show such spike data in dry area in contrast with other roughness conditions, it was concluded that *a priori* roughness scheme is responsible for such run-off errors in dry area rather than the ASAR backscattering errors.

2.2.3.3. Data assimilation analysis

Data assimilation was carried out through two different EnKF schemes: EnOI and EnKF. Their results were compared with the original SAR data at a local point scale and a SAR spatial scale. As described in methods, the difference in the EnOI and EnKF schemes is whether the ensemble used in the EnKF scheme is sequential or stationary. Table 3 shows a time-series point-scale comparison for the SAR data before and after data assimilation. In Table 3, SAR, EnOI and EnKF results are the spatial analysis estimating a single SAR pixel nearest to a local station, and compared with the field measurements. With respect to the field measurements, the original SAR-retrieved soil moisture was significantly overestimated. Their time-average Root-Mean-Square-Error (RMSE) of SAR data for the field measurements was highest at 0.0946 $m^3/m^3$ before data assimilation. However, the RMSE significantly decreased after the data assimilation. The RMSE of the EnKF scheme was lowest at 0.0267 $m^3/m^3$, and the RMSE of the EnOI scheme was slightly higher than, but just comparable to the EnKF at 0.0305 $m^3/m^3$, suggesting that the performance of the EnKF scheme is the best but just comparable to the EnOI scheme at a local point scale.

Table 3. Point-scale comparison with the field measurements. Unit: $m^3/m^3$

| **DoY** | **216** | **219** | **221** | **222** | **224** |
|---|---|---|---|---|---|
| **Field measurement** | 0.0963 | 0.0495 | 0.0213 | 0.0299 | 0.1162 |
| **SAR** | 0.1808 | 0.0512 | 0.1328 | 0.0504 | 0.2736 |
| **EnOI** | 0.0625 | 0.0211 | 0.0692 | 0.0157 | 0.1309 |
| **EnKF** | 0.0636 | 0.0302 | 0.0659 | 0.0378 | 0.1239 |

Especially, on DoY 221, the SAR retrievals significantly overestimated the surface soil moisture in contrast with the field measurements on the driest condition during the season. This is presumably due to the lowest incidence angle, the only peculiarity on DoY 221 in comparison with other data. It was previously found that the incidence angle at VV polarization often influences the estimation of backscattering (Nair, 2007). On DoY 224,

SAR data largely overestimated the soil moisture, being affected by rain events, and accordingly a change in roughness. Data assimilation significantly mitigated such overestimation errors, as shown in Figure 9.

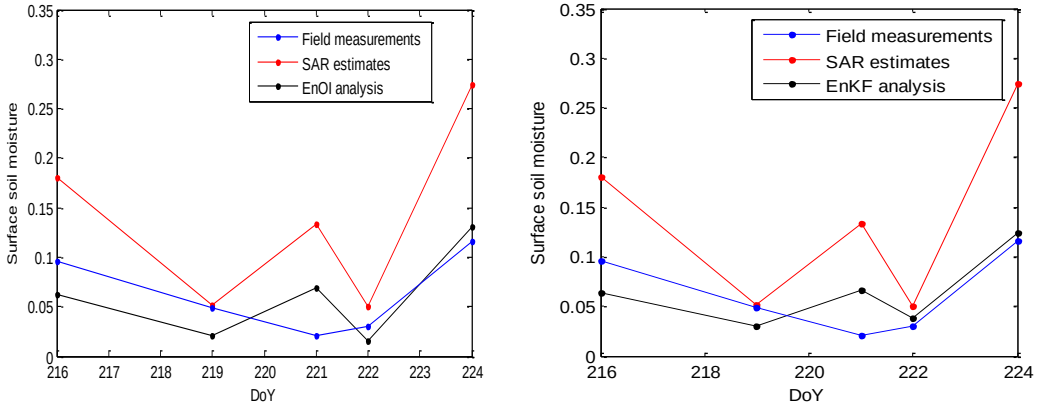


(a) (b)

Figure 9. Time-series 1-D soil moisture (a) by EnOI and (b) by EnKF. Unit: $m^3/m^3$

The performance of data assimilation was further assessed at a spatial scale. DoY 224 was selected for a spatial analysis to assess whether the sequential EnKF scheme will better mitigate the SAR retrieval error by the rain event that occurred on DoY 224 than the stationary EnOI scheme. To effectively demonstrate the systematic errors in SAR retrievals, in comparison, the SVAT model estimation (considered as open-loop) was first illustrated in Figure 10 in conjunction with the original SAR data estimated before the implementation of data assimilation. Although the SVAT model also contains several errors of their own, their estimation provides an informative comparison because their error structure is fundamentally different from the SAR retrievals. As shown in Figure 10-a, the study area was estimated to be dry mostly below 0.2 $m^3/m^3$ by the SVAT model, which is independent from uncertainty of *a priori* roughness information, penetration depth issue, rainfall error or vegetation attenuation problem usually suggested in the SAR retrievals. Instead, for SVAT model, there is uncertainty in input parameters such as a spatial variability of rainfall data, subsurface soil and hydraulic property, and the applicability of assumption used for land surface parameterization (Montaldo & Albertson, 2001, Montaldo et al., 2001, Pellarin et al., 2009).

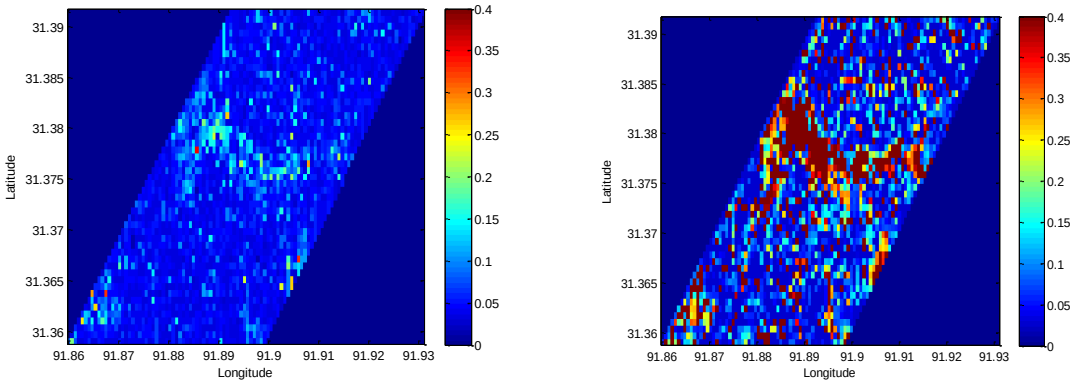


(a) (b)

Figure 10. Soil moisture estimated by a) SVAT and b) SAR. DoY 224. Unit: $m^3/m^3$

As shown in Figure 10-b, the SAR-retrieved surface soil moisture was estimated to be much higher than the SVAT model. More specifically, the spatial average of SAR surface soil moisture was higher at 0.1140 $m^3/m^3$ than the SVAT model at 0.0565 $m^3/m^3$. The SAR data also reported that the surface run-off occurred in dry area. Despite of uncertainty in SVAT model as described above, because there has been no rainfall for several days until DoY 224 and because the field measurements also reported just moderate condition around 0.1 $m^3/m^3$, the run-off in dry area and generally wet condition estimated by the SAR retrievals were considered overestimation. The overestimation of SAR data is considered due to rainfall and consequently roughness. As discussed in Section 2.2.3.1., the roughness condition of the s scheme #2 used in original SAR retrievals tends to generally overestimate surface soil moisture and specifically misestimate run-off in comparison with the s scheme #4 (Figure 6-b). Additionally, the assumption used in original SAR retrievals that roughness does not change over the SAR data measured from three different incidence angles on near days cannot be applicable, because there was rain (0.4 mm/day) on DoY 224. In rain, the surface becomes thinner due to decrease in a penetration depth or sometimes in a film of the standing water formed by rain that fell on terrain slope or vegetation, leading to a change in roughness. Additionally, a penetration depth or optical depth may change due to rain, resulting in SAR retrieval errors (Saleh et al., 2006).

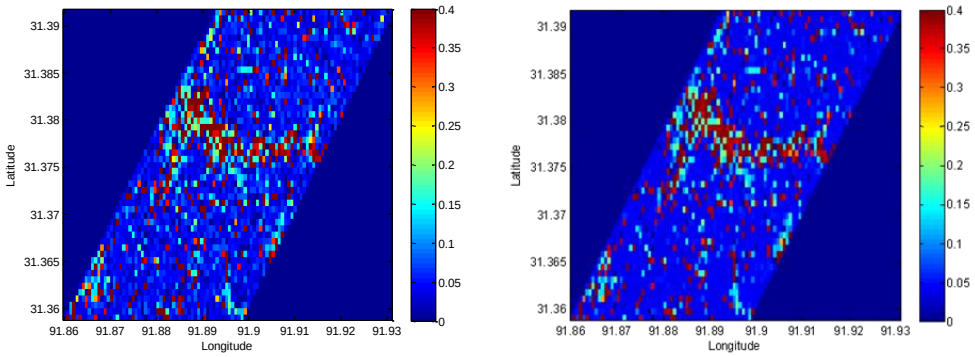


(a) (b)

Figure 11. Soil moisture estimated by (a) EnOI and (b) EnKF. DoY 224. Unit: $m^3/m^3$

Data assimilation analysis successfully provided the intermediate values between two extreme estimations by SAR and SVAT model. As shown in Figure 11, the overestimation by SAR retrievals and the underestimation by the SVAT model were appropriately adjusted after data assimilation. More specifically, the spatial average of the EnOI scheme was lower at 0.1048 $m^3/m^3$ than the SAR retrievals. However, it was still higher than that of the EnKF scheme at 0.0717 $m^3/m^3$. The spatial average of the EnKF scheme was higher than the SVAT model. A reduction in the spatial averages of both EnKF and EnOI schemes indicates that the run-off errors were successfully mitigated by data assimilation. Those run-off errors are considered due to roughness errors for several reasons. First, the roughness errors were a more influential factor than vegetation attenuation, as quantitatively analyzed in Section 2.2.3.1. and 2.2.3.2. Secondly, the time-invariant assumption used for inverting the roughness is not applicable to rainy day on DoY 224. Decisively, by comparing Figure 6-a and b, it was demonstrated that such spike data in dry area were removed by changing roughness conditions. In contrast, such spike data in dry area could not be effectively removed by adjusting the ASAR backscattering errors (see Figure 8-d). In addition, the original ASAR backscattering did not contain such spike signals (see Figure 8-b). Thus, it was concluded that run-off errors in dry area was largely influenced by roughness errors. This finding is consistent with (van der Velde et al., 2012). Those roughness errors were significantly reduced by the EnOI scheme, as shown in Figure 11-a. They were far more mitigated by the EnKF scheme, demonstrating a lower spatial average than the EnOI scheme. However, some of the run-off errors still remained even in the EnKF scheme. If excluding such errors, the EnKF final analysis was comparable to the SVAT model estimation in terms of a spatial average and soil moisture distribution. Hence, based upon the EnKF results in a point-scale comparison (Table 3) and a reduction in the spatial average as well as run-off error at a SAR spatial scale (Figure 8), it was suggested that the performance of the EnKF scheme is better than the EnOI scheme. This result is consistent with other previous studies. Evensen (2003)

introduced the EnOI scheme as a cost-effective alternative for EnKF, and discussed that it is usually a suboptimal solution when compared to the EnKF. Oke et al. (2007) also stated that the EnKF scheme outperforms the EnOI without localization because the ensemble spread in EnKF gradually decreased over time, resulting in a more accurate estimation of forecast error covariance.

Therefore, combining the discussions in Section 2.2.3.1 to Section 2.2.3.3, it was concluded that the data assimilation mitigated several SAR retrieval errors, alleviating the overestimation by SAR and the underestimation by SVAT model. Roughness errors were effectively reduced by the EnKF scheme. However, some run-off errors still remained in the EnKF results, since the erroneous SAR data was used as the observations in the data assimilation scheme.

#### 2.2.3.4. Conclusion & Summary

This study attempted to reduce the SAR retrieval errors arising from inappropriate *a priori* roughness information with data assimilation. First, the roughness error in SAR retrieval algorithm was characterized as follows. Error propagation of the RMS height was larger than that of the correlation length despite of a smaller increment, implying that a higher accuracy is required for RMS height. By changing the roughness scheme, run-off errors in dry area could be removed. In contrast, such run-off errors could not be effectively adjusted by changing backscattering error schemes. In addition, according to the error propagation analysis measured at a backscattering of -11 dB, the roughness errors were more largely disseminated to soil moisture estimation than backscattering error schemes. In wetter soils (e.g. higher than -11 dB), the error propagation may be larger than this. Therefore, it was suggested that run-off errors in dry area was mainly due to roughness errors.

To appropriately alleviate such roughness errors, two data assimilation schemes were implemented by assimilating SAR surface soil moisture into a SVAT land surface model. One scheme was a sequential EnKF, while the other scheme was a stationary EnOI. At a local point scale, the data assimilation results showed that the RMSE of SAR data for the field measurements significantly decreased after data assimilation. The lowest RMSE was found in the EnKF scheme. However, it was comparable to EnOI. At a SAR spatial scale, the data assimilation successfully reconciled the overestimation of SAR data and the underestimation of SVAT model. A spatial average of the EnOI scheme was lower than SAR data, while that of the EnKF scheme was lower than EnOI but higher than SVAT model. One of the reasons for this lower estimation in EnKF was considered because the run-off errors in the dry area arising from *a priori* roughness information errors were successfully reduced by EnKF. Therefore, it was suggested that EnKF outperformed EnOI because the former could more

accurately estimate the forecast error covariance through ensemble spread evolving over time.

### 2.3. Optimization of stationary EnKF

This Section suggested the method optimizing the stationary EnKF described in Section 2.2.2.2, because the stationary ensemble-based EnOI is usually sub-optimal, despite of a high computational efficiency. The optimization was conducted by empirically manipulating the observation errors. This is important, because the error of true field can be transferred to EnKF analysis as the EnKF converges towards true field, usually the satellite data on a large-scale. After a thorough review, Reichle (2008) pointed out that *a priori* quality control information referring to the Radio-Frequency Interference (RFI) included in satellite data sets is rarely sufficient for the success of soil moisture data assimilation. Since both satellite data and *in-situ* field measurement contain a certain degree of unknown measurement errors or biases, a reduction in Root Mean Square Error (RMSE), a successful convergence to the observations or the excellent performance of data assimilation *per se* does not necessarily signify that the data assimilation final analysis provides the immaculate truth. Accordingly, it was argued that the observation error or bias correction is required, prior to data assimilation. The same problem can be raised for SMOS data assimilation over the semi-arid region in West Africa, where soil moisture is often less than 0.05 $m^3/m^3$. It was previously known that passive microwave sensors such as AMSR-E are prone to mis-estimate soil moisture in dry and sandy soils as in Mali site (Gruhier et al., 2008). The brightness temperature errors in microwave radiometry at L-band as in SMOS instrument occur mostly in dry soils (Escorihuela et al., 2010). Such satellite data error may be transferred to the analysis, while EnKF converges to the observations. Hence, we suggest the EnKF scheme accounting for those satellite data errors and biases in West Africa.

Objective of this Section is 1) to demonstrate the systematic error propagations of SMOS retrieval algorithms over West Africa in dry and sandy soils, and 2) to provide the computationally effective EnKF scheme empirically pre-processing the SMOS data errors and biases, by means of the L-MEB radiative transfer forward model. In comparison with other previous studies, this approach suggests several operational merits. Firstly, this does not require a long record of satellite data like Cumulative Distribution Functions (CDF) matching technique (at least one year) and the sequential EnKF assuming a global constant *a priori* variance for observation errors (Reichle et al., 2007; Reichle & Koster, 2004). This aspect is advantageous, because in several cases such as weather prediction or climate models, soil moisture data is required for initial conditions only. Secondly, this does not require assuming a slow evolution or a global constant for the observation bias or error parameters in the observation operator of EnKF (Fertig et al., 2009). This aspect is advantageous, because the

satellite retrieval errors, in fact, evolve rapidly with time (e.g., sudden rainfall events can result in a large change in retrieval errors, Saleh et al., (2006)) and heterogeneously over a wide variety of landscapes and climatic conditions (Margulis et al., 2002). Finally, it is more simply than a localization approach, which can degrade the data assimilation analysis if the length-scales of the localizing function are inappropriate (Oke et al., 2007).

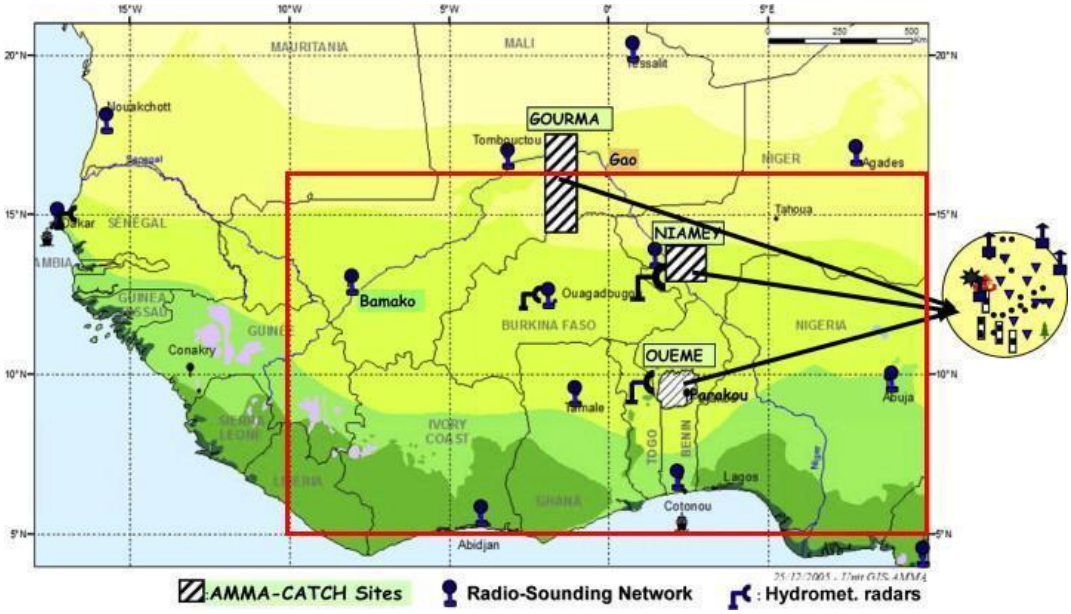


Figure 12. The study domain denoted by red line (Lebel et al., 2009).

### 2.3.1. *Experiment sites and data*

Figure 12 illustrates a study domain around the sub-Saharan area (5-16°N and 10°W-10°E). Because most Western African populations are concentrated in this sub-Saharan area rather than the infertile Saharan desert, this specific region is of high interest, and considered vulnerable to climate change (ECOWAS-SWAC/OECD, 2007, FAO-SWAC, 2007, World Food Program, 2010). The time-invariant ECOCLIMAP datasets revealed that this study area is a highly sandy region. A clay fraction is estimated at 15.8%, and a sand fraction at 52.6% (30% to 95%), on a spatial average. The ECMWF datasets reported this region in hot weather. The spatially averaged air and land surface temperature was 30 ℃ with a maximum of 41 ℃, and a minimum of 17 ℃, approximately, during the experiment period.

For the validations, AMMA field campaign data were used as in-situ field measurement. During the AMMA campaign, several soil moisture sensors were installed in West Africa. Most of those sensors were distributed over three AMMA supersites located in Niger

(Wankama region, 50 km East of Niamey), Mali (Agoufou region) and Benin (Djougou region), as shown in Figure 2, and 3. Long-term soil moisture observation experiments have been conducted since 2006 onwards in those sites, except Mali, due to the putsch in early 2012. There were six and eight sensors within a 0.25° x 0.25° grid cell at established at the Niger and Benin site, respectively. The measurements obtained from several probes in each site were spatially averaged in order to be as representative as possible of a single pixel of satellite image. All the soil moisture probes were deployed at a depth of 0.05 m for the top layer and 1 m for the root zone layer. The detailed descriptions of rain gauge networks and soil moisture measurements were provided by Cappelaere et al. (2009) for the Niger site, and by Séguis et al. (2011) for the Benin site.

For the observations, one day ascending SMOS data was used in a point scale experiment, while three day ascending SMOS data for a wider spatial coverage was exploited in a large scale experiment. Level 3 surface soil moisture SMOS data (CATDS OP 245) were directly obtained from CATDS (http://www.catds.fr/). SMOS L3 data is a global composite of L2 data, a swath product (Jacquette et al., 2010, Kerr et al., 2012, 2013). The SMOS L2 data retrieved by a L2PP processor (ver. 5.51) used a Mironov formulation for the calculation of dielectric constant in dry and sandy soils, while SMOS L3 products used a Dobson model.

For the forecasts, the SVAT land surface model was used (see Section 4.2. for a detailed description). The input data were obtained from following sources: the ECMWF datasets (resolution: 0.25 day, 0.5 degree, AMMA dataset operational archive) for meteorological inputs such as air, soil and land surface temperature, inward and outward long and shortwave radiations, and relative humidity; Tropical Rainfall Measuring Mission (TRMM) 3B42 data (resolution: 0.125 day, 0.25 degree) for rainfall; the ECOCLIMAP datasets for Leaf Area Index (LAI), thermal and aerodynamic roughness height (resolution: 10 days, 0.25 degree), and time-invariant soil fractions (i.e. clay and sand from Food and Agriculture Organization (FAO) map at 10 km resolution) (Champeaux et al., 2005, Lee et al., 2012a). The spatial resolution of SVAT model inputs were all re-scaled to the SMOS data dimension at 0.25 degree, by reading the nearest pixel value. The temporal resolution of SVAT model simulation was 0.25 day. However, only when the SVAT time step of the day is comparable to the 1 day SMOS data acquisition time, the model estimates were selected and used for the data assimilation on a daily basis.

2.3.2. EnKF scheme

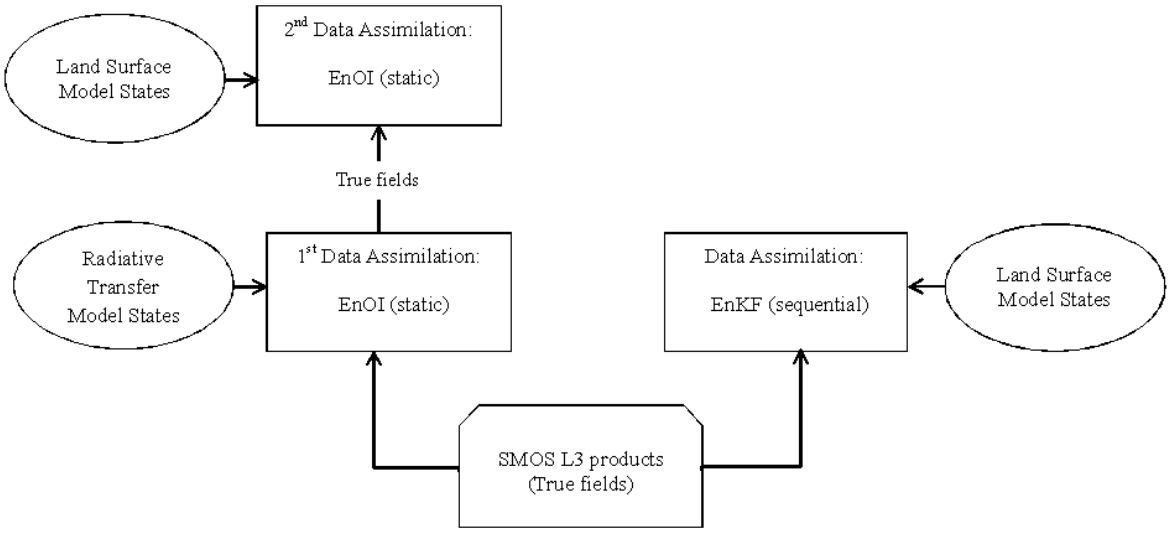


Figure 13. The schematic diagram of stationary (left) and sequential EnKFs (right).

Two different EnKF schemes are illustrated in Figure 13. The main difference between two methods is that the stationary EnKF using one-time update is optimized by empirically defining the satellite observation errors, while the sequential EnKF uses a time-invariant global constant a priori variance for defining the observation errors. The two-step stationary data assimilation is shown in the left hand part of Figure 13. In the 1st step, the SMOS L3 soil moisture is assimilated into a L-MEB radiative transfer model, which are differently perturbed by three different error sources (i.e. geophysical parameters, brightness temperature, land use fractions) in Table 4 (Kerr et al., 2012; 2013). Due to the difference between the SMOS L2 products of a L2PP processor and L3 data, this step takes account of forecast errors in dielectric constant in sandy and dry soils. In the 2nd step, a product of the 1st data assimilation (brightness temperature scheme) is further assimilated into SVAT land surface model via EnOI. On the other hand, the sequential EnKF is shown in the right hand part of Figure 13. This scheme sequentially assimilates the same SMOS L3 surface soil moisture products into the SVAT land surface model for a longer period of time step.

2.3.2.1. Sequential EnKF

A detailed theoretical description of sequential EnKF is introduced above in Section 2.2.2.1.

*Ensemble generation and experimental set-up*

In a sequential EnKF, 1 day SMOS L3 surface soil moisture products were assimilated into the SVAT model at the same time step with the SMOS data acquisition time. The time-invariant global constant observation variance of 0.01 $[m^3/m^3]^2$ was used for the perturbation of true field, the SMOS L3 data. Here, true field implies the observations not taking account of observation errors (Evensen, 2003). The observation variance was aprioristically determined based upon the RMSE from the field measurements. A spatial dimension and the time step of available observation were same with those of model state. For the generation of SVAT surface soil moisture ensemble members, two dimensionless soil hydraulic variable $C_1$ and $\theta_{geq}$ in SVAT model formulations (see Section 4.2.) were randomly generated, ranging from 0.01 to 1 and from 0.01 to 0.5, respectively. Due to the uncertainty of these two input variables, they were not restricted to be Gaussian distributed (Braud et al., 1993; Evensen, 2003). TRMM-retrieved rainfall data was also perturbed, assuming a Gaussian distribution and a variance of 10%, according to the error analysis specific to TRMM data (Yuter et al., 2005). In a local point scale experiment, the initial conditions of SVAT model were adopted from the in-situ field measurements. Similarly, in a large scale experiment, the initial conditions were obtained from SMOS L3 products. The SVAT model was run for 40 days before capturing the ensemble pool. Ensemble size was 100. Inflation, localization and spatial correlation were not used for the implementation of EnKF, but completely local at a pixel scale. A sequential EnKF was carried out continuously from DoY 176 to 188.

2.3.2.2. Stationary EnKF

A theoretical description of EnOI is introduced above in Section 2.2.2.2. Here, L-MEB forward model used as the observations is briefly introduced, and experimental set-up is followed.

*L-MEB forward model*

The SMOS retrieval algorithm employs a cost function approach minimizing a difference between brightness temperatures (Level 1C products) measured by SMOS instrument and simulated by the L-Band Microwave Emission of Biosphere (L-MEB) forward model in order to determine geophysical parameters as well as soil moisture (Kerr et al., 2012, 2013, Wigneron et al., 2007). In each iteration, it updates a new value of several parameters in a dominant area, whereas the pre-determined reference values are assigned for the default conditions (remaining area other than a nominal mode). In this step, it selects an appropriate model in a model library that represents the dominant landscape in a given domain, according to a decision tree (refer to Figure 1 in Kerr et al (2012)). This decision tree is based upon the

aggregated fractions (i.e. land use assessed by the ECOCLIMAP datasets), as suggested by scheme 3 in Table 4.

In a nominal surface, different brightness temperature (TB) models are used, according to land surface conditions (Kerr et al., 2013). For smooth bare soil,

$$TB_p = (1 - r_{bp})T_g \qquad (3\text{-}1)$$

where, $r_{bp}$ soil reflectivity is a function of dielectric constant and incidence angle. $T_g$ is effective soil temperature. The dielectric constant required to determine $r_{bp}$ is defined by a Dobson semi-empirical model as a function of soil moisture, soil bulk density, and soil particle density or a Mironov semi-physical model as a function of soil moisture and wilting point. Mironov formulation is preferred for dry and sandy soil conditions. For low vegetation, a following $\tau - \omega$ model is used. It consists of the direct vegetation emission, the vegetation emission reflected by soil and attenuated by canopy, and the soil emission attenuated by a canopy.

$$TB_p = (1-\omega_p)(1-\gamma_p)(1+ \gamma_p\, r_{gp})T_c + (1-r_{gp})\, \gamma_p\, T_g \qquad (3\text{-}2)$$

where, $\omega_p$ is single scattering albedo, and $T_c$ is canopy temperature. The vegetation attenuation factor $\gamma_p$ (or vegetation transmissivity) is determined with the optical depth $\tau_p$, as follows:

$$\gamma_p = \exp(-\tau_p / \cos\theta) \quad \text{where, } \tau_p = \tau_{sp} + \tau_L + \tau_{IP} \qquad (3\text{-}3)$$

The optical depth by standing vegetation $\tau_{sp}$ is further expressed as $\tau_{S\_NAD}$ $(\sin^2(\theta).tt_p + \cos^2(\theta))$, where the vegetation optical depth at nadir $\tau_{S\_NAD}$ is a function of LAI. In the same formulation, $tt_p$ is angular correction factor, $\theta$ is incidence angle. Returning back to equation 3-3, the optical depth by litter $\tau_L$ is estimated with several coefficients including the litter attenuation coefficient $c_L$ and the litter water content LWC as well as soil moisture. The next element in 3-3, $\tau_{IP}$ takes into account an increase of optical depth by the intercepted water of a standing vegetation. Returning back to the equation 3-2, $r_{gp}$ soil reflectivity is defined, as follows:

$$r_{gp} = ((1 - QR)r_{bp} + QR\, r_{bp}) \exp(-HR \cos^{NR_p}(\theta)) \qquad (3\text{-}4)$$

where, the polarization coupling factor QR is set to zero at L-band. $r_{bp}$ is smooth surface reflectivity for alternate polarizations, while $NR_P$ is an integer to describe the influence of

incidence angle θ on the surface roughness. Effective surface roughness HR is a function of soil moisture (Escorihuela et al., 2007). Additionally, the effective soil temperature $T_g$ in equation (3-2) is determined with $T_{soil\_depth}$ deep soil temperature (0.5 to 1 meter) and $T_{soil\_surf}$ surface soil temperature (1 to 5 cm).

$$T_g = T_{soil\_depth} + C_t (T_{soil\_surf} - T_{soil\_depth}) \quad (3\text{-}5)$$

where, $C_t$ is formulated by relationship of min[(soil moisture/$w_0$)$^{bw0}$, 1], and coefficients $w_0$ and $b_{w0}$ are a function of soil type. For forest, the algorithm uses the similar formulation described above but different default values.

*Ensemble generation and experimental set-up*

The two-step stationary EnKF is shown in the left hand part of Figure 13. To empirically optimize the L-MEB forward model states (SMOS L2 products) in the 1st step with a L2 processor, three different schemes shown in Table 4 were examined: scheme 1 perturbed the geophysical input parameters of the L-MEB model; scheme 2 disturbed the brightness temperature input; scheme 3 perturbed the landscape fraction to examine the uncertainty associated with a selection of a landscape-based model in the SMOS retrieval algorithm. According to the error budget study preliminarily examined by Kerr et al. (2013), the retrieval errors stemming from instrument error, sky and ionosphere, or atmospheric effect were considered limited. Instead, other error sources such as radiometric error, uncertainty of *a priori* geophysical parameters, soil texture, or soil roughness were suggested to largely influence the final estimation of soil moisture.

Table 4. L-MEB radiative transfer model perturbation schemes for 1st step of stationary EnKF

| No. | True field | L-MEB radiative transfer model states | Objective |
|---|---|---|---|
| 1 | SMOS L3 products | SMOS L2 ensembles perturbed by random geophysical input parameters (LAI, ECMWF soil moisture, soil temperature, clay & sand fraction) | To assess the L-MEB retrieval errors propagated by geophysical parameters |
| 2 | SMOS L3 products | SMOS L2 ensembles perturbed by random brightness temperature inputs (L1C data) | To assess the L-MEB retrieval errors propagated by brightness temperature |
| 3 | SMOS L3 products | SMOS L2 ensembles perturbed by random landscape fractions (FNO, FFO, FWL, FWP, FWS, FEB, FEI, FEU) | To assess the L-MEB retrieval errors propagated by a land use-based model selection |

First, scheme 1 in Table 4 examined the propagation (or sensitivity) of *a priori* geophysical parameters to the estimation of soil moisture. Uncertainty in each geophysical parameter is discussed, as follows:

- Surface roughness: surface roughness has an influence on the determination of soil reflectivity $r_{gp}$ whose errors can be propagated up to the estimation of brightness temperature (see equation 3-2). In the SMOS retrieval algorithm, the surface roughness is formulated as a function of *a priori* soil moisture information. That formula was empirically established, based upon the SMOSREX datasets in loamy soil texture with a clay fraction of 17 % and a sand fraction of 36%. Escorihuela et al. (2007) previously suggested that the formula is uncertain in different soil texture, high soil moisture gradients, or different probe sampling depth. Our experiment site is in such circumstances. The sand fractions in West Africa are much higher than the SMOSREX datasets, often reaching up to 95%. Soil composition is more diverse than that. Additionally, during the WAM, the intense precipitation fallen on dry soils might cause large vertical soil moisture gradient conditions. Escorihuela et al. (2010) also argued that the relationship between roughness and soil moisture depends on soil dielectric constant model, whose performance is highly affected by a sand fraction or soil moisture. Hence, to examine the propagations of surface roughness to soil moisture, *a priori* soil moisture (i.e. volumetric soil water layer 1 of the ECMWF datasets) was perturbed with the assumption of a normal distribution and a variance of 20%. Transition moisture (XMVT) and field capacity (FC) required for estimating the roughness were also propagated from the clay and sand fractions perturbed by assuming a Gaussian distribution and a variance of 50%.

- Optical depth: erroneous optical depth adversely affects the vegetation attenuation factor $\gamma_p$, whose error is eventually propagated up to brightness temperature (see equation 3-2 and 3-3). In the SMOS retrieval algorithm, optical depth is defined with the vegetation optical depth at the nadir $\tau_{S\_NAD}$ as well as several other fitting coefficients (e.g., $b'$, $b''$, $tt_H$, $tt_v$, $c_L$, or litter layer water contents). Uncertainty is mainly introduced from the $\tau_{S\_NAD}$ formulated with LAI (Gruhier et al., 2008, Holmes et al., 2008, Kerr et al., 2013). In the SMOS retrieval algorithm, LAI is employed due to its global availability. However, the optical depth is significantly related to the Vegetation Water Content (VWC), because it presents better vertical characteristics than LAI. The latter is often saturated even in low vegetation (Lee et al., 2012a). Additionally, the fitting coefficients required in vegetation model were known to be dependent on a vegetation type. Most vegetation types in our experiment site are more diverse than that in the SMOSREX field site. Thus, to account for such uncertainties associated with the use of LAI, and heterogeneous vegetation conditions on a large scale, the optical depth was propagated from the perturbation of LAI (8 day MODIS data), which was

assumed to be normally distributed with a variance of 40%.

- Effective soil temperature: erroneous effective soil temperature directly affects the estimation of brightness temperature (see equation 3-2). In the SMOS retrieval algorithm, it is formulated with the parameter $C_t$, which is further calculated with *a priori* surface soil moisture and some other soil texture-sensitive coefficients (see equation 3-5) (Kerr et al., 2013). Firstly, uncertainty is introduced from the parameterization of $C_t$, because it was previously argued that $C_t$ parameterized as a function of dielectric constant showed a better agreement with theoretical values than that of soil moisture (de Rosnay & Wigneron, 2005). In addition, there is uncertainty associated with soil texture-sensitive fitting coefficients such $w_o$ and $b_{wo}$ (see equation 3-5), because the soil texture in our experiments is different from literature (Gruhier et al., 2008). Hence, to assess the sensitivity of surface soil moisture to $C_t$, *a priori* soil moisture was perturbed as stated above in surface roughness Section. To take into account uncertainty in the soil texture-sensitive fitting coefficients, auxiliary soil property data (e.g. clay, sand, $w_o$ and $b_{wo}$) were randomly disturbed. In addition, to assess uncertainty arising from the vertical soil temperature gradients, *a priori* soil temperatures at top and deep layers in the ECMWF datasets were also randomly perturbed by assuming a normal distribution and a specified variance of 30 %.

In scheme 2 of Table 4, the hypothetical error propagations of brightness temperature to the estimation of soil moisture was examined. The ensemble pool of the brightness temperature (L1C data) measured by SMOS instrument was established by assuming a normal distribution and a variance of 40 %. WAM rainfall effects, RFI over West Africa, uncertainty arising from vegetation and dielectric constant model were considered for determining the magnitude of brightness temperature errors (e.g. 25K) (Holmes et al., 2008, Schlenz et al., 2012, Shin, 2011). Finally, scheme 3 was suggested to examine the propagations of the ECOCLIMAP datasets-based land cover misclassification to the estimation of soil moisture (Kerr et al., 2012). In the SMOS retrieval algorithm, a different retrieval model is selected in a decision tree, depending on fraction percentage (i.e. land cover type) so that the errors in fraction information can be propagated to soil moisture estimation. When perturbing the fractions, only fractions with non-zero percentages in a given node were randomly disturbed. Consequently, a summation of all the eight different fractions always remained the same as 100%. By means of this perturbation, a dominant landscape representing a given node and a resultant retrieval model were randomly altered. The ensemble size for three schemes in Table 1 was 50.

Based upon the error propagation analysis of three different schemes stated above, the scheme 2 was selected, and used as model states for the 1$^{st}$ step. In the following step, the

same SVAT model ensembles of a sequential EnKF described in Section 2.2.1 and obtained on DoY 186 to 188 (i.e. requiring three days of SMOS data to fully include the study domain) was one time updated with the products of the 1st step data assimilation. Similarly to the sequential EnKF scheme, inflation, localization and spatial correlation were not used, but completely local at a pixel scale. The same observation variance of 0.01 $[m^3/m^3]^2$ was aprioristically applied for the perturbation of true field in both steps, assuming a time-invariant global constant. A spatial dimension and the time step of available observation were same with those of model state.

2.3.3. Discussions & Results

2.3.3.1. Evaluation of SMOS data at a local point scale

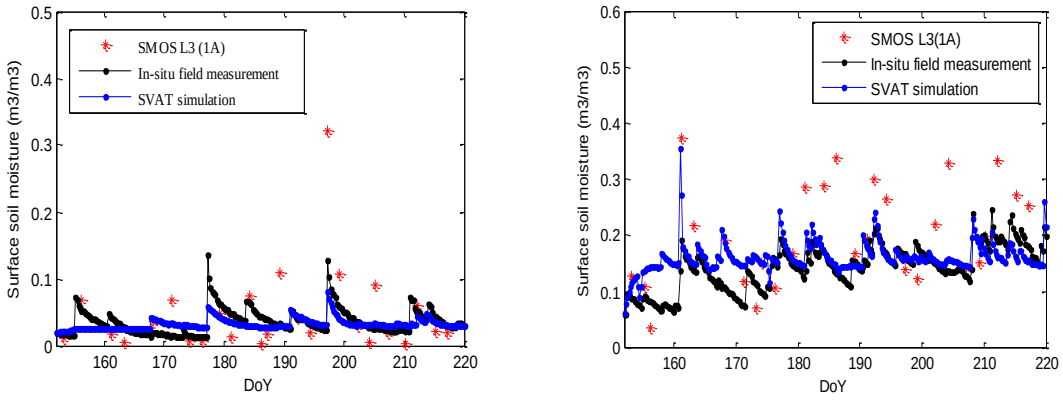


(a) (b)

Figure 14. Time-series comparison between SVAT-simulated surface soil moisture estimates and SMOS L3 data (1 day ascending indicated by 1A): (a) Niger; (b) Benin.

The SVAT model estimates and SMOS L3 data were compared, with respect to the AMMA campaign data measured at a local station and up-scaled to a single pixel of satellite data. In the Niger site (Figure 14-a), time-averaged field measurement of surface soil moisture was 0.0360 m3/m3, while that of root zone soil moisture was 0.0474 m3/m3. According to the field observatory, the accumulated rainfall (spatially averaged) was 358.52 mm during the experiment period. The RMSE of SVAT model estimates was found to be 0.0188 m3/m3, while the RMSE of SMOS L3 products was 0.0555 m3/m3. The SMOS data showed a larger discrepancy for various reasons.

First, several SMOS data points drier than field measurements were considered, primarily due to a Dobson model used for retrieving SMOS L3 data. It was known that soil moisture is underestimated and roughness is overestimated when using a Dobson model especially over dry and sandy soils as in the Niger site (Escorihuela et al., 2010, Kerr et al., 2012, Mironov et al., 2013, Wigneron et al., 2011). This observation bias was expected to be mitigated in the stationary EnKF. In the L2 processor being used for generating the L-MEB forward model ensembles in the 1$^{st}$ step of a stationary EnKF, a Mironov formulation is applied to dry and sandy soils. In addition to a dielectric constant model stated above, an increase in the penetration depth in dry and sandy soils is also considered influential. The penetration depth –at L-band, theoretically just 2 cm in a wet soil top layer (1/10λ: where, λ is wave length) - becomes much deeper in dry and coarse textured soils, as in the Niger site. Accordingly, the SMOS surface soil moisture might have shown a different estimation from the field measurements or SVAT model estimates fixed at a depth of 5 cm. It is also uncertain to use the maximum surface roughness over dry soils in a SMOS retrieval algorithm. Escorihuela et al. (2010) previously suggested that the dependency of roughness on soil moisture is obscure for several reasons. More specifically, the surface roughness overestimated in dry soils, due to the inverse relationships used in a SMOS retrieval algorithm was speculated to overestimate the soil emissivity and brightness temperature, resulting in the underestimation of soil moisture. In contrast to this, the SMOS data sometimes also showed several overestimations in the events of rain. For instance, in Figure 14-a, on DoY 197, the SMOS data showed overestimation as compared to the field measurements in the event of rain (intensity: 25 mm/3hr, according to the spatially averaged local rain gauge network data). This was considered due to the unstable penetration depth and surface roughness in rain. It was thought that the rain fallen on very dry soil surface enhanced a vertical soil moisture gradient. Such a condition further increased the dependency of roughness on a penetration depth, which is usually influenced by rain (Escorihuela et al., 2010, Jackson et al., 2012). For this reason, the SMOS data was thought to show a disagreement with field measurements in the event of rain.

In the Benin site, as shown in Figure 14-b, time-averaged field measurement of surface soil moisture was estimated as 0.16 $m^3/m^3$, while that of root zone soil moisture was higher at 0.288 $m^3/m^3$. According to the field observatory, accumulated rainfall was 1289.09 mm during the experiment period. The RMSE of SVAT model estimates was 0.0389 $m^3/m^3$, while the RMSE of SMOS data was 0.1051 $m^3/m^3$. The larger inconsistency between the SMOS data and the field measurement was considered to be attributed to the rain events. It was previously discussed that the vegetation optical depth misestimated by rain interceptions (with no geometric implication) might lead to the errors in brightness temperature estimation

(Saleh et al., 2006, Schlenz et al., 2012).

2.3.3.2. Evaluation of SMOS products at a spatial scale

For a spatial comparison, the SVAT model estimates were re-arranged, according to 3 day ascending SMOS L3 data acquisition time. Consequently, a data acquisition time difference between the SMOS data and SVAT estimates was only several minutes, approximately. The comparison between the SVAT surface soil moisture estimates and the SMOS L3 data is illustrated in Figure 15.

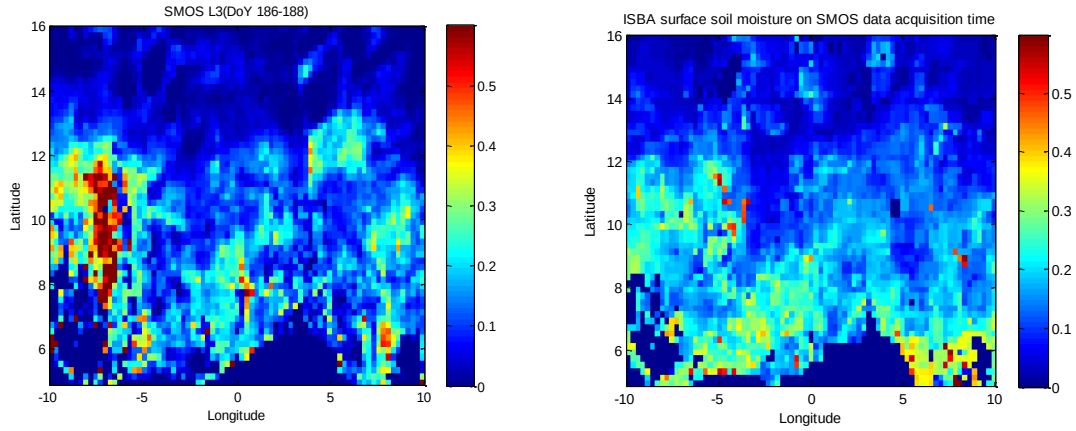


(a) (b)

Figure 15. Surface soil moisture estimates:
(a) SMOS L3 data; (b) SVAT model estimate (open-loop). Unit: m3/m3

The spatial RMSE between them was found to be significant at 0.129 $m^3/m^3$. In terms of a spatial average, the SMOS L3 data was lower at 0.1337 $m^3/m^3$ than the SVAT model estimates at 0.1468 $m^3/m^3$, due to the use of a Dobson model in dry and sandy soils. In terms of latitudinal gradients, the spatial pattern of the SVAT model estimates was akin to that of the SMOS data. However, both estimates differently responded to rainfall and vegetation cover, suggesting the different systematic errors in each model structure. First, the SMOS data exhibited the rainfall-induced run-off errors, as shown in Figure 15-a. Although it was previously suggested that TRMM rainfall data contain a certain degree of biases and errors, the TRMM data errors were considered insignificant in this study area and used for assessing the SMOS L3 data. It is because the SMOS and TRMM data are independent but agreeable to each other. As shown in Figure 16, the rainfall that occurred on DoY 186 and 187 coincided with the enhancements of SMOS soil moisture on the following days. More specifically, subsequent to the rainfall on DoY 187 (Figure 16-b), significant run-off errors (shown dark

red in Figure 15-a) were observed over the same rainy area in the SMOS data.

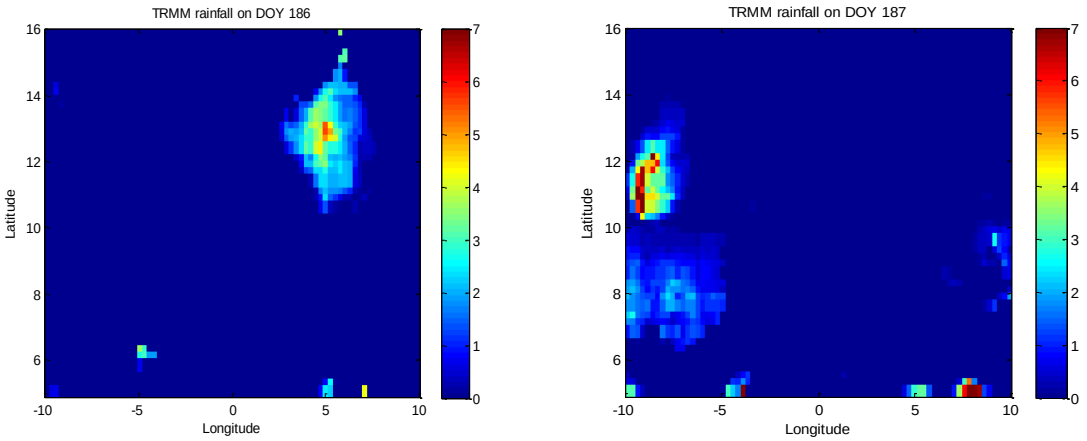


(a) (b)

Figure 16. TRMM rainfall events on (a) DoY 186 and (b) DoY 187, respectively. Unit: mm/hr.

As Pellarin et al. (2009) previously suggested that the soil crusting significantly contributes to run-off, the run-off errors was considered due to the infiltration decreased in clay soils (i.e. indicating higher clay fractions here than the adjacent area, according to the ECOCLIMAP datasets) and resultant water film formed on the soil surface. In contrast, since the rain events on DoY 186 (Figure 16-a) occurred over the soils showing the clay fractions of less than 10%, potentially higher infiltration rate was suggested, not leading to significant run-off errors in the rainy area of SMOS data. Secondly, the vegetation attenuation was suggested for the SMOS data. The SMOS data indicated that it is dry in vegetated patches. In contrast, as shown in Figure 15-b, the SVAT model showed that the vegetation zone is in wet conditions, which is positively correlated with a spatial distribution of LAI. The underestimation of the SMOS data was considered due to uncertainty of canopy temperature and vegetation optical thickness. It was suggested that the emission from vegetation decreases the soil moisture (Holmes et al., 2008). In addition to the effects of rainfall as well as vegetation mentioned so far, the penetration depth (usually much deeper in dry and sandy soils) different from the soil depth of SVAT model fixed at a depth of 5 cm was also suggested as the reason of a large discrepancy between the SVAT model estimates and SMOS data.

Unlike the SMOS data, the SVAT model estimates did not exhibit rainfall-induced run-off and vegetation attenuation. Only moderate increases in soil moisture were found in the

SMOS run-off areas, partially because the SVAT model calculates discharge and evapotranspiration as the sinks (Noilhan & Planton, 1989). Especially under very dry and sandy soil conditions, however, the SVAT model contains the sources of uncertainty different from the SMOS data. The performance of SVAT model is often limited by uncertainty in soil and hydraulic inputs (i.e., $C_1$ and $\theta_{geq}$ in Section 4.2.). $C_1$ is uncertain, because the vapor phase transfer was not included in the original land surface parameterization (Montaldo et al., 2001). Even the alternatively suggested Gaussian distribution formulation of $C_1$, expressed as a function of land surface temperature and wilting point, is often contaminated by uncertainty of wilting point information determined with site-specifically defined pedo-transfer functions (Braud et al., 1993; Pellarin et al., 2009). Furthermore, $\theta_{geq}$ is usually overestimated in sandy soils (Noilhan & Mahfouf, 1995). Finally, the use of satellite-retrieved rainfall data is a source of uncertainty. These factors might lead to some mis-estimation in the SVAT model.

2.3.3.3. Systematic error propagations of L-MEB forward model

To optimize the prior L-MEB radiative transfer model state ensembles used at the 1$^{st}$ step of the stationary EnKF, three different perturbation schemes shown in Table 1 were examined. The results are shown in Table 5, where spread was calculated by spatially averaging a standard deviation of ensemble anomalies. Additionally, correlation indicates a relationship between true field (i.e., SMOS L3 data) and ensemble mean. Among three schemes, scheme 2 (brightness temperature perturbation) showed the highest variance and ensemble spread, suggesting the lowest bias as well as highest sensitivity (Geman et al., 1992). Considering that a fundamental rationale of the EnOI scheme is that the variance of model represents the magnitude of forecast model errors (Oke et al., 2007), it was found that the SMOS retrieval errors can be largely amplified by brightness temperature measurement errors such as calibration error or RFI, according to these statistics in Table 5. In contrast, it was considered that the errors in *a priori* geophysical parameters and fractions were relatively less propagated to soil moisture errors than brightness temperature, and might be amendable while minimizing a cost function and updating parameters through the iterations in the SMOS retrieval algorithm. Accordingly, the ensemble of brightness temperature scheme was selected and used as the L-MEB model states in the 1$^{st}$ step of the stationary EnKF scheme, to empirically consider the SMOS retrieval errors in EnOI.

Table 5. Statistics of L-MEB model ensembles (SMOS L2 products)

| | Scheme 1(GH) | Scheme 2(TB) | Scheme 3(FR) |
|---|---|---|---|
| Spread | 0.0180 | 0.0385 | 0.0137 |
| Correlation | 0.8166 | 0.8037 | 0.7417 |
| Variance | 0.0003 | 0.0016 | 0.0002 |
| Spatial average | 0.1787 | 0.1631 | 0.1512 |

Note: GH: the perturbations of geophysical parameters; TB: the perturbations of brightness temperatures; FR: the perturbations of fractions. Unit: variance $[m^3/m^3]^2$, spread and spatial average $[m^3/m^3]$, and correlation [-].

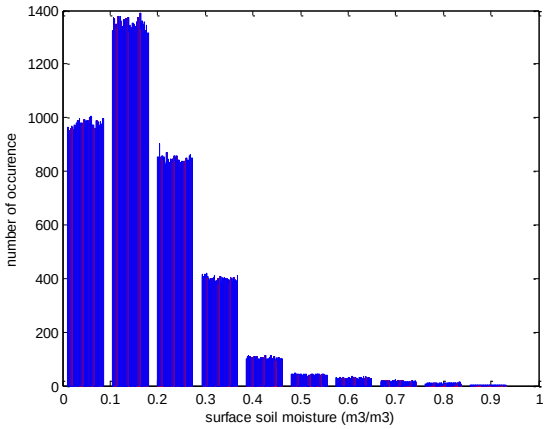


(a)

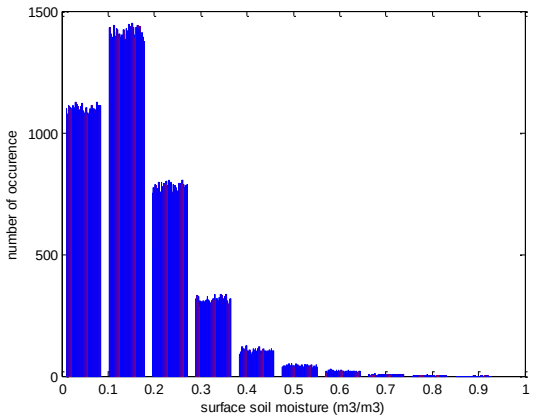


(b)

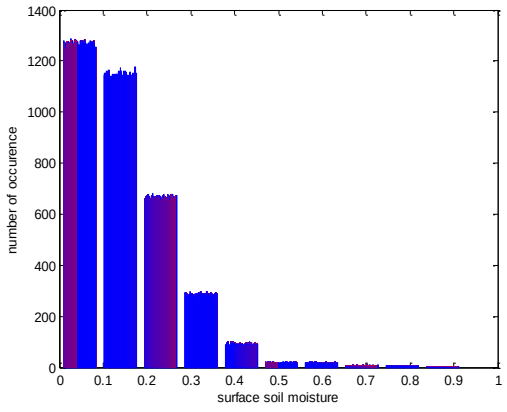


(c)

Figure 17. The ensemble members propagated by different perturbation regimes: (a) geophysical parameter (scheme 1); (b) brightness temperature (scheme 2); (c) fraction (scheme 3).

Based upon the ensemble propagations, a pattern of bias was also discussed. In Table 5, the fraction scheme showed the lowest spatial average. Similarly, as shown in frequency of Figure 17-c, the majority of the ensembles in fraction scheme were most frequently found in the lowest level groups of surface soil moisture (i.e., below 0.1 $m^3/m^3$), suggesting that any fraction error might be a source of surface soil moisture underestimation by the SMOS retrieval algorithm. In contrast to fraction scheme, the greater part of the ensembles in geophysical parameter and brightness temperature scheme were most frequently found in the moderately wet group (higher than 0.1 $m^3/m^3$), as shown in Figure 17-a and b. Additionally, considering the highest spatial average of geophysical parameter scheme at 0.1787 $m^2/m^2$ (Table 5), it may be suggested that any overestimated SMOS data may be related to *a priori* geophysical parameter errors.

2.3.3.4. Sequential EnKF

Table 6.The sequential EnKF results, unit: $m^3/m^3$

| Time step (DoY) | Surface soil moisture in Niger | | | | Surface soil moisture in Benin | | | | Spatial RMSE | Spatial average |
|---|---|---|---|---|---|---|---|---|---|---|
| | EnKF | FM | SMOS | SVAT | EnKF | FM | SMOS | SVAT | | |
| 182-184 | 0.0736 | 0.0640 | 0.0743 | 0.0244 | 0.2026 | 0.1707 | 0.2882 | 0.1746 | 0.0829 | 0.1767 |
| 184-186 | 0.0122 | 0.0432 | 0.0022 | 0.0196 | 0.2026 | 0.1707 | 0.2882 | 0.1746 | 0.0783 | 0.1551 |
| 186-188 | 0.0122 | 0.0432 | 0.0022 | 0.0196 | 0.2457 | 0.1326 | 0.3393 | 0.1421 | 0.0795 | 0.1516 |

*FM: field measurement, SMOS: SMOS L3 products

The sequential EnKF results were captured in the end of data assimilation on DoY 186 to 188. For a point-scale comparison, Table 6 shows the surface soil moisture of EnKF results, the original SMOS L3 data prior to any data assimilation, and SVAT model estimates shown at a single pixel nearest to the field measurement in the Niger and Benin sites. The EnKF results in Table 6 shows that after the sequential EnKF, the RMSE from field measurement on DoY 186 was reduced from 0.041 to 0.031 $m^3/m^3$ for the Niger site in very dry and sandy soils and from 0.207 to 0.113 $m^3/m^3$ for the Benin site in moderately wet conditions. The spatial RMSE shown in Table 6 presents a difference between the EnKF result and true field. The reduced RMSE of 0.08 $m^3/m^3$ on the approximate average suggested that EnKF successfully integrated model states with the observations. In contrast, before data assimilation, a spatial RMSE between SVAT model open-loop and the original SMOS L3 data was higher at 0.129 $m^3/m^3$.

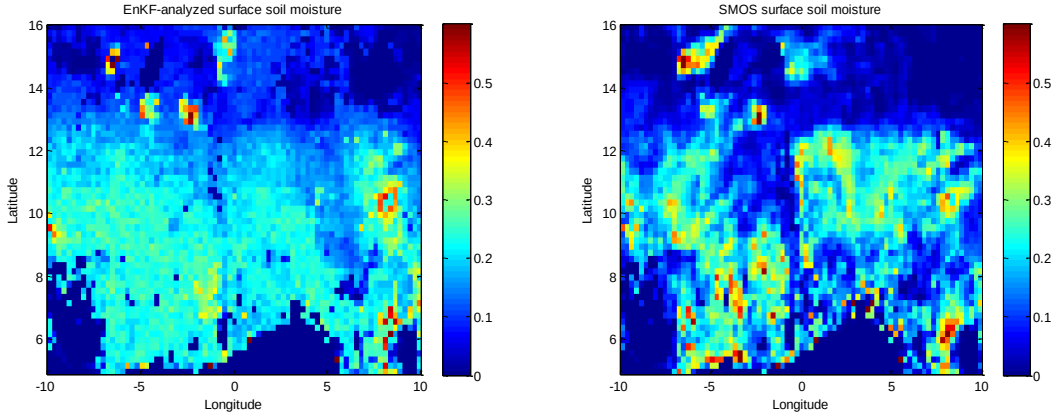


(a) (b)

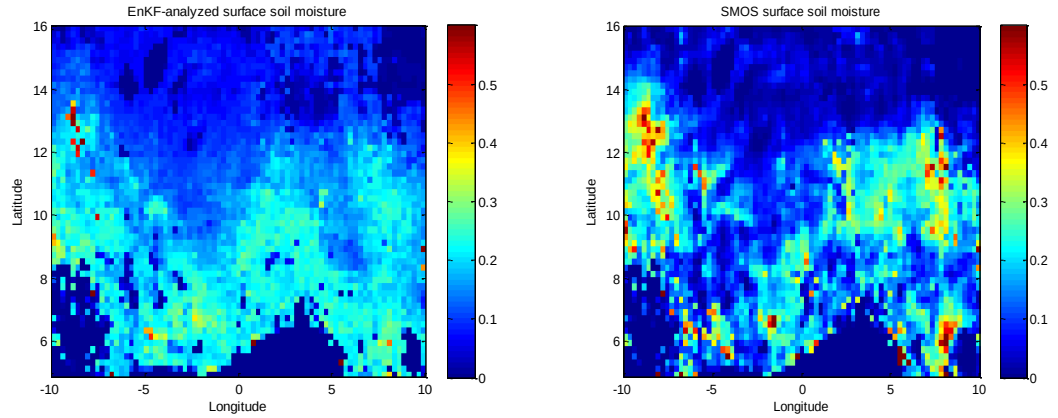

(c) (d)

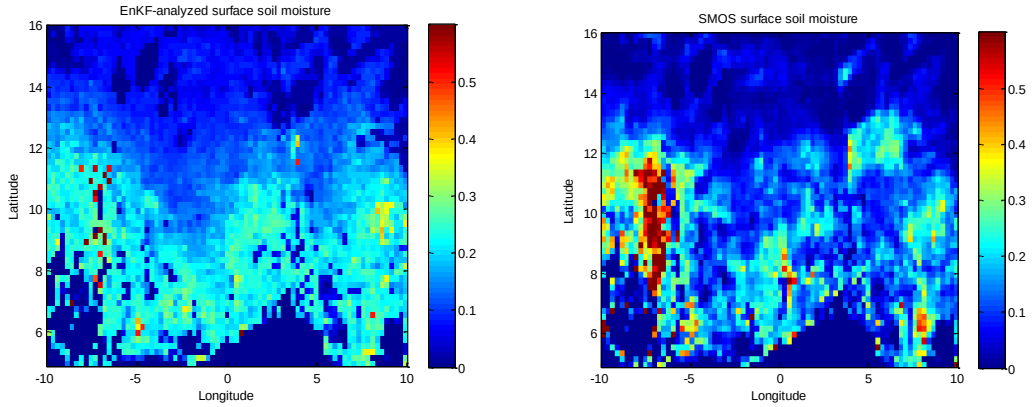


(e) (f)

Figure 18. Surface soil moisture estimates on multiple time steps, Unit: m3/m3: EnKF analysis on the left column and SMOS L3 data (true field) on the right column. (a) and (b): DoY 182 to 184; (c) and (d): DoY 184 to 186; (e) and (f): DoY 186 to 188.

The spatial comparisons between the sequential EnKF results on the multiple time steps and the original SMOS L3 data are provided, in Figure 18. The rainfall-induced run-off errors shown in SMOS L3 data (Figure 18-f) were significantly smoothed away in the EnKF scheme (Figure 18-e). It was considered because the SVAT model being independent from the rainfall-induced radiometric errors found in the SMOS data contributed to the EnKF analysis. Additionally, the SMOS soil moisture attenuated in vegetated areas was recovered in the EnKF scheme, showing a similar spatial distribution of LAI.

2.3.3.5. Stationary EnKF

The statistics of two-step stationary EnKF results are shown in Table 7, where ‘EnOI scheme’ indicates the results of the EnOI scheme assimilating the brightness temperature error-corrected SMOS data into the SVAT model on DoY 186-188. For the SMOS data error correction, prior to the EnOI, the SMOS L3 data was assimilated into three different L-MEB model ensembles (i.e. L2 products in Table4). These products are indicated by ‘EnOI: scheme 1, 2 and 3’, in Table 7.

Table 7. The two-step stationary EnKF results (DoY: 186-188), unit: $m^3/m^3$

| Method | Soil moisture in Niger | Soil moisture in Benin | Spatial RMSE | Spatial average |
|---|---|---|---|---|
| Field measurement | 0.0432 | 0.1326 | - | - |
| SMOS L2 | 0.0211 | 0.3425 | - | 0.1678 |
| SMOS L3 | 0.0022 | 0.3393 | - | 0.1337 |
| EnOI: scheme 1 (GH) | 0.0790 | 0.2584 | 0.1077 | 0.1832 |
| EnOI: scheme 2 (TB) | 0.0346 | 0.1573 | 0.0907 | 0.1515 |
| EnOI: scheme 3 (FR) | 0.0817 | 0.2526 | 0.1022 | 0.1672 |
| Sequential EnKF | 0.0122 | 0.2457 | 0.0795 | 0.1516 |

For a point-scale comparison, the 2nd and 3rd column of Table 7 shows the surface soil moisture of EnKF results, and the original SMOS data shown at a single pixel nearest to the field measurement in the Niger and Benin sites. Compared to the original SMOS L2 and L3 data, the EnOI (scheme 1 to 3) significantly reduced a difference from the field measurements. For a point-scale comparison, the 2nd and 3rd column of Table 7 shows the surface soil moisture of EnKF results, and the original SMOS data shown at a single pixel nearest to the field measurement in the Niger and Benin sites. Compared to the original SMOS L2 and L3 data, the EnOI (scheme 1 to 3) significantly reduced a difference from the field measurements. Although the same SVAT model states were used for all EnOI schemes, the best improvement was found in scheme 2 (brightness temperature), demonstrating the main source of errors was brightness temperature. In detail, after two-step stationary EnKF, the RMSE from the field measurements significantly decreased from 0.0410 $m^3/m^3$ to 0.0086 m3/m3 for the Niger site, and from 0.2067 $m^3/m^3$ to 0.0247 $m^3/m^3$ for the Benin site. The more improvement in the Niger site (i.e. RMSE: 0.0086 $m^3/m^3$) than the Benin site (i.e. RMSE: 0.0247 $m^3/m^3$) was considered because a SMOS L2 processor used a Mironov formulation as a dielectric constant model over dry and sandy soils for the generation of L-MEB forward model state ensembles in the 1st step, unlike the SMOS L3 data.

As shown in Table 7, this can be reinforced by the fact that the SMOS L2 product (0.0211 $m^3/m^3$) of L2 processor in the dry and sandy Niger site was more similar to field measurement (0.0432 $m^3/m^3$), than the original SMOS L3 data (0.0022 $m^3/m^3$). The RMSE reduction level of two-step stationary EnKF was more considerable than the sequential EnKF (i.e. RMSE: 0.031 $m^3/m^3$ for the Niger site, and 0.113 $m^3/m^3$ for the Benin site), as shown in Table 7. The reason was considered because the sequential EnKF did not empirically take into account of the error propagation of L-MEB forward model but aprioristically used the variance for the observation errors (Reichle, 2008). It was thought that as the analysis gradually converged towards true field, the SMOS L3 data errors were transferred to the

EnKF analysis. In terms of a spatial average, two-step stationary EnKF with brightness error corrections was just same with a sequential EnKF. More specifically, in Table 7, in contrast to scheme 1 (0.1832 $m^3/m^3$) and scheme 3 (0.1672 $m^3/m^3$), only two-step stationary EnKF scheme 2 (0.1515 $m^3/m^3$) was comparable to the sequential EnKF (0.1516 $m^3/m^3$), suggesting the performance of EnOI is just comparable to the sequential EnKF. The spatial average of scheme2 was still higher than the original SMOS L3 data (0.1337 $m^3/m^3$), because scheme 2 solved the underestimation problem by means of a Dobson model through a L2 processor. Therefore, based upon the spatial average, and point-scale validation, it was concluded that the EnOI can provide the optimal values, if brightness temperature errors and biases in the SMOS L3 data are empirically defined by means of L-MEB radiative transfer model. It was also suggested that a quality of brightness temperature is very significant for the success of data assimilation, and may reduce a computation cost of the sequential EnKF scheme.

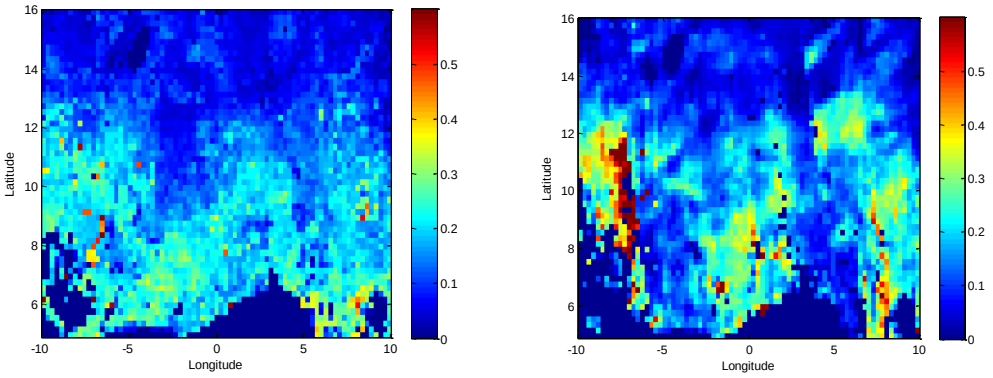


(a) (b)

Figure 19. Comparison in surface soil moisture: (a) two-step stationary EnKF (brightness temperature scheme); (b) SMOS L2 data (open-loop of the 1st step EnKF), unit: $m^3/m^3$.

Figure 19 further illustrates a spatial distribution of two-step stationary EnKF results (scheme 2), being compared to the original SMOS L3 data prior to any data assimilation. It was found that the rainfall-induced run-off (or ponding) errors (red-colored spikes in the SMOS data in Figure 18-f and 19-b) were significantly mitigated in two-step stationary EnKF scheme 2. It could be attributed to the brightness temperature measurement errors by rain. In contrast, although SMOS L2 data solved the underestimation errors arising from the dielectric constant model used in L3 data, the rainfall (on DoY 187 in Figure 16-b) -induced brightness errors still remained in L2 data without any data assimilation. Although run-off errors were removed, the rain activities on DoY 186 (Figure 16-a) were appropriately

expressed in two-step stationary EnKF (Figure 19-a) better than the sequential EnKF (Figure 18-e). Next, the vegetated attenuations in the SMOS L3 data were recovered in this stationary EnKF scheme, showing the wet conditions generally consistent with a spatial distribution of LAI. To sum up, it was suggested that in the 1st step of the stationary EnKF, the brightness temperature measurement errors (i.e., the underestimations by means of a Dobson model in dry and sandy regions or the run-off errors by rain events) were alleviated by L-MEB forward model. In the 2nd step, it was suggested that the SVAT land surface model state ensembles with systematic error structures different from the SMOS retrieval algorithms mitigated the vegetation attenuation in the SMOS data

2.3.3.6. Conclusion & Summary

To compare the effects of sequential forecast error evolution with those of empirical observation error correction by means of L-MEB radiative transfer model, we examined two different EnKF schemes: the sequential EnKF assuming a time-invariant global constant a priori variance for considering observation errors versus the stationary EnKF empirically rectifying the observation errors. The two-step stationary EnKF scheme corrected the brightness temperature measurement errors and biases with the L-MEB model state ensembles in the 1st step, and assimilated the products in the 1st step to the SVAT model through the EnOI. The local point-scale comparison data showed that the two-step stationary EnKF scheme was better matched with field measurements than sequential EnKF and the original SMOS data. The spatial comparison exhibited that the two-step stationary EnKF scheme successfully mitigated the rainfall-induced run-off errors, the vegetation attenuation and dielectric constant model errors found in SMOS L3 data. The spatial average of two-step stationary EnKF (brightness temperature scheme only) was just comparable to that of the sequential EnKF. Therefore, it was concluded that the main source of SMOS data was brightness temperature error, and the two-step stationary EnKF empirically defining the observation errors with radiative transfer model was more effective than the sequential EnKF scheme using the a priori variance for observation error. The two-step stationary EnKF approach offers several operational advantages in that this scheme does not require a long record (usually at least one year) of satellite data like Cumulative Distribution Functions (CDF) matching technique and sequential EnKF. Additionally, because this scheme takes into account the spatially heterogonous and time-variant observation biases and errors, there is no need to assume a slow evolution of the observation errors and biases or to define a global constant for bias parameter in observation operators or to determine the length of the localising function in EnKF for sampling errors.

According to the error propagation analysis of L-MEB model ensembles, it was suggested that a priori geophysical parameter and fraction errors (or adversely influencing the selection of retrieval model) were relatively amendable by iterations in a SMOS retrieval algorithm, as compared with the brightness temperature errors, meaning that a quality of brightness temperature is crucial for the successful retrieval of SMOS data. The fraction errors exhibited biases towards underestimating surface soil moisture.

CHAPTER 3

# Inversion I: Aerodynamic Roughness from Heat Flux

In this Section [*], the aerodynamic roughness in the SEBS model was inverted from the heat flux measurements. For a successful inversion, it is crucial to filter out the heat flux measurement errors through the appropriate data assimilation, because the measurements are usually interfered by the instrument calibration error or the use of assumption inapplicable to the specific study site. Several studies previously applied the data assimilation to the parameter estimation. Goegebeur and Pauwels (2007) compared the performance of extended Kalman filter with the PEST method minimizing an objective function, as briefly discussed in Section 1.2.. The latter is different from the extended Kalman filter minimizing a square error with the observations. After applying these two algorithms into a conceptual rainfall-runoff model, this study concluded that the extended Kalman filter performed better than the objective function minimization methods, since it can accommodate the high observation error, a low frequency of observation update, and erroneous initial parameters. Pauwels et al. (2009) further employed the extended Kalman filter for parameter estimation. By combining

*This chapter is based upon Lee et al. (2012b)

a land surface model and remote sensing data, they estimated three soil hydraulic model parameters in TOPLATS (TOPMODEL based Land Atmosphere Transfer Scheme) – i.e. saturated hydraulic conductivity, pore size distribution index, and bubbling pressure. After a calibration of these parameters, the model output successfully reached an agreement with SAR-retrieved surface soil moisture. However, one of the well-known drawbacks in the extended Kalman filter is that when a system is highly nonlinear, as in hydrological applications, the extended Kalman filter tends to be unstable. This instability or divergence of the extended Kalman filter is due to the inappropriate approximation over-simplified by ignoring the higher order of derivatives and just using the first order Taylor series of a linear model (Moradkhani et al., 2005). On the other hand, the EnKF appropriately accommodates a nonlinear system with a better stability (Evensen, 2004, Margulis et al., 2002, Moradkhani et al., 2005, Reichle et al., 2002, Reichle, 2008). Additionally, EnKF does not require solving *a priori* model state, since it uses the model ensemble (Moradkhani et al., 2005). Theoretically, it requires the joint Gaussian probability distribution between the measurements and propagated states, based upon Bayes theorem. However, in several cases of nonlinear hydrological applications, it was reported that the EnKF can also handle the non-Gaussian or non-additive noise (Margulis et al., 2002, Dunne et al., 2005).

This thesis suggests a versatile in terms of dynamics and simple approach appropriately extracting aerodynamic roughness height from single or two heat flux estimates. With respect to previous studies, the new aspects and advantages of this study is (1) that this study provides an operational frame implementing EnKF with the SEBS model ensembles; (2) that the inverse method of this study requires the smaller number of inputs – i.e. only sensible heat flux – than the cost function approach minimizing the MOS relationships (Yang et al., 2003); (3) that this is less affected by the vegetation attenuation or saturation problem of remotely sensed Vegetation Indexes (VIs) than the Massman methods (Massman, 1997); (4) that this is time-variant in comparison with the literature values and the GIS-based land use map or ECOCLIMAP being constant, regardless of Monsoon-induced vegetation dynamics or heat transfer (as in the AROME model); (5) that this is applicable to a large scale where the eddy covariance data is not available. This Section is organized as follows: the field measurement method is provided in Section 3.1. The theoretical basis of SEBS model is provided in Section 3.2. In the Section 3.3., the inverse method, and result of the Tibet-GAME datasets are presented. Here, the inverted aerodynamic roughness is compared with the literature value, and other approaches such as eddy covariance or vegetation index formulation by Massman methods. The SEBS model-simulated heat flux outputs are compared before and after calibration. In Section 3.4, the same inverse method is applied to the Landriano site in different climatic conditions from Tibet – i.e. moderately wet soils.

### 3.1. Field Measurements

3.1.1. Eddy Covariance (EC) method for estimating aerodynamic roughness

In general, aerodynamic roughness height is referred to as the height where the logarithmic wind profile reaches to zero. If the EC data is available at a local-point scale, the independent wind profile method is usually employed (Yang et al., 2008), as follows:

$$z_{om} = z \exp\left(-\frac{ku}{u*} - \psi\right) \qquad (4\text{-}1)$$

where, K is the von karman constant, $u$ is the horizontal velocity, $u$* is the friction velocity, z is the measurement height. ψ is the atmospheric stability correction as a function of Obukhov length (Ma et al., 2008). The estimation of aerodynamic roughness is usually performed under neutral (i.e. ψ = 0) condition when the turbulent transfer coefficient for humidity and temperature is considered to be equivalent (Kohsiek et al., 1993, Tsuang et al., 2003). However, other researchers suggested to include all the atmospheric stability conditions or to use the turbulent data under unstable and highly convective conditions only (Yang et al., 2003).

3.1.2. BREB method for heat flux

Although due to the absence of the EC data at the BJ station during the experiment period, it was not possible to estimate the field measured aerodynamic roughness described in 3.1.1. Instead, the heat fluxes were measured with the Bowen Ratio Energy Balance (BREB) method. The measurements in the same experiment site were previously validated with the EC data (van der Velde et al., 2009). The BREB method determines the heat flux using the temperature and vapor pressure gradients, as follows (Perez et al., 1999):

$$\text{Bowen ratio } (\beta) = \frac{H}{LE} = \gamma \frac{T_1 - T_2}{e_1 - e_2} \qquad (4\text{-}2)$$

where, $e_1$ and $e_2$ are the vapor pressure measurements [kPa] observed at two different levels ($Z_1$=8.2m and $Z_2$=1m, respectively), while $T_1$ and $T_2$ are the air temperature [K] measured at those heights ($Z_1/Z_2$>4) and γ is the psychometric constant [kPa/K]. This Bowen ratio is further used to calculate the heat fluxes using surface energy balance.

$$\lambda E = \frac{R_n - G_o}{1+\beta} \qquad (4\text{-}3) \qquad \text{and} \quad H = \frac{\beta}{1+\beta}\left(R_n - G_o\right) \qquad (4\text{-}4)$$

where, $G_o = K_h \frac{T_{skin} - T_s}{dz}$ (4-5) and $R_n = R_{is} - R_{os} + R_{il} - R_{ol}$ (4-6)

Ground heat flux ($G_o$) was determined by the thermal conductivity $K_h$ [W/mK] as a function of soil moisture contents [$m^3/m^3$]. z is the soil depth. $T_{skin}$ is the surface temperature. $T_s$ is the soil temperature at a depth of 0.05 m (van der Velde et al., 2010). Net radiation ($R_n$) was calculated from the sum of inward ($R_{is}$), and outward short wave radiation ($R_{os}$), and inward ($R_{il}$), and outward ($R_{ol}$) long wave radiation, each component of which was measured from the radiation sensors installed at a local station (van der Velde et al., 2009).

To acquire the quality of data, this study rejected most of the uncertain data irrelevant to aerodynamic roughness momentum activity, according to following criteria:

- Turbulent data with β below -0.7 were excluded, to forbid the latent heat sign error occurring during night time (Perez et al.,1999, Tsuang et al., 2003).
- Heat flux values with incorrect sign were further excluded, according to flux and gradient relationship (i.e. latent heat has an opposite sign with respect to specific humidity gradient) (Ohmuka,1982). Accordingly, the entire data showed negative humidity gradient, suggesting positive latent heat (evaporation).
- To isolate the turbulent characteristics governing aerodynamic momentum roughness, the wind measurement with a low velocity (i.e. $U_2$ <1 m/s) and a small wind velocity gradient (i.e. $U_1$-$U_2$<0.3 m/s) as well as low friction velocity were also neglected (Liu & Foken, 2001).
- In arid region such as the Naqu sites, since temperature gradient is usually considered more significant than the vapour gradient, data with a low temperature gradient ($T_2$ - $T_1$ <0.1K) were discarded (Yang et al., 2003).
- Sensible heat fluxes below 10 $W/m^2$ were also excluded to identify convective condition (Yang et al., 2003).

This filtering resulted in sensible heat under free-convective turbulent conditions (i.e. H> 50 $W/m^2$).

### 3.2. SEBS model

The SEBS model was developed to estimate the atmospheric fluxes on the large to

global scale using satellite earth observation data. As the inputs, it requires the land surface parameters such as canopy height, emissivity, albedo and LAI, and the meteorological turbulent data such as wind speed and humidity as well as the radiation. Unlike the energy balance closure approach, it estimates the sensible heat flux from the MOS equations. It determines latent heat from evaporation fraction. The evapotranspiration products of the SEBS model are available to general public (http://wacmos.itc.nl). The relevant theoretical description is presented below.

3.2.1. Roughness lengths

In SEBS, displacement height and aerodynamic roughness length are estimated, as follows (Massman, 1997, Su et al., 2001, Su, 2002):

$$d_0 = h_c\left(1-\frac{1}{2n_{ec}}\exp\left(-2n_{ec}\right)\right) \quad (4\text{-}7)$$

$$z_{0m} = h_c\left(1-\frac{d_0}{h_c}\right)\exp\left(-k\frac{u(h_c)}{u_*}\right) \quad (4\text{-}8)$$

where, $h_c$ is the canopy height as a function of MODIS NDVI, $d_o$ is the displacement height. The within-canopy-extinction $n_{ec}$ is further formulated below.

$$n_{ec} = 2C_d LAI\left(\frac{u(h_c)}{u_*}\right)^2 \quad (4\text{-}9)$$

where, $C_d$ is a drag coefficient of foliage, LAI is the Leaf Area Index. In this study, LAI was formulated as a function of MODIS NDVI, to reduce the number of inputs disturbing for the perturbation of aerodynamic roughness later in the EnKF scheme. Consequently, if perturbing the single input of NDVI, its errors are propagated to the LAI, $h_c$, $d_o$, and $z_{om}$, as shown in error propagation of Section 3.3.2.1. $u(h_c)/u^*$ was determined from the Massman methods (Su et al., 2001). Additionally, by following land surface parameters for mixed canopy and soil, the thermal roughness height is related to the aerodynamic roughness height (Choudhury and Monteith, 1988).

$$kB^{-1} = \log\left(\frac{z_{0m}}{z_{0h}}\right) \qquad (4\text{-}10)$$

where, $kB^{-1}$ is an excess resistance to heat transfer. For bare soil surface, it is expressed as a function of roughness Reynolds number. For a canopy landscape, it is parameterized with leaf heat transfer coefficient, fractional canopy coverage, and within-canopy wind speed profile extinction coefficient (Su et al., 2005). Thermal roughness length $z_{oh}$ can be estimated from $kB^{-1}$ and (4-8).

3.2.2. Heat Flux

The roughness heights for heat and momentum (resp. $z_{oh}$ and $z_{om}$) are further used in the MOS relationships for the profiles of the mean wind speed, and the mean temperature gradient $T_o - T_a$ (where, $T_o$ is the potential temperature at the surface, $T_a$ is the potential air temperature at the measurement height z), as follows (Su et al., 2002):

$$u = \frac{u^*}{K}\left[\ln\left(\frac{z-d_o}{z_{om}}\right) - \psi_m\left(\frac{z-d_o}{L}\right) + \psi_m\left(\frac{z_{om}}{L}\right)\right] \qquad (4\text{-}11)$$

$$T_o - T_a = \frac{H}{Ku^*\rho C_P}\left[\ln\left(\frac{z-d_o}{z_{oh}}\right) - \psi_h\left(\frac{z-d_o}{L}\right) + \psi_h\left(\frac{z_{oh}}{L}\right)\right] \qquad (4\text{-}12)$$

where, L is the Obukov Length, ρ is the density of dry air [kg/m$^3$], $C_p$ is the heat capacity [J/kgK].

The sensible heat H estimated by the iterations using the MOS relationships illustrated above is used for determining the latent heat. More specifically, H is used for estimating the relative evaporation in (4-13), which is further used for estimating the evaporative fraction in (4-16), the ratio of heat fluxes on hypothetical conditions (sensible heat in the hypothetically wet/dry condition, and residual latent heat in wet condition) to available energy, and finally latent heat in (4-18) (Su et al., 2002).

$$\text{The relative evaporation } \Lambda_r = 1 - \frac{H - H_{wet}}{H_{dry} - H_{wet}} \qquad (4\text{-}13)$$

where, sensible heat in dry condition $H_{dry}$ is directly approximated by $R_n - G_o$, assuming that latent heat is zero (i.e. $\lambda E_{dry}=0$).

Sensible heat in wet condition $H_{wet}$ is formulated, as follows:

$$H_{wet}= [(R_n-G_o) - \frac{C_p \rho_{air}}{r_a}(e_{sat} - e_a)] \frac{\gamma}{\Delta + \gamma} \quad (4\text{-}14)$$

$$\text{where, } r_a= \frac{1}{Ku^*}\left[\ln\left(\frac{z-d_o}{z_{oh}}\right) - \psi_h\left(\frac{z-d_o}{L_{wet}}\right) + \psi_h\left(\frac{Z_{oh}}{L_{wet}}\right)\right] \quad (4\text{-}15)$$

where, $r_a$ is aerodynamic resistance to heat transfer [s/m]. $e_a$ is actual vapour pressure at reference height [Pa], while $e_{sat}$ is the saturation vapour pressure at the reference heights [Pa]. $L_{wet}$ is the wet-limit stability length. $\Delta$ is the change rate of saturation vapour pressure with temperature.

The relative evaporation in (4-13) is further used for estimating the evaporation fraction, as follows:

$$\text{The evaporative fraction } \Lambda = \frac{\Lambda_r \lambda E_{wet}}{R_n - G_0} \quad (4\text{-}16)$$

$$\text{where, } \lambda E_{wet} = R_n - Go - H_{wet} \quad (4\text{-}17)$$

$$\text{Finally, latent heat is } \lambda E = \Lambda(R_n - G_o) \quad (4\text{-}18)$$

### 3.3. Case study I: Tibet-GAME datasets

Experiment was conducted with the Tibet-GAME datasets collected from a BJ station shown in Figure 1(van der Veldel et al., 2009). Those meteorological measurements were used for running the SEBS model.

#### 3.3.1. EnKF-based inverse method

*Experimental setup for EnKF*

In the inverse method of this study, the EnKF is used to compensate for the limitations and systematic errors of the model and observation. If not using the EnKF scheme integrating the *a priori* model states with the observations, the errors of the field measurement can be significantly propagated in the inverse method because the field measure is used as the

reference data inferring from. In this study, the BREB method was used for the field measured heat fluxes because the relatively more accurate EC data are not available in experimental site and period. The BREB method incorrectly assumes the energy balance closure, although the imbalance of the surface energy budget has been widely observed (Liu & Foken, 2001). The energy balance un-closure is not simply due to the EC measurement errors or uncertainty of storage term but due to more complicated land surface circulation not appropriately defined (Foken, 2008). In addition, the SEBS model has also uncertainty in the MOS relationships used for the iterations. The parameters such as friction velocity or Monin-Obukov length estimated from the iterations of MOS relationships often showed discrepancies from the EC data. Therefore, by EnKF, the *a priori* model states contaminated by uncertain aerodynamic roughness, but independent from the inappropriate energy balance closure assumption of the BREB method were integrated with the BREB field measurements independent from SEBS-simulated aerodynamic roughness errors, but interfered by the incorrect assumption of energy balance closure. More specifically, field measured heat flux estimates were true field (i.e. the observations before taking into account of observation errors), while the *a priori* model state ensembles came from the SEBS model. Due to a lack of the EC data in the experiment site, and accordingly the absence of aerodynamic roughness measurement, as briefly described in 3.1.2, the parameter could not be assimilated by the EnKF scheme. In addition, Moradkhani et al. (2005) previously reported that the parameters perturbed are not efficiently converged, even after a long period of assimilation time step.

Hence, instead of parameters, the SEBS-simulated sensible heat was updated with the BREB-measured sensible heat through the sequential EnKF scheme described in 2.2.2.1. For the generation of model ensemble, the SEBS model was perturbed with the MODIS NDVI, assuming the Gaussian distribution. The variance of NDVI was determined, based upon the Normalized Rmse Ratio described in Moradkhani (2005). The NRR is defined as time averaged RMSE over ensemble-averaged RMSE, and was previously used to evaluate and quantify the ensemble spread. Out of 20 experimental cases (i.e. NDVI variance ranging from 8% to 50%; ensemble size ranging from 20 to 100), the ensemble pool group (i.e. ensemble size=100, variance=30%) showing the $NRR_H$ of 1.05 and the $NRR_{LE.}$of 1.1 was selected. For information, the perfectly optimal and ideal NRR value is a unity. The number of the observations updated at each assimilation step was equivalent to the number of the model states. Inflation was set to 1.01. Observation variance used for perturbing the observations and considering the observation errors was set at 10 $W/m^2$, based upon the aprioristically defined errors from Foken (2008). Localization was not carried out.

*Experimental setup for inverse method*

The fundamental conceptual schematic diagram of the EnKF-based inverse method is illustrated in Figure 20.

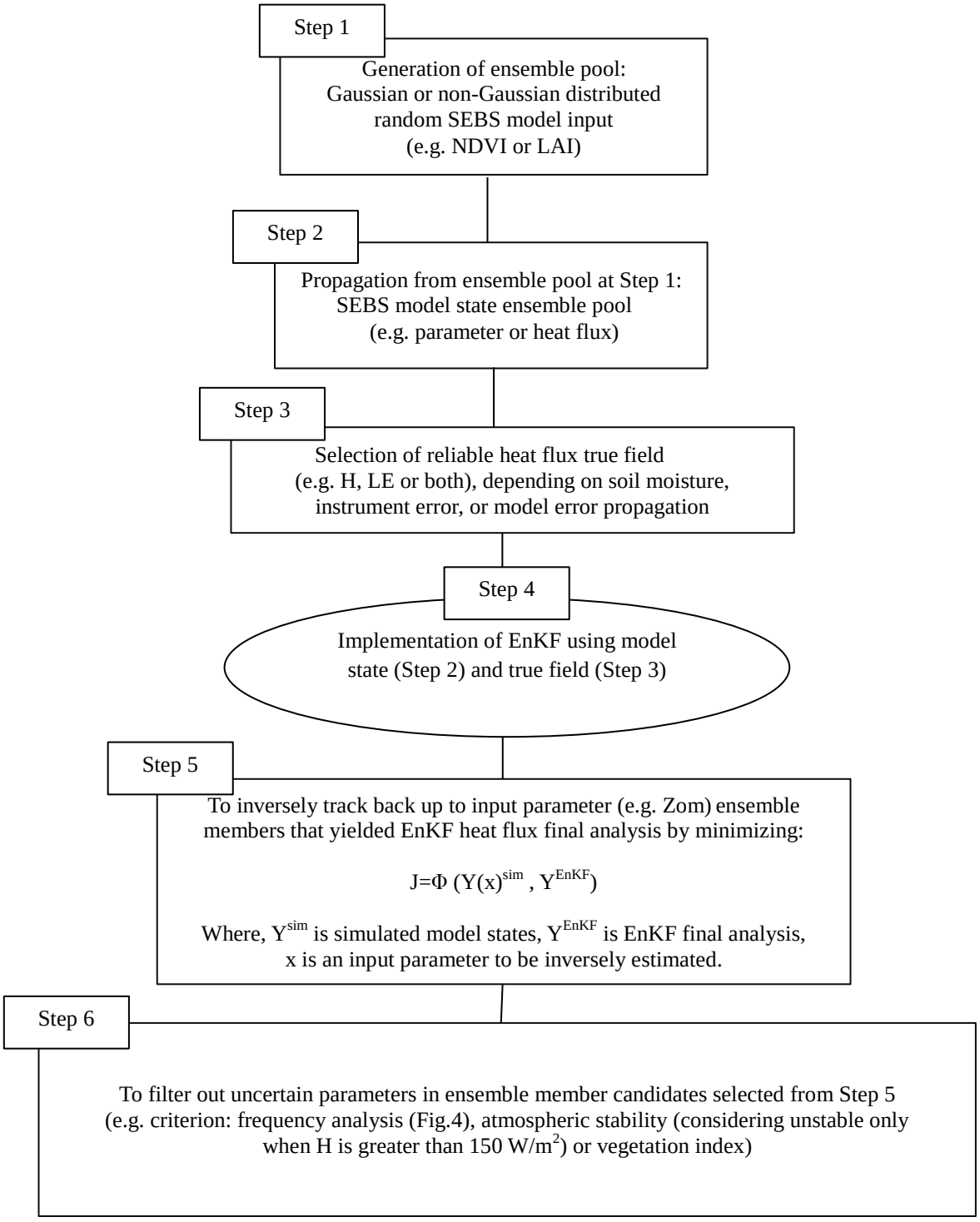


Figure 20. The conceptual diagram for the determination of aerodynamic roughness

By perturbing the NDVI, the input of SEBS model, in step 1, the heat flux ensemble pool was generated in step 2. In step 3, based upon the instrument errors and climatic conditions, as briefly discussed in 3.3.2.1, sensible heat was selected for EnKf. After implementing EnKF in step 4, the inverse method was carried out by minimizing the differences between measurements and SEBS model estimates in step 5. This step was also further constrained with additional site information in step 6.

### 3.3.2. Discussions & Results

#### 3.3.2.1. EnKF results

Only sensible heat was analyzed by the EnKF scheme for various reasons. The EnKF results were used for inverting the aerodynamic roughness. First, in general, it is considered that the latent heat in arid regions suggests a high degree of uncertainty in measurement. It was previously found that moisture flux is vulnerable to measurement errors in arid regions, since the temperature gradient is greater than specific humidity or vapor pressure (Boulet et al., 1997, Jochum et al., 2005, Prueger et al., 2004, Weaver et al., 1992). Second, according to the energy budget analysis over the Tibetan Plateau, sensible heat is the dominant energy in ABL, suggesting its major role (Ma et al., 2009). Finally, in SEBS, as briefly described in Section 3.2.2., sensible heat can amplify or propagate its errors to latent heat. Therefore, it was concluded that the errors in latent heat were considered larger than the sensible heat.

Furthermore, the Gaussian error propagated through SEBS model structure was analyzed, according to Marx et al. (2008). The variance $\delta^2_{\mathrm{LE}}$ and $\delta^2_{\mathrm{H}}$ demonstrated below showed that the errors propagated from aerodynamic roughness are more considerable in latent heat than sensible heat.

$$\delta^2_{\mathrm{LE}} = \left(\frac{\partial LE}{\partial z_{om}}\right)^2 \delta^2_{Zom} + \left(\frac{\partial LE}{\partial LAI}\right)^2 \delta^2_{LAI} + \left(\frac{\partial LE}{\partial h_c}\right)^2 \delta^2_{hc} + \left(\frac{\partial LE}{\partial z_{oh}}\right)^2 \delta^2_{Zoh} + \left(\frac{\partial LE}{\partial d_o}\right)^2 \delta^2_{do}$$

$$\delta^2_{\mathrm{H}} = \left(\frac{\partial H}{\partial z_{om}}\right)^2 \delta^2_{Zom} + \left(\frac{\partial H}{\partial h_c}\right)^2 \delta^2_{hc}$$

In detail, for various aerodynamic roughness inputs ranging from 0.015m to 0.055m (mean: 0.035 m; standard deviation: 0.016 m), the variances of sensible and latent heat propagated through SEBS was estimated at 225 and 331 $[\mathrm{W/m^2}]^2$, respectively, suggesting the errors in latent heat is more sensitive to the errors in aerodynamic roughness. As shown above, one of the reasons is that in SEBS, latent heat is interfered by several other input errors (i.e.

LAI, $h_c$, $z_{oh}$, $d_o$ propagated by NDVI) in addition to $z_{om}$, while sensible heat mostly affected by $z_{om}$. In specific, the variances in latent heat were very large at 20931 $[W/m^2]^2$ by displacement height errors, 663 $[W/m^2]^2$ by thermal roughness height errors, 136 $[W/m^2]^2$ by canopy height, and 100 $[W/m^2]^2$ by LAI, while there was only minor errors in sensible heat (i.e. variance: 89 $[W/m^2]^2$) by canopy height other than $z_{om}$. Accordingly, the sensible heat with less interference was selected to directly invert the aerodynamic roughness height from that. The EnKF-analyzed sensible heat was shown below in Figure 21. After EnKF, the RMSE between the EnKF-analyzed sensible heat and the BREB measurement was reduced to 17 $W/m^2$ (open-loop: 65 $W/m^2$).

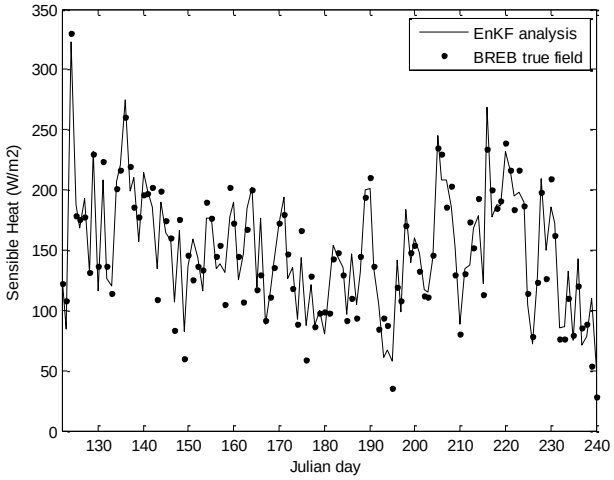


Figure 21. Daily average sensible heat estimated by EnKF analysis

3.3.2.2. Inversion of aerodynamic roughness

The aerodynamic roughness minimizing a mismatch between the SEBS-simulated sensible heat and EnKF final analysis was selected from the ensemble pool, as shown in Figure 20. Some additional constraints were used. During the pre-Monsoon period of highly unstable and free convective condition when sensible heat is greater than latent heat, only the day-time unstable sensible heat flux (>150 $W/m^2$) was used for inversion (Prueger et al., 2004, de Bruin et al., 1997). Since aerodynamic roughness is usually widely spread, showing a high standard deviation as illustrated in Figure 22, only the values the most frequently found in the ensemble pool were selected as the final estimates (Yang et al., 2008).

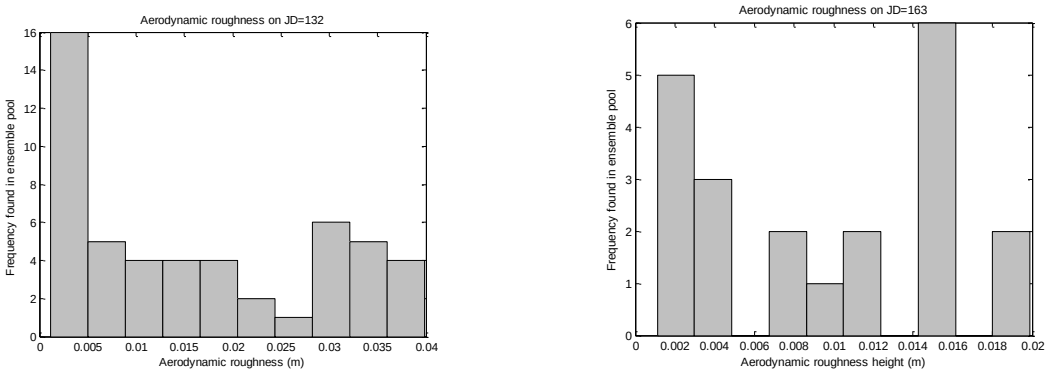


(a) (b)

Figure 22. Frequency of aerodynamic roughness: (a) Julian day 132, and (b) 163.

As shown in Figure 23, the resultant aerodynamic roughness height well reflected the vegetation effects, being consistent with the NDVI and LAI patterns (refer to Figure 4) and being agreeable with the bare soil conditions around till Julian day 150. The time-variant aerodynamic roughness showed a mean of 0.0098 m, and standard deviation of 0.0063 m, ranging from 0.0029 to 0.0186 m. This estimate was consistent with the literature value for grasslands (i.e. 0.01m, according to Beljaars et al. (1983)). However, the inverted estimation is more advantageous than the literature value, since it is time-variant. The result was also agreeable with the previous study that estimated aerodynamic roughness with the EC data over the same Naqu site (Yang et al., 2003).

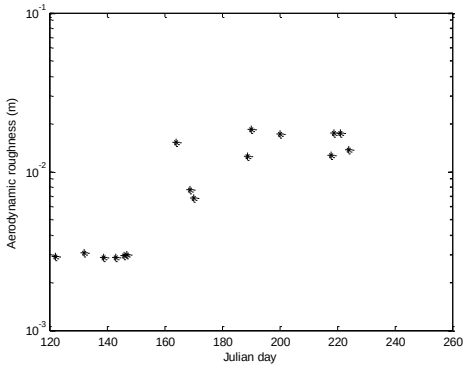


Figure 23. Inverted aerodynamic roughness height

3.3.2.3. Validation with the heat flux

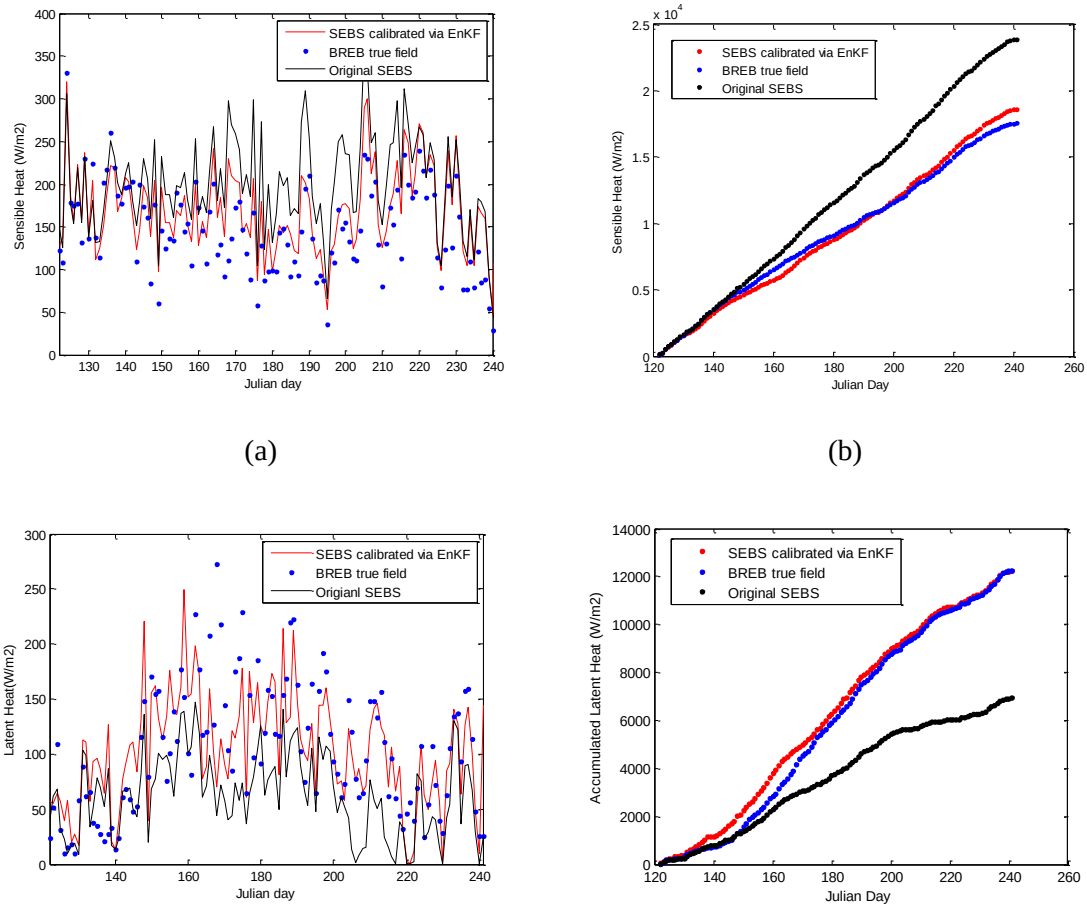


Figure 24. Comparison in heat flux estimates:
(a) sensible heat; (b) accumulated sensible heat; (c) latent heat; (d) accumulated latent heat.

The inverted aerodynamic roughness height was inserted into the SEBS model to examine its influence over the estimation of heat flux and energy source partitioning. The large improvement was found in the wet condition, because the error is usually proportional to the quantity. Especially, around DoY 180 during the summer Monsoon period, as shown in Figure 24, large discrepancies in heat flux estimates were noticed. However, the EnKF-based inverse method provided the very appropriate intermediate estimations between two extremes of the original SEBS and the BREB measurement. This is a good improvement, because both SEBS and BREB method suggests the large errors in this experiment site and period. First, it is considered that the original SEBS estimates were significantly biased by the errors in aerodynamic roughness input significantly higher than the literature value, as shown in

Figure 4. Similarly, the BREB measurements without data assimilation were also considered uncertain due to the inappropriate assumption of energy balance closure, because it was previously reported that the surface energy balance is not closed in this region (Ma et al., 2009). Finally, due to the considerable increments in precipitation and surface soil moisture during the Monsoon period, as demonstrated in Figure 25, the latent heat higher than the original SEBS were considered plausible (Margulis et al., 2002). When suggesting a positive relationship between latent heat and soil moisture, the interference by soil texture was ignored, because loamy sand was previously observed in the Naqu site (Su et al., 2011), instead of clay significantly preventing the evaporation activity.

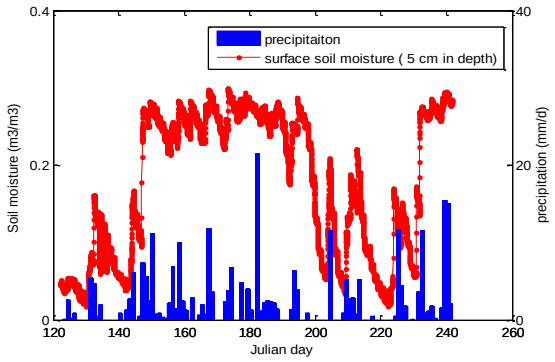


Figure 25. Seasonal changes in surface soil moisture measured at a depth of 5 cm and rainfall.

When using the inverted roughness heights (i.e. $z_{om}$ and $z_{oh}=0.1 \cdot z_{om}$ by approximation), the calibrated SEBS model showed the lower RMSE (H: 34 W/m$^2$, LE: 40 W/m$^2$) from the BREB measurements than the open-loop (H: 65 W/m$^2$, LE: 60 W/m$^2$). For the higher RMSEs in latent heat (40 and 60 W/m$^2$, respectively), there are various explanations. First, the Gaussian error propagation analysis showed that the errors in latent heat are additive and interfered by several other input parameter errors. In addition, the small errors in sensible heat can be largely propagated to latent heat through the SEBS model, as shown in (4-13), (4-16) and (4-17). More specifically, if the thermal or aerodynamic roughness height is overestimated as shown in Figure 4, sensible heat H becomes overestimated by (4-12), aerodynamic resistance $r_a$ becomes underestimated by (4-15) or wet sensible heat ($H_{wet}$) becomes underestimated by (4-14). Once the sensible heat is overestimated, the relative evaporation ($\Lambda r$) becomes underestimated by (4-13), and evaporative fraction ($\Lambda$) underestimated by (4-16), and finally latent heat underestimated by (4-18). This underestimated latent heat and overestimated sensible heat by roughness errors was demonstrated in the original SEBS of Figure 24.

It was also investigated whether the calibrated SEBS model can better addresses the

energy partitioning influenced by the vegetation development and increase in soil moisture during Monsoon (van der Tol et al., 2009). It is previously known that the dominant energy in the Tibetan Plateau is sensible heat (Ma et al., 2009). However, the calibrated SEBS model showed that the latent heat was approximately comparable to the sensible heat during Monsoon, suggesting that there is a significant seasonal change in the energy partitioning. The Monsoon precipitation was considered as one of the reasons for such a seasonal change. Prior to the Monsoon period, high sensible heat (above 150 $Wm^{-2}$) was considered to significantly develop the convective activities in the Atmospheric Boundary Layer (ABL), which usually initiate the Monsoon precipitation as a feedback (Ma et al., 2009; Wen et al., 2010). As a consequence, this Monsoon precipitation further elevated the surface soil moisture approximately up to 0.3 $m^3/m^3$, as shown in Figure 25, indirectly increasing the latent heat but slightly suppressing the sensible heat.

#### 3.3.2.4. Conclusion & Summary

In heat flux estimation, aerodynamic roughness is a major uncertain input. Unlike other parameters such as pressure, land surface temperature or surface soil moisture, this parameter can be indirectly estimated using eddy covariance data, which covers only limited fetch size on a local scale. However, due to measurement errors and land surface-atmospheric conditions not satisfying MOS assumptions, data inclined to be scattered with high standard variations. In a larger scale, a method using remotely sensed vegetation index can be employed. However, this still requires drag force input obtained from eddy covariance data, and also can be applied to limited vegetation type, on account of saturation problem of remote sensing. Non-linear MOS equations are also used to estimate aerodynamic roughness by iteration. However, this is a complicated procedure requiring the accuracy of several other related parameters involved in MOS theory.

Thus, this study demonstrated a simpler operational framework to retrieve a parameter of aerodynamic roughness via EnKF that affords non-linearity. This method demands only single or two heat flux parameters, which were elected by model error structure analysis. This study successfully adjusted the heat flux outputs over or underestimated by original SEBS, allowing more reliable interpretation for energy partitioning and water cycle. Analysis suggested lower sensible heat and higher latent heat during the summer Monsoon than original SEBS. At the onset of Monsoon, this discrepancy was remarkable in accumulative heat flux. Main energy source in Naqu site was still sensible heat even during Monsoon period, and latent heat was minor before/after Monsoon precipitation. Aerodynamic roughness estimated in this study was time-variant, reflecting vegetation effects, and independent from remotely sensed VI saturation problem. It was demonstrated that this

approach can be applied to the local field where eddy covariance data are not available. This may replace existing wind profile or vegetation index approach as an alternative. Future work will include some scale issues: the application of this approach to a larger scale with heterogeneity. The forest area where it is difficult to identify the vertical characteristics with remotely sensed VIs is also an interest. Effect of observation update with low temporal frequencies such as satellite data should be explored in future data assimilation scheme.

### 3.4. Case study II: Landriano station in Italy

To demonstrate that the inverse method can be differently applied in different climatic conditions, another experiment was carried out with the EC data over maize field at Landriano station, in Italy during vegetation development period in the beginning of July to the middle of October. In this site, the atmospheric condition is mostly unstable, and soil moisture is moderately high (0.25~0.35 $m^3/m^3$), suggesting a different instrument error condition (Baroni et al., 2010). Accordingly, unlike the BREB method in arid conditions as in the Tibetan Plateau suggesting a high degree of latent heat errors, both latent and sensible heat fluxes - e.g. the error of 15~20% equally for both heat fluxes, according to Chavez et al. (2005) - were used for inverting aerodynamic roughness under wet condition. Hence, both heat flux measurements were assimilated through the sequential EnKF to the SEBS model. As described in 3.3.1., the aerodynamic roughness was inverted from heat flux. The result indicated that the inverted aerodynamic roughness showed 0.25m as a mean and 0.04m as standard deviation. This is the intermediate value between the VI approach and a traditional wind profile method. More specifically, the aerodynamic roughness formulated as a function of LAI and drag force showed a mean of 0.32 m, which is higher than the inverse method (Olioso et al., 2002). The traditional wind profile method considering the atmospheric stability correction on both neutral and non-neutral condition reported a mean of 0.18m, which is lower than the inverse method (Ma et al., 2008).

CHAPTER 4

# Parameter Estimation II: Soil Hydraulic Properties from Satellite Soil Moisture

A scarcity of spatially distributed soil hydraulic property information is the major source of uncertainty in SVAT scheme, especially on dry and sandy conditions. They are usually parameterized by the PTFs expressed as a function of clay or sand fraction. This soil information is obtained from the Food and Agriculture Organization (FAO) soil maps or ECOCLIMAP, due to its global availability (Champeaux et al., 2005). However, it was previously suggested that the relationship between soil texture and soil hydraulic properties is uncertain, empirical and site-specific (Soet and Stricker, 2003; Gutmann and Small, 2007; Pellarin et al., 2009; Brimelow et al., 2010). Hence, there is a limitation in applying the same PTF to various bio-climatic conditions on the meso scale. To overcome the limitation of PTFs, another global map relevant to soil hydraulic parameters (e.g. wilting point, porosity or saturated hydraulic conductivity), the International Satellite Land Surface Climatology Project (ISLSCP) II was suggested, based upon the FAO soil maps and Neural Network Analysis (Schaap et al., 1998). However, its applicability may also be limited, when it is utilized for soil composition and bio-climatic conditions different from their bootstrap soil sample data base. Therefore, it would have much wider applicability to directly extract the spatially distributed soil and hydraulic property from globally available satellite data rather than the use of empirically defined PTFs or locally sampled soil data base.

*This chapter is based upon Lee et al. (2014)

As a strategy to systematically calibrate the soil hydraulic property information on the meso-scale beyond the empirical formulations at a local scale, an inverse method was previously suggested in various hydrological systems. The term of 'inverse' is defined as the estimation of input values from the model states, on the contrary to the forward method determining the model states from input values. More specifically, it optimizes the objective function by minimizing a mismatch between the observations and the model simulations (Wigneron et al., 1993; Zhou, 2011; Li et al., 2012). Gutmann and Small (2007) applied an inverse method to determining the soil hydraulic input parameters of a NOAH land surface model, noting that a linear relationship between soil texture and soil hydraulic parameters is obscure (Brimelow et al.,2010). They selected the specific soil hydraulic parameters that showed a best fit to field measured latent heat. Their result was also compared with the existing soil texture approach, concluding that an inverse method is better in the estimation of latent heat. For future works, they suggested applying this inverse method into soil moisture satellite data beyond a local point scale. Kunstmann (2008) and Intsiful & Kunstmann (2008) also applied a stochastic inverse method to determining the SVAT land surface parameters including roughness length, wilting point soil moisture and field capacity. They stochastically generated several input parameters, and selected certain input parameters when satisfying given constraints or minimizing the objective functions (Goegebeur et al., 2007). On the other hand, some previous studies employed ensemble filterings for a purpose of calibrating soil hydraulic parameters (Li and Ren, 2011, Montzka et al., 2011). Hendricks-Franssen & Kinzelbach (2009) and Vrugt et al. (2005) regarded EnKF as the inverse calibration requiring less computational cost than other Monte-Carlo methods. This previous study applied EnKF to transient flow and transport model parameter calibration. Parameters and states were both updated by the observations or jointly analysed (Li et al., 2012). Sabater et al. (2008) also proposed a joint update of parameter and state through data assimilation, demonstrating that it can capture time-variant vegetation biomass and hydraulic properties. However, some studies encountered limitations associated with long parameter adaptation time due to a premature reduction in ensemble variance, divergence of parameters estimated or linear update scheme in joint state-parameter estimation through EnKF (Moradkhani et al. 2005; Qin et al., 2009; Kurtz et al., 2012). Without achieving adequate parameter error characterization based upon parameter measurements, it is uncertain to appropriately estimate a non-linear relationship with the cross-error covariance between parameter ensemble and state ensemble. Recently, Pauwels et al. (2009) and Santanello et al. (2007) retrieved soil hydraulic parameters of land surface models from multi-temporal active or passive microwave retrieved surface soil moisture. Pollacco and Mohanty (2012) inverted SVAT hydraulic parameters from satellite-retrieved soil moisture and evapotranspiration, and compared them with up-scaled point measurements, suggesting that the non-uniqueness of inverted hydraulic parameters needs to be reduced.

### 4.1. TDR measurement

Soil moisture can be measured by TDR installed in local stations (Cappelaere et al., 2009, Séguis et al., 2011, van der Velde et al., 2012).

### 4.2. SVAT land surface model

The SVAT scheme simulates the evolution of surface $\theta_g$ [$m^3/m^3$] and total root zone soil moisture $\theta_{rz}$ [$m^3/m^3$] over time t by following water balance (Noilhan and Platon, 1989; Noilhan and Mahfouf, 1996; Montaldo et al., 2001).

$$\frac{\partial \theta_g}{\partial t} = \frac{C_1}{d_1}\left(P_g - E_s\right) - \frac{C_2}{\tau}\left(\theta_g - \theta_{geq}\right) \qquad 0 < \theta_g < \theta_{sat} \qquad (5\text{-}1)$$

The first term in equation (5-1) describes the surface atmospheric exchange consisting of the precipitation $P_g$ that infiltrates into surface as well as root zone layers and surface bare soil evaporation $E_s$ from the surface layer $d_1$. $C_1$ is dimensionless surface soil variable. The second term addresses water diffusivity on the surface layer. $C_2$ is dimensionless transfer rate. $\theta_{geq}$ is equilibrium surface volumetric soil moisture. $\tau$ is a time constant equal to one day. $\theta_{sat}$ is saturated soil moisture.

$$\frac{\partial \theta_{rz}}{\partial t} = \frac{1}{d_2}\left(P_g - E_s - E_c - Q\right) \qquad 0 < \theta_{rz} < \theta_{sat} \qquad (5\text{-}2)$$

Equation (5-2) calculates total depth mean root zone soil moisture by the water budget consisting of $P_g$, total evapotranspiration (a combination of $E_s$ and $E_c$ canopy transpiration from the root zone layers $d_2$) and drainage Q. Q flows across the bottom of the root zone soil layers as follows: $K_s(\theta_{rz}/\theta_{sat})^{2b+3}$, where $K_s$ is saturated hydraulic conductivity, and b is a pore size distribution index parameter (Clapp and Hornberger, 1978). For the determination of resistance (i.e. atmospheric resistance between soil and reference height, stomatal resistance, soil resistance, canopy boundary layer resistance) required for a calculation of evapotranspiration, we followed Cammalleri et al. (2010), Jarvis (1976), Lee et al. (2012a), and Norman et al. (1995).

$$\theta_{geq} = \theta_{rz} - a\theta_{sat}\left(\frac{\theta_{rz}}{\theta_{sat}}\right)^{p}\left[1-\left(\frac{\theta_{rz}}{\theta_{sat}}\right)^{8p}\right] \quad (5\text{-}3)$$

$$C_1 = C_{1sat}\left(\frac{\theta_{sat}}{\theta_g}\right)^{\frac{b}{2}+1} \quad (5\text{-}4)$$

$$C_2 = C_{2ref}\left(\frac{\theta_{rz}}{\theta_{sat}-\theta_{rz}+\theta_l}\right) \quad (5\text{-}5)$$

Soil hydraulic variables $\theta_{geq,}$ $C_1$, and $C_2$ required as inputs in equation (5-1) are formulated as functions of soil moisture and soil texture, and illustrated in equation (5-3), (5-4) and (5-5), respectively. $\theta_l$ in (5-5) is a small numerical value of the constraint used when $\theta_{rz}$ approaches $\theta_{sat}$. When surface soil moisture is less than wilting point, a Gaussian distribution formulation is used for $C_1$, according to Braud et al. (1993) and Giordani et al. (1996).

$$C_1=C_{1max}\exp[-\frac{(\theta_g-\theta_{max})^2}{2\sigma^2}] \quad (5\text{-}6)$$

where, $C_{1max}$, $\theta_{max}$, and $\sigma$ are the maximum, the mode, and the standard deviation of the Gaussian function, respectively. They are parameterized as functions of wilting point $\theta_{wp}$ and land surface temperature expressed in Kelvin (Calvet and Noilhan,2000). Three soil hydraulic variables $C_{1,}$ $C_{2,}$ and $\theta_{geq}$ formulated as (5-3) to (5-6) require several input coefficients such as $\theta_{sat}$, $\theta_{wp}$, $C_{1sat}$ ($C_1$ at saturation), $C_{2ref}$ ($C_2$ for $\theta_{rz}$ = 0.5· $\theta_{sat}$), two coefficients for $\theta_{geq}$ formulation a and p, and a slope of retention curve b. They are all parameterized as a function of clay (or sand) fraction (%), according to the land surface parameterization scheme used in ISBA models (hereafter referred to as "soil maps-based PTFs") (Clapp and Hornberger, 1978; Noilhan and Lacarrère, 1995; Noilhan and Mahfouf, 1996).

Similarly to 2.3.1., for various input data required in the SVAT scheme, several global data were employed. Tropical Rainfall Measuring Mission (TRMM) 3B42 was used for rainfall data. European Centre for Medium-Range Weather Forecasts (ECMWF) was used for the meteorological inputs such as wind velocity, air and soil temperature, land surface temperature, inward and outward long and shortwave radiations, and relative humidity. The ECOCLIMAP datasets were used for LAI, thermal and aerodynamic roughness height, and soil information (i.e. clay and sand fractions from FAO soil maps) (Champeaux et al., 2005).

### 4.3. Case study I: SAR and Tibet-GAME datasets on the local scale

This Section primarily focused on the BJ station described in 1.1.1. and 2.2.1.. In contrast to several previous hydrological studies that applied an EnKF into the determinations of state variables such as surface soil moisture or land surface temperature, this study attempted to adopt EnKF to a less applied topic of parameter estimation (Margulis et al., 2002; Reichle et al., 2002, Reichle, 2008; Li et al., 2010). EnKF was used to reduce any potential SAR retrieval errors that may be adversely propagated into parameter estimation and to adjust any systematic difference between SAR estimation and SVAT land surface model simulation. The objective of this study is to provide a spatial scale operational framework for inverting soil hydraulic variables from EnKF-analyzed SAR surface soil moisture, and to improve the SVAT model. Compared to other previous studies, this approach suggests operational merits in that it does not heavily rely on the empirically defined PTFs, and it is capable of estimating the root zone soil moisture even when it is in a non-linear relationship with the surface soil moisture.

*Experimental set-up for EnKF*

The SVAT model described in 4.2. was used for model state. For the input data required for SVAT scheme, the meteorological data was directly obtained from the BJ station (van der Velde, 2009; Su et al., 2011). The meteorological data was considered uniform within a study domain, while other land surface estimates required for the calculation of resistance or stability correction (e.g., aerodynamic roughness height, canopy height, displacement and thermodynamic roughness heights) were considered to be spatially heterogeneous, and calibrated as a function of the MODIS leaf area index (LAI) (Lee et al., 2012b). The SVAT model was run for 120 days, approximately at a local point scale, while it was run for 20 days at a SAR spatial scale. The top soil layer $d_1$ was 0.05 m, while the root zone depth $d_2$ was 0.2 m, according to February & Higgins (2010). The SVAT input parameters are illustrated in Table 8.

Table 8. Parameter values used in SVAT model (point scale)

(soil type: loamy sand (Su et al., 2011), corresponding clay fraction: 6% (Cosby et al., 1984))

| Parameters | Default | Calibrated value |
|---|---|---|
| $K_s$ | 1.2 m/d<br>(van der Velde, 2010) | $156\times10^{-6}$ m/s<br>(Braud et al., 1993) |
| $C_{1sat}$ | 0.098<br>(Noilhan & Planton, 1989) | Not used |
| $\theta_{sat}$ | 0.421 $m^3/m^3$<br>(Noilhan & Mahfouf, 1996) | same as default |

| | | |
|---|---|---|
| a | 0.4<br>(Noilhan & Planton, 1989) | Not used |
| p | 4<br>(Noilhan & Planton, 1989) | Not used |
| b | 4.38<br>(Noilhan & Planton, 1989) | 1.2<br>Not used for $C_1$ |
| $C_{2ref}$ | 3.7<br>(Noilhan & Planton, 1989) | 5 |
| $\theta_{wp}$ | 0.091 $m^3/m^3$<br>(Noilhan & Mahfouf, 1996) | same as default |
| $\theta_{fc}$ | 0.1666 $m^3/m^3$<br>(Noilhan & Mahfouf, 1996) | same as default |

* Source is provided in brackets.

For the generation of SVAT model ensembles (surface soil moisture), soil variable $C_1$ was randomly generated, ranging from 0 to 0.2, while equilibrium soil moisture $\theta_{geq}$ was randomly generated, ranging from 0 to 0.3 (Noilhan and Planton, 1989; Mahfouf and Noilhan, 1991). It was not assumed to be a Gaussian distribution due to its high uncertainty (Margulis et al., 2012; Evensen, 2003). $\theta_{geq}$ were perturbed, because (5-5) is not applicable to vertically heterogeneous conditions like Naqu site (Montaldo et al., 2001). $C_1$ was also perturbed, because $\theta_{wp}$ used in (5-3) has uncertainty in dry soils (Brimelow et al., 2010). These input ensemble pools were propagated through the SVAT model to establish surface soil moisture ensemble pools. The ensemble size was 100 (Margulis *et al*., 2002). For true field, SAR-retrieved surface soil moisture was used, as described in 2.2.2.3 (van der Velde, 2010; van der Velde *et al*., 2012). Here, true field is defined as the observations before the observation errors are taken into account (Evensen, 2003). The observation variance perturbed for observation errors was set to 0.01. This *a priori* value was based upon SAR retrieval errors (i.e. RMSE between the SAR data in a single pixel and field measurements), and EnKF final analysis under the given experimental conditions. No data assimilation was carried out for *in-situ* field measurements. No localization and inflation was applied.

#### 4.3.1. Inverse method

The objective function minimizing a difference between simulated and observed surface soil moisture was optimized simultaneously with some constraints shown below. In specific, the soil variable $C_1$ and $\theta_{geq}$ satisfying the following objective function in (6-1) and constraints in (6-2) to (6-5) were selected directly from the ensemble pools established above in the EnKF set-up. This calibration scheme does not use (5-2), (5-3), and (5-5). Accordingly, several input parameters such as $C_{1sat}$ and b in (5-2), wilting point in (5-3) and *a* and *p* parameters in (5-5) are not used. Instead, this method directly inverts the soil variable $C_1$ and

$\theta_{geq}$ from soil moisture, beause they are a function of soil moisture. The objective function is formulated as follows:

$$\text{Min } |\theta_{g,ref} - \theta_{g,sim}(C_1, \theta_{geq})| \quad (6\text{-}1)$$

$$\text{Subject to} \begin{cases} 0.8\theta_{g,ref} \le \theta_{geq} \le \theta_{g,ref} & \text{if no rain} \quad (6\text{-}2) \\ \theta_{g,ref} \le \theta_{geq} \le 1.2\,\theta_{g,ref} & \text{if rain} \quad (6\text{-}3) \end{cases}$$

$$\text{Subject to} \begin{cases} 0 < C_1 < 0.05 & \text{for } \theta_g > \theta_{wp} \quad (6\text{-}4) \\ C_1 > 0.05 & \text{for } \theta_g < \theta_{wp} \quad (6\text{-}5) \end{cases}$$

In objective function (6-1), reference surface soil moisture $\theta_{g,ref}$ refers to reference data such as *in-situ* field measurements or EnKF-analyzed SAR surface soil moisture, while $\theta_{g,sim}$ is SVAT-simulated surface soil moisture as a function of soil hydraulic variables $C_1$ and $\theta_{geq}$. $\theta_{g,sim}$, $C_1$ and $\theta_{geq}$ were stochastic ensemble members with an ensemble size of 100, while $\theta_{g,ref}$ was deterministic single values. Here, *a priori* information on the range of $\theta_{geq}$ introduced in constraints (6-2) and (6-3) was based upon the hydrostatic effect of the restoring term $\theta_g - \theta_{geq}$ in equation (5-1). Under hydrostatic conditions, the difference between $\theta_{geq}$ and $\theta_g$ should be precisely 0, and there is no vertical flow, due to the vertical inhomogeneity of soil hydraulic properties (Montaldo et al., 2001). This hydrostatic hypothesis is applicable to the Naqu site that the wet surface condition with rainfall intensity higher than evaporative demand exhibits corresponding low root zone soil moisture, due to a lack of significant vertical flow. As shown in Figure 28, this hyposthesis was reinforced by the field measurements showing a minimal vertical flow between surface and root zone soil moisture at this site. While surface soil moisture significantly increased from 0.05 to 0.27 $m^3/m^3$ by rainfall, the root zone soil moisture was marginally elevated from 0.05 to 0.09 $m^3/m^3$. To express this minimal flow, the constraints (6-2) and (6-3) were suggested: $\theta_{geq}$ is close to but slightly greater than $\theta_g$ during the recharge to $\theta_g$, while $\theta_{geq}$ is close to but slightly less than $\theta_g$ during the drainage to $\theta_{rz}$ (Montaldo and Albertson, 2001, Montaldo et al., 2001).

For reference data $\theta_{g,ref}$ used in objective function (6-1), EnKF-analysis was employed to adjust any potential systematic or retrieval errors of SAR data and to reconcile any physical difference between SAR instrument and SVAT land surface model. For instance, the SAR surface soil moisture products often exhibit a large error during or after the rainfall, being influenced by several factors such as a change in penetration depth, topographic effect (e.g., puddle) or a change in vegetation optical depth with no geometric implication (Saleh et

al., 2006). Especially, the roughness in SAR retrieval algorithms is one of the main source errors. Although this study assumed the time-invariance of roughness over the backscattering data measured from three different incidence angles, in fact, roughness can vary by sudden rainfall (van der Velde, 2010, van der Velde et al., 2012). Even when there is no rainfall activity, the roughness for the same backscattering or the sensitivity to dielectric constant can vary by soil moisture, soil texture or severl other environmental conditions, resulting in some inversion error (Sano et al., 1999, Mattia et al., 2006). In addition, vegetation effect from the grassland in study site could cause some bias, resulting in backscattering measurement errors (Scipal, 2002, van der Velde et al., 2012). Most of all, the penetration depth of SAR instrument in dry and sandy soils can be much greater than the SVAT surface soil layer, resulting in a large discrepancy when comparing the SAR surface soil moisture with SVAT estimation (Guo, 2000). Furthermore, although SVAT scheme assumed no runoff, satellite data, in general, often reports runoff due to stauration effects or shallower penetration depth by rainfall or roughness error. Hence, any erroneous estimation of surface soil moisture by SAR systematic errors or any difference between SAR instrument and SVAT land surface model physics could be adversely propagated into the parameter estimation, so EnKF has been suggested to adjust these aspects (Reichle et al., 2002, Moradkhani, 2008, Reichle, 2008).

Due to a low temporal resolution of SAR data, if there is no data available on any SVAT model time step (e.g. DoY 217), then time-interpolation of soil hydraulic variables was carried out, and SVAT simulation was run on each SAR pixel, and every day from DoY 216 till DoY 224. Relatively short simulation time for calibration schemes could be justified by appropriate initialization schemes that used SAR surface soil moisture as initial conditions and calibrated parameters.

#### 4.3.2. Discussions & Results

##### 4.3.2.1. Estimation of soil hydraulic variables $C_1$ and $\theta_{geq}$ on a local point scale

The soil hydraulic variables estimated in this study were first assessed with a local point station data to compare them with the original SVAT PTFs. As shown in a trend line of Figure 26-a, calibrated soil variable $C_1$ was inversely proportional to surface soil moisture, since hydraulic diffusivity decreases in dry soils. This inverse pattern was consistent with Noilhan and Planton (1989) and Mahfouf and Noilhan (1991), while its range was agreeable to Braud et al. (1993) that considered the maximum $C_1$ as 0.45. In contrast, before calibration, $C_1$ was not appropriately estimated, as indicated by "$C_1$ before calibration" in Figure 26-a. Uncalibrated $C_1$ reported 65% of several invalid numbers (<0.01) on dry conditions below

the wilting point, as shown in Figure 26-b.

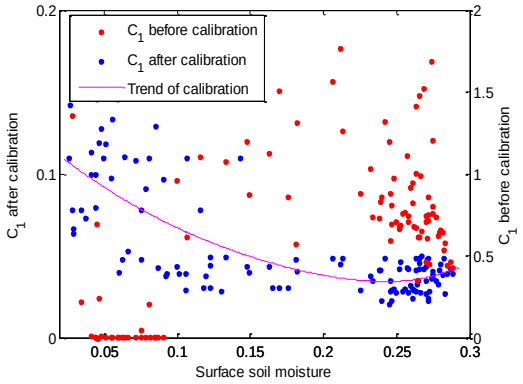


(a)

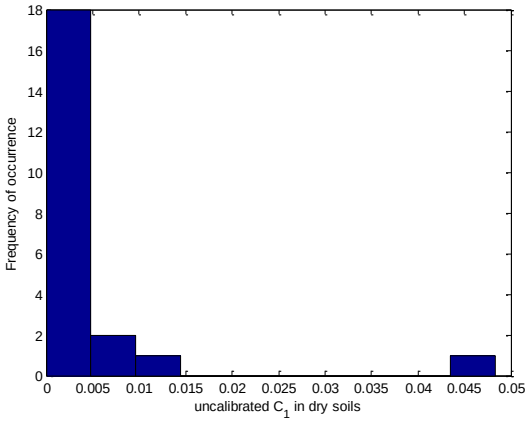


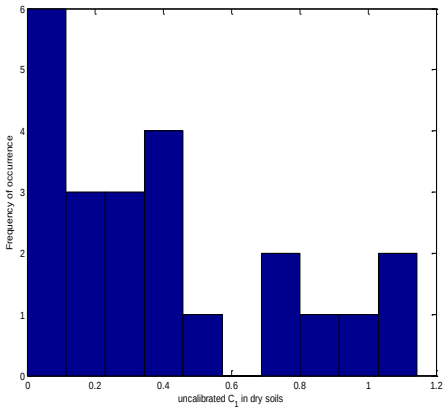


(b) (c)

Figure 26. (a) Relationship between surface soil moisture and $C_1$ at BJ station; (b) Frequency of $C_1$ ($\theta_{wp}$: 0.09); (c) Frequency of $C_1$ ($\theta_{wp}$: 0.15)

This is mainly because equation (5-3) used on dry conditions (Braud et al., 1993; Giordani et al., 1996; Noilhan and Mahfouf, 1996) largely relies on wilting point information. Wilting point is considered very significant but often exhibits faulty estimation especially on dry conditions with original SVAT PTFs formulated solely as a function of clay fraction (Pellarin et al., 2009, Brimelow et al., 2010). Accordingly, its uncertainty could be propagated to $C_1$ estimation by (5-3). For example, as shown in Figure 2-c, when changing only wilting point $\theta_{wp}$ in (5-3), $C_1$ was estimated within a valid range suggested by Braud et al. (1993). Additionally, both formulas (i.e., (5-2) as well as (5-3)) assumed soil hydraulic properties to be vertically homogenous. However, this assumption is not applicable to the Naqu site with underlying impermeable permafrost and on highly stratified conditions (Guo, 2011). Finally,

diverse soil condition is also uncertainty. More specifically, Braud et al. (1993) examined this formula only up to land surface temperatures of 10℃ at the lowest, while the study site often reaches temperatures below this level. They also underlined that (5-3) was validated with the Barrax soil and clay only, suggesting uncertainty in other soil textures such as sand.

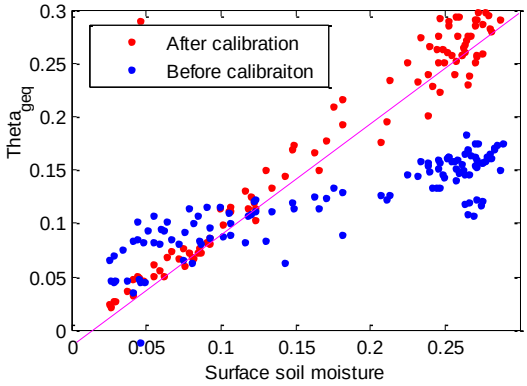


Figure 27. Relationship of $\theta_{geq}$ with surface soil moisture

Next, calibrated $\theta_{geq}$ was also compared with the original SVAT PTFs, as shown in Figure 27. The $\theta_{geq}$ calibrated in this study was higher than the original schemes. The underestimation of $\theta_{geq}$ by the original SVAT PTFs was mainly attributed to (5-5) assuming a vertical homogeneity. However, at Naqu site, under hydrostatic conditions, root zone soil moisture did not respond to surface exchange, due to the vertical inhomogeneity of the soil hydraulic properties (Montaldo et al., 2001, Montaldo and Albertson, 2001). The statistical comparisons before and after calibration of $C_1$ and $\theta_{geq}$ were illustrated in Table 9 (time average over Figure 26-a and Figure 27).

Table 9. Time average comparison of soil hydraulic variable and soil moisture at BJ station

| Variable [unit] | | Before calibration | After calibration |
|---|---|---|---|
| $C_1$ [ - ] | mean | 1.2420 | 0.0670 |
| | std. | 1.7541 | 0.0486 |
| | max. | 12.5815 | 0.1967 |
| | min. | 0 | 0 |
| $\theta_{geq}$ [$m^3/m^3$] | mean | 0.1697 | 0.1798 |
| | std. | 0.0507 | 0.0957 |
| | max. | 0.2518 | 0.3102 |
| | min. | 0 | 0 |
| RMSE of $\theta_g$ [$m^3/m^3$] | | 0.0494 | 0.0148 |
| RMSE of $\theta_{rz}$ [$m^3/m^3$] | | 0.1185 | 0.0164 |
| Correlation between $\theta_g$ and $\theta_{rz}$ | | 0.9360 | 0.6017 |

4.3.2.2. Validation of calibrated soil hydraulic variables on a local point scale

The soil hydraulic variables compared above were further used to determine the soil moisture profile. Before calibration, in Figure 38, uncalibrated $C_1$ and $\theta_{geq}$ led to the underestimation of $\theta_g$, while uncalibrated Ks, and b overestimated $\theta_{rz.}$ This demonstrated the error propagation of soil hydraulic variables misestimated by the original SVAT PTFs into soil moisture estimations. In contrast, the soil moisture profile estimated after calibration showed better matches with field measurements of both surface and root zone soil moisture, as shown in Table 9 (i.e. RMSE of $\theta_g$ decreased from 0.0494 $m^3/m^3$ to 0.0148, while RMSE of $\theta_{rz}$ decreased from 0.1185 $m^3/m^3$ to 0.0164). It was also noted that a non-linear relationship between $\theta_g$ and $\theta_{rz}$ was properly demonstrated after calibration (in Table 9, correlation between $\theta_g$ and $\theta_{rz}$ dropped from 0.9360 to 0.6017). Here, 'non-linear' indicates that surface soil moisture vigorously increased responding to rainfall events (e.g. 0.0254 $m^3/m^3$ on DoY 222 to 0.2883 on DoY 240), while root zone soil moisture stays same with no large increments (e.g. 0.0460 $m^3/m^3$ on DoY 222 to 0.1079 on DoY 240). In short, the appropriate calibration of soil hydraulic variables is shown to be necessary for the successful derivation of soil moisture profile, and it was also shown that hydrostatic assumption is appropriate for this study site.

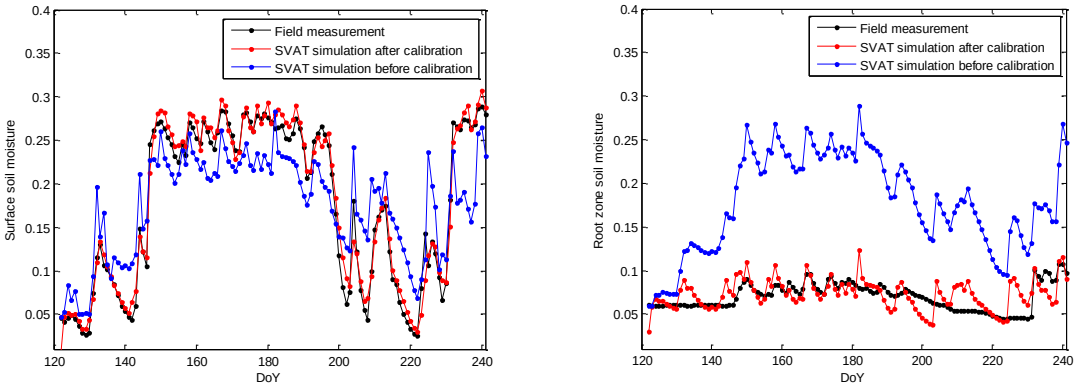


(a) (b)

Figure 4. Soil moisture profile before and after the calibration at BJ station: surface soil moisture and (b) root zone soil moisture, respectively. Unit: $m^3/m^3$.

4.3.2.3. EnKF-analyzed SAR surface soil moisture

After data assimilation, the errors in SAR estimation decreased, showing a better match

with the field measurements. In detail, the EnKF performance and the improvement of $\theta_g$ estimation were assessed on daily SVAT model simulation time step as shown in Table 10. The 2nd column showed the reduction in the RMSE between EnKF final analysis and true field (i.e., SAR data), suggesting a successful convergence towards the observations. Spread in the 3rd column calculated a spatial average of anomaly standard deviations, while correlation in the 4th column determined a relationship between ensemble mean and true field. High correlation implies that observation and model ensemble were not departed but likely to be converged. A point comparison between SAR data on a pixel nearest to a local point station and *in-situ* field measurements was also presented in the 5th column, as indicated by "$RMSE_{pixel}$ (before)". After data assimilation, as indicated by "$RMSE_{pixel}$(after)", RMSE between EnKF analysis in a pixel and field measurement significantly decreased, suggesting that SAR retrieval errors were mitigated. Higher RMSE estimated before data assimilation was considered due to vegetation effects from grasslands present in the site. On DoY 221, a large RMSE before EnKF was considered to be affected by the lowest incidence angle among other SAR data. Nair (2007) reported that the effect of incidence angles at VV polarization influences overestimation of backscattering. On DoY 224, higher RMSE estimated before EnKF was considered due to roughness. It was assumed to be time-invariant, yet it in fact could be changed by rain fallen on this day (Sano et al., 1999, van der Velde, 2010). These factors could therefore be adjusted in EnKF final analysis. Finally, a spatial average of EnKF final analysis was shown in the 7th column. For an example, the spatial comparison was also presented in Figure 29.

Table 10. Statistics of EnKF-analyzed SAR surface soil moisture, unit: $m^3m^{-3}$

| Model time step (DoY) | RMSE with true field | Spread | Correlation [ - ] | $RMSE_{pixel}$ (before) | $RMSE_{pixel}$ (after) | Spatial Average |
|---|---|---|---|---|---|---|
| 216 | 0.0818 | 0.0194 | 0.8676 | 0.0928 | 0.0302 | 0.0966 |
| 219 | 0.0503 | 0.0154 | 0.8485 | 0.0122 | 0.0177 | 0.0516 |
| 221 | 0.0636 | 0.0181 | 0.8872 | 0.0988 | 0.0382 | 0.0772 |
| 222 | 0.0518 | 0.0154 | 0.8400 | 0.0274 | 0.0006 | 0.0529 |
| 224 | 0.0810 | 0.0197 | 0.7392 | 0.1616 | 0.0148 | 0.1084 |

*RMSE with true field: RMSE between EnKF final analysis and true field; RMSEpixel(before): RMSE between field measurement and SAR surface soil moisture in a single SAR pixel nearest to a local BJ station; RMSEpixel(after): RMSE between field measurement and EnKF analyzed surface soil moisture in a single SAR pixel nearest to a local BJ station.

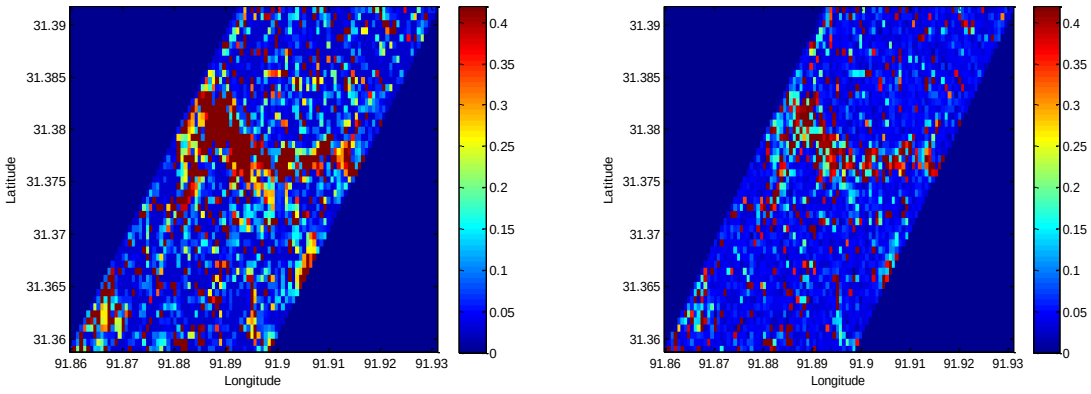


(a) (b)

Figure 29. Soil moisture (a) by SAR and (b) by EnKF analysis (DoY 224). unit: $m^3/m^3$.

4.3.2.4. Application of an inverse method to a SAR spatial scale

The calibration scheme validated at a local point scale was further applied to a SAR spatial scale. The SVAT scheme was run on each SAR pixel, according to the inverse method described in 4.3.1. The SAR-based inverse calibration schemes of this study were compared with soil maps-based PTFs in Figure 30 and 31. In Figure 30-b, before calibration, large $C_1$ values were estimated over dry area below wilting point, rejecting the Gaussian distribution (i.e. estimating small values in dry soils) suggested by Braud et al. (1993). In Figure 31-b, similarly to a local point scale, $\theta_{geq}$ was underestimated, consequently being similar to the root zone soil moisture levels and rejecting hydrostatic conditions. In contrast, a calibration scheme presented an inverse relationship of $C_1$ values with surface soil moisture, as being consistent with the inverse relationship previously shown in Noilhan and Planton (1989). $\theta_{geq}$ was also tuned to surface soil moisture levels, satisfying hydrostatic conditions.

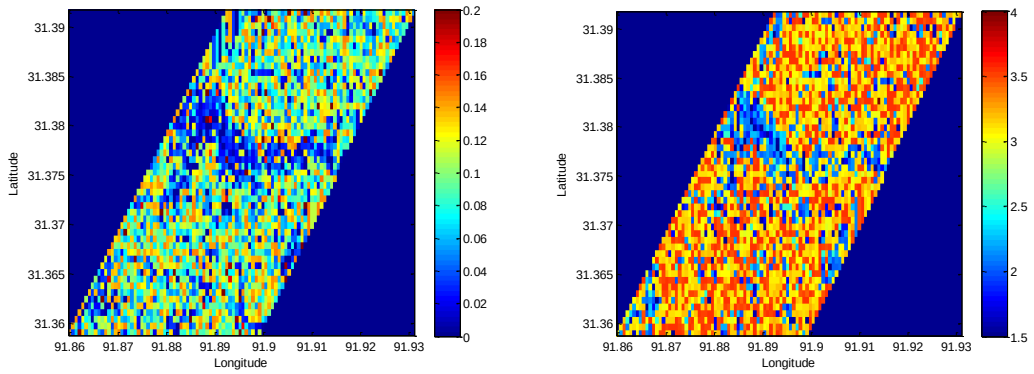

(a) (b)

Figure 30. $C_1$ (a) after calibration and (b) before calibration (DoY 224).

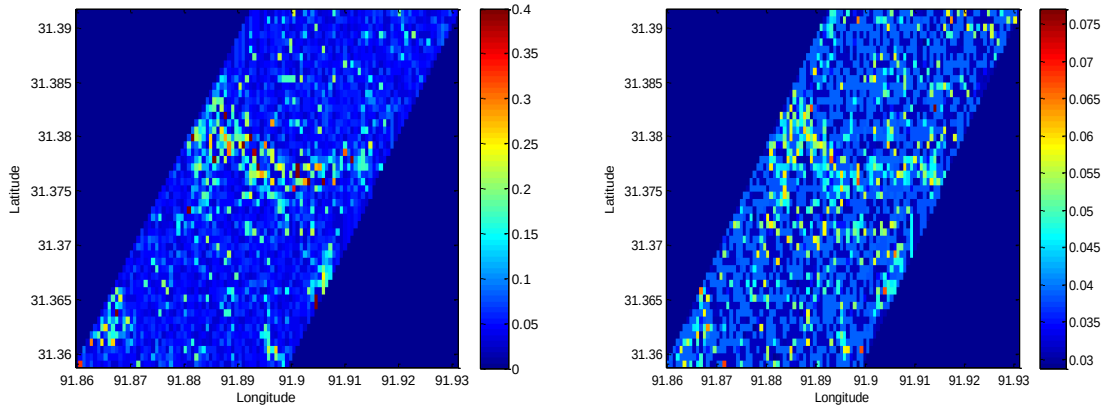


(a) (b)

Figure 31. $\theta_{geq}$ (a) after calibration and (b) before calibration (DoY 224).

Spatially distributed soil and hydraulic variables were further used to estimate the soil moisture profile, as presented in Figure 32 and 33. Before calibration, surface soil moisture was significantly underestimated. In terms of spatial distribution and soil moisture level, it was similar to root zone soil moisture levels, suggesting a higher correlation of 0.8480 in Table 11. In contrast, after calibration, surface soil moisture was much higher than root zone soil moisture, demonstrating a lower correlation of 0.3252, higher spatial variability (i.e. higher standard deviation of 0.0320 in Table 11) and better non-linear relationship with root zone soil moisture. As shown in Figure 32 and 33, this non-linear relationship was captured in the calibrated SVAT. More specifically, the root zone soil moisture was uniformly dry in terms of the spatial distribution, while surface soil moisture was largely elevated by the rain fallen on the same day and wet especially in a latitude of 31.38. Considering that all other experimental conditions were same except soil and hydraulic variables (e.g. $K_s$, b, $C_1$, and $\theta_{geq}$ in Table 8) before and after calibration, it was suggested that a key determinant of soil moisture distribution is soil hydraulic properties rather than soil texture or atmospheric forcing. This finding can be supported by Chang and Islam (2003) that previously suggested that soil property are the key determinants for a spatial variability of soil moisture. It was also suggested that root zone soil moisture may not be capable of being inferred from surface soil moisture in stratified soils. Finally, the point-scale comparisons between field measurements and SVAT soil moisture profile at a pixel nearest to a local point station were provided in Table 12, where surface soil moisture field measurement is a spatial average between BJ (depth: 4.5cm) and NQ stations (depth: 2.5 cm) installed right behind the BJ station .

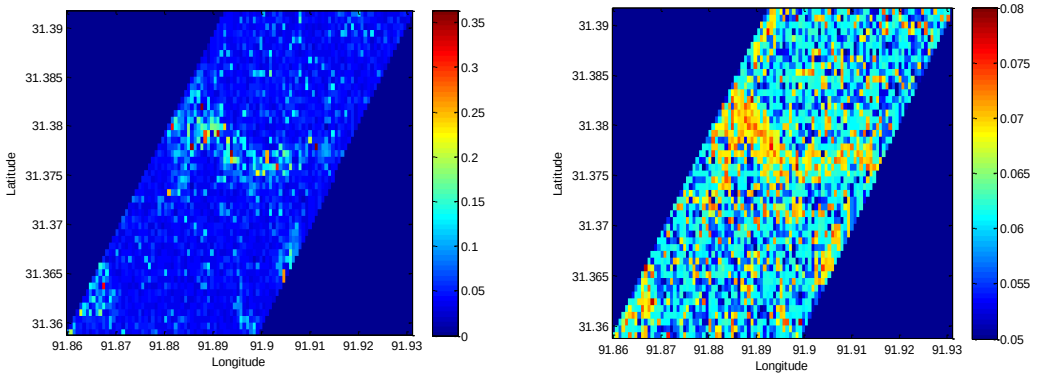


(a) (b)

Figure 32. $\theta_g$ (a) after calibration and (b) before calibration (open loop) (DoY 224), unit: $m^3/m^3$.

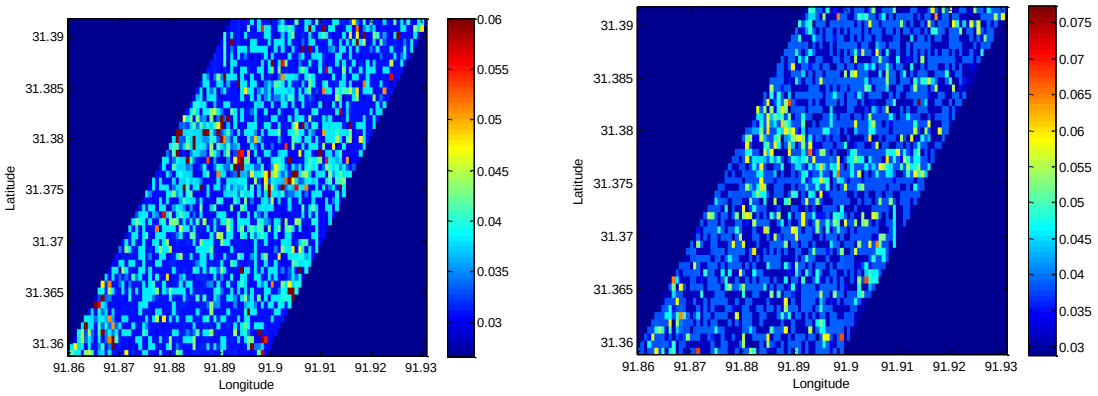


Figure 33. $\theta_{rz}$ (a) after calibration and (b) before calibration (open loop) (DoY 224), unit: $m^3/m^3$.

Table 11. Spatial average of soil variable and soil moisture at a SAR spatial scale (DoY 224)

| Variables [unit] | Before calibration | After calibration |
|---|---|---|
| $C_1$ [ - ] | 2.9794 (0.5847) | 0.0868 (0.0483) |
| $\theta_{geq}$ [$m^3/m^3$] | 0.0381(0.0070) | 0.0679 (0.0507) |
| $\theta_g$ [$m^3/m^3$] | 0.0613 (0.006) | 0.0552 (0.0320) |
| $\theta_{rz}$ [$m^3/m^3$] | 0.0381 (0.007) | 0.0353 (0.0062) |
| Correlation between $\theta_g$ and $\theta_{rz}$ | 0.8480 | 0.3252 |

* Standard deviation is provided in brackets.

Table 12. Point comparison between field measurement and SVAT simulation (DoY 224)

| | **Field measurement** | **$SVAT_{pixel}$ before calibration** | **$SVAT_{pixel}$ after calibration** |
|---|---|---|---|
| $\boldsymbol{\theta_g}$ | 0.0825 | 0.0620 | 0.0787 |
| $\boldsymbol{\theta_{rz}}$ | 0.0445 | 0.0386 | 0.0382 |

* $SVAT_{pixel}$: SVAT estimation in a single SAR pixel nearest to a local BJ station, unit: $m^3/m^3$

#### 4.3.2.5. Conclusion & Summary

Operational merit of this approach is that it is independent from SAR instrument or retrieval errors (e.g. SAR radiometric response to rain or retrieval errors by roughness uncertainty), while conferring a spatial variability. This aspect is advantage because SAR measurement error (e.g. radio frequency interference) is not readily solved even by data assimilation (Reichle, 2008). Next, with respect to SVAT scheme, this approach reduces the number of input parameters and accommodates vertical heterogeneous soil layers. When this algorithm is applied to a larger scale than current study, future study might take a spatial variability of other parameters such as Ks or b into account.

### 4.4. Case study II: SMOS and AMMA datasets on the synoptic scale

Objective of this study is to provide a meso-scale operational framework of inverting the SVAT soil hydraulic variables often erroneous in dry and sandy soils from the EnKF analysis of SMOS surface soil moisture and to ultimately improve SVAT models with inverted soil and hydraulic variables. Because this study is aimed for the meso-scale spatial analysis with satellite data, EnKF was employed to alleviate any discrepancy between land surface model and satellite data and to reduce satellite errors presumably propagated into parameter estimation. Advantage of this approach is that this inverse calibration does not heavily rely on the empirically defined PTFs (Brimelow et al., 2010, Gutmann and Small, 2007, Schaap et al., 1998). With respect to joint parameter-state estimation through EnKF, this approach is more flexible because this does not require precise parameter error characterization and can be applied when parameter is highly uncertain and measurement is not available. This Section primarily focused on the sub-Saharan desert area described in 2.3.1.

*Experimental set-up for EnKF*

For the forcasts, SVAT model was used, as described in 4.2. For various input data required for simulating the SVAT scheme, several global data were employed. Tropical Rainfall Measuring Mission (TRMM) 3B42 was used for rainfall data. European Centre for Medium-Range Weather Forecasts (ECMWF) was used for the meteorological inputs such as wind velocity, air and soil temperature, land surface temperature, inward and outward long and shortwave radiations, and relative humidity. The ECOCLIMAP datasets were used for LAI, thermal and aerodynamic roughness height, and soil information (i.e. clay and sand

fractions from FAO soil maps) (Champeaux et al., 2005). The top soil depth was 0.05 m, while the root zone soil depth was 1 m.

The sequential EnKF was used as described in 2.2.2.1. For the generation of SVAT model ensembles, soil hydraulic input variables and forcing data were perturbed in the SVAT scheme. Two soil hydraulic input variables $C_1$ and $\theta_{geq}$ were randomly generated in specified ranges from 0.01 to 1 and from 0.01 to 0.5, respectively. Due to uncertainty of these variables, they were not restricted to be Gaussian distributed (Evensen, 2003). TRMM-retrieved rainfall data was also disturbed, assuming a normal distribution and variance of 10% (Yuter et al., 2005). Surface soil moisture ensembles were propagated through SVAT model from these input ensembles. Inflation for adjusting the forecast error was not used. Ensemble size was 100. For true field (i.e. the observations before taking into account the observation error), 1 day ascending SMOS L3 surface soil moisture products (CATDS OP 245) directly achieved from CATDS (www.catds.fr/) were used (Wigneron et al., 2007 and 2011; Jacquette et al., 2010; Kerr et al., 2012 and 2013). All the EnKF experiments shown in Table 3 used the same observation variance of 0.01 $[m^3/m^3]^2$ to build up the observation errors. This variance was determined by assessing a mismatch between true fields and field measurements. Localization was not carried out. Data assimilation was not conducted for *in-situ* field measurements on a local scale.

4.4.1. Inverse method

The objective function was simultaneously optimized by minimizing a mismatch between simulated and observed surface soil moisture and by considering some constraints shown below. More specifically, from the EnKF ensemble pools established in Section 2.3.2.1, specific soil hydraulic variables $\theta_{geq}$ and $C_1$ satisfying the following objective function in (7-1) and several constraints in (7-2) to (7-4) were selected, instead of using (5-3), (5-4) and (5-6).

$$\text{Objective function: } \min |\theta_{g,ref} - \theta_{g,sim}(C_1, \theta_{geq})| \qquad (7\text{-}1)$$

$$\text{Subject to } \begin{cases} 0.6\,\theta_{rz} < \theta_{geq} < 0.9\,\theta_{rz} & (7\text{-}2) \\ 0 < C_1 \text{ and } \theta_{geq} < \theta_{wp} \quad \text{if} \quad \theta_g < \theta_{wp} & (7\text{-}3) \\ 0 < C_1 \text{ and } \theta_{geq} < \theta_{sat} \quad \text{if} \quad \theta_g > \theta_{wp} & (7\text{-}4) \end{cases}$$

In the objective function (7-1), the reference surface soil moisture $\theta_{g,ref}$ refers to the observations such as the EnKF analysis of SMOS surface soil moisture or field measurement, while $\theta_{g,sim}$ signifies SVAT-simulated surface soil moisture as functions of soil hydraulic variables $C_1$ and $\theta_{geq}$. $\theta_{g,sim}$, $C_1$ and $\theta_{geq}$ are stochastic ensemble pools of EnKF scheme described in Section 2.3.2.1, while $\theta_{g,ref}$ are conclusively determined values. The fundemental rationale of this objective function is that if surface soil moisture contents were correctly estimated with appropriate $\theta_{geq}$ values in the reasonable range, then they have also used correct $C_1$ values. Here, the reasonable range of $\theta_{geq}$ expressed in constraint (7-2) was site-specifically suggested as *a priori* information for highly sandy soils, and may not be applicable to other sites covered with loam or clay soils. According to the ECOCLIMAP datasets, on a spatial average, a sand fraction in this study area is higher than 50%, ranging from 30 % up to 95% (see Figure 34). With regard to highly sandy soils, it was previously suggested that $\theta_{geq}$ is supposed to be smaller than the root zone soil moisture levels, unlike loam or clay soils (refer to Figure 2 in Noilhan and Planton (1989)). However, since it was previously demonstrated that the soil maps-based PTFs is liable to overestimate $\theta_{geq}$ to be similar to the root zone soil moisture levels in highly sandy soils (e.g. a sand fraction of 77% in Niger site), a constraint (7-2) was provided, assuming the slow evolution of root zone soil moisture (refer to Figure 5 in Pellarin et al. (2009)). In addition, constraints (7-3) and (7-4) were provided simply to characterize a tipping point of hydraulic behavior with $\theta_{wp}$, as previously suggested by Braud et al. (1993), Giordani et al. (1996), and Noilhan & Mahfouf (1996). No other limitations or parameter bounds were artificially imposed to extract variables from ensemble pools.

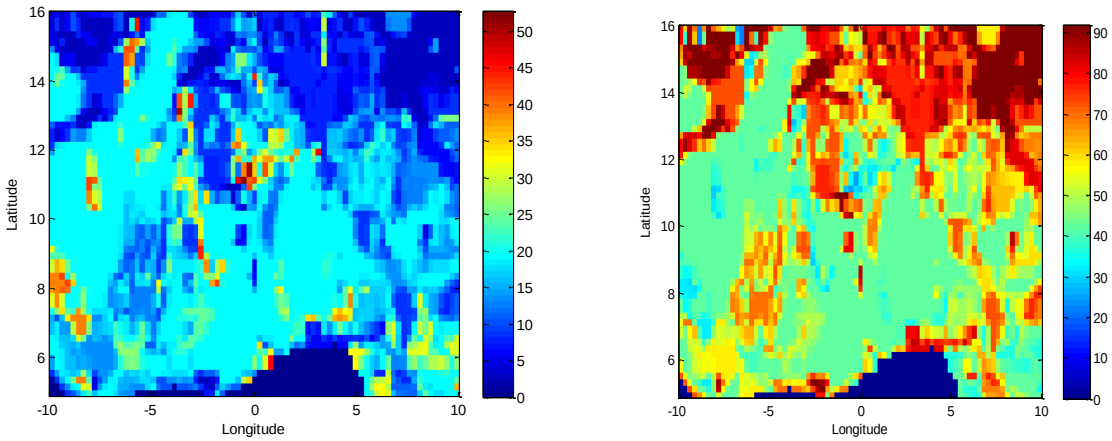


(a) (b)

Figure 34. ECOCLIMAP: (a) clay fraction, (b) sand fraction in a study domain, unit: %.

For reference data used in the objective function (7-1), the EnKF analysis of SMOS surface soil moisture was employed to reconcile the SMOS data with SVAT simulations and to resolve their estimation errors presumablly propagated into parameter estimation (Saleh et al., 2006; Holmes et al., 2008; Reichle et al., 2008; Scheel et al., 2011; Jackson et al.,2012; Schlenz et al., 2012). Systematically, there is some discrepancy between SMOS instrument and SVAT model. For instance, during and after rainfalls, SMOS surface soil moisture products often report run-off, being affected by several factors such as a change in penetration depth or a change in optical depth with no geometric implication, while the SVAT scheme assumes that run-off is negligible (Noilhan and Mahfouf, 1996). In addition, in dry and sandy soils, a penetration depth of SMOS instrument is often much deeper than wet conditions (e.g. only a few centimeters), while the surface soil layer always stays same in SVAT scheme (Escorihuela et al., 2007 and 2010; de Rosnay et al., 2008; Gruhier et al., 2008; Mironov et al., 2009 and 2013; Kerr et al., 2013). Lastly, another discrepancy between SMOS data and SVAT model is a data acquisition frequency. Since the entire study domain requires 3 day SMOS products in terms of a temporal coverage, 1 day SMOS products available for the EnKF analysis cover only a part of the entire study domain. When no EnKF final analysis of SMOS data was available on any given DoY and in any pixel location (e.g. on DoY 177 and 178, no 1 day SMOS product is available in the Niger and Benin site, as shown in Table 3) for calibration, undefined values were filled by a temporal interpolation.

#### 4.4.2. Discussions & Results

##### 4.4.2.1. Validation of inverted variables on a local scale

*Sensitivity of $C_1$ and $\theta_{geq}$ to soil moisture estimation*

To demonstrate whether we can improve the SVAT scheme with the calibration of selected variables, the sensitivity to $C_1$ and $\theta_{geq}$ was illustrated here. As shown in Figure 35 and Table 13, the surface soil moisture was very sensitive to variations in $C_1$ at both Benin and Niger sites, when $\theta_{geq}$ was constant at an optimal value to each site. Similarly, under the same $C_1$ condition, as shown in Figure 36 and Table 13, the surface soil moisture sensitively responded to changes in $\theta_{geq}$, suggesting that both soil hydraulic variables are largely responsible for the accurate estimation of surface soil moisture. On the contrary, these surface variables neither deteriorated nor significantly improved the estimation of root zone soil moisture, as shown in Figure 37. Since selected surface variables are involved with surface soil moisture in equation (5-1), a calibration can only improve the estimation of surface soil moisture. This aspect also justifies exploiting root zone soil moisture in a constraint (5-2).

Table 13. Time-average comparison between field measurement and SVAT simulation. unit: $m^3m^{-3}$

| ISBA scheme | Surface soil moisture in Niger | Root zone soil moisture in Niger | Surface soil moisture in Benin | Root zone soil moisture in Benin |
|---|---|---|---|---|
| $C_1 = 0.05$ | 0.0188 | 0.0450 | 0.0375 | 0.0167 |
| $C_1 = 0.3$ | 0.0335 | 0.0413 | 0.0469 | 0.0167 |
| $C_1 = 0.8$ | 0.0707 | 0.0392 | 0.0826 | 0.0168 |
| $\theta_{geq}=0.05$ | 0.0195 | 0.0326 | 0.0907 | 0.0153 |
| $\theta_{geq}=0.15$ | 0.0865 | 0.0236 | 0.0389 | 0.0167 |
| $\theta_{geq}=0.3$ | 0.2169 | 0.0230 | 0.1481 | 0.0171 |

*****Each SVAT scheme above used three different $C_1$ conditions but the same $\theta_{geq}$ value indicated in Figure 37, while it used three different $\theta_{geq}$ conditions but the same $C_1$ value indicated in Figure 36.

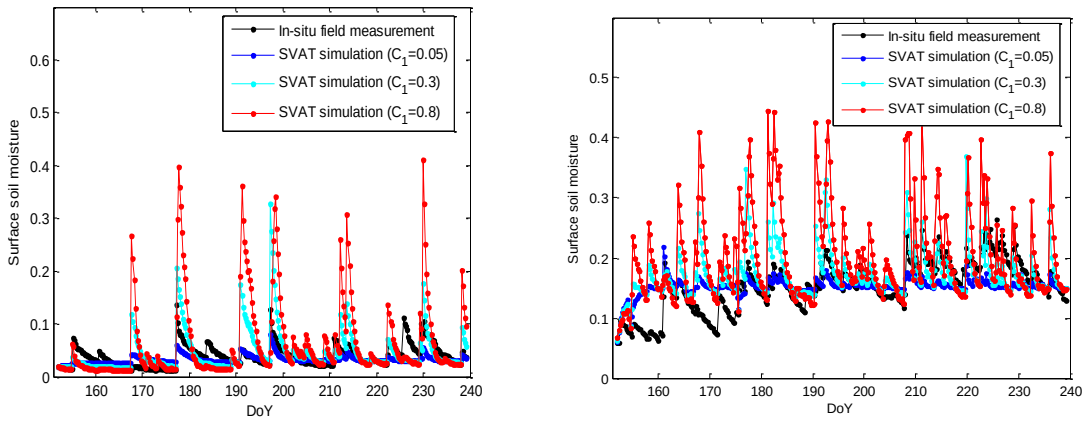


(a) (b)

Figure 35. Surface soil moisture sensitive to different $C_1$ input values:
(a) Niger site ($\theta_{geq}$ of 0.03); (b) Benin site ($\theta_{geq}$ of 0.15). Unit: $m^3m^{-3}$.

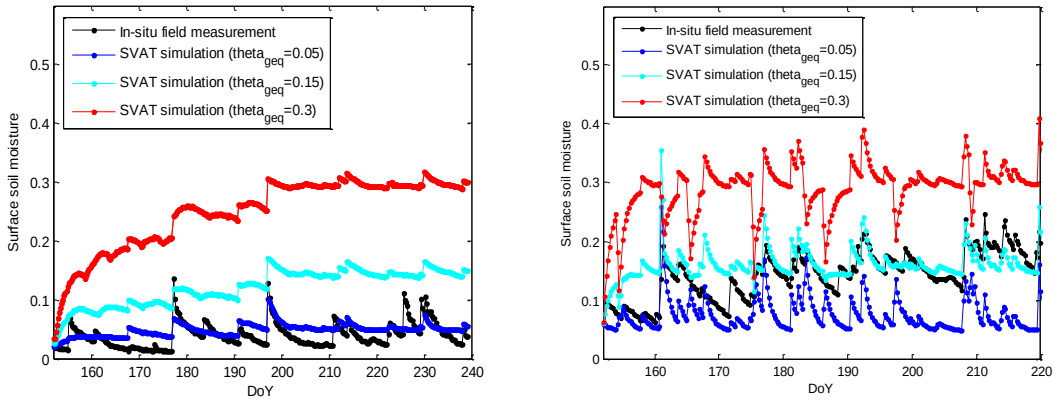


(a) (b)

Figure 36. Evolution of surface soil moisture sensitive to different $\theta_{geq}$:
(a) Niger site ($C_1$ of 0.05); (b) Benin site ($C_1$ of 0.15). unit: $m^3m^{-3}$.

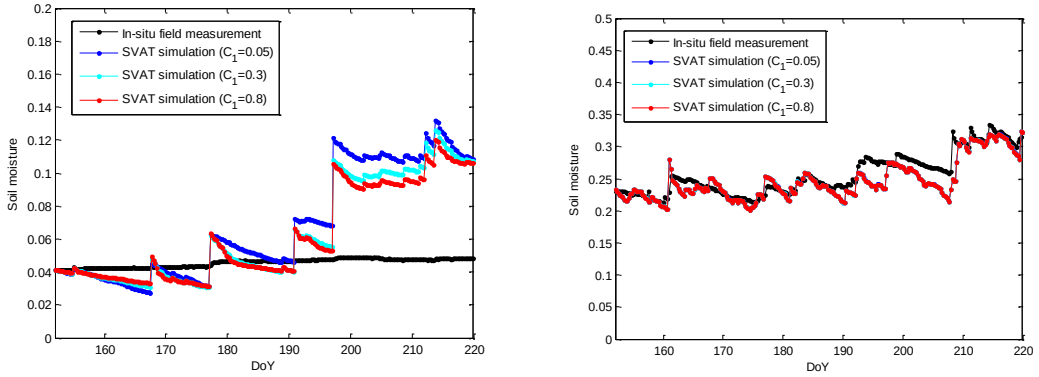


(a) (b)

Figure 37. Root zone soil moisture (depth:1 m) less sensitive to different $C_1$ input values: (a) Niger site ($\theta_{geq}$ of 0.03); (b) Benin site ($\theta_{geq}$ of 0.15). Unit: $m^3m^{-3}$.

*Comparison of inverted $C_1$ and $\theta_{geq}$ with soil maps-based PTFs approach*

The soil and hydraulic variables were estimated, according to the inverse calibration method described in 4.4.1., and were compared with the soil maps-based PTFs, in which (5-3) was used for $\theta_{geq}$, (5-4) and (5-6) were used for $C_1$, and other associated coefficients such as b, a, p, $\theta_{wp}$ and $C_{1sat}$ required as inputs of (5-3), (5-4), and (5-6) were calculated by soil maps-based PTFs of Noilhan & Mahfouf (1996).

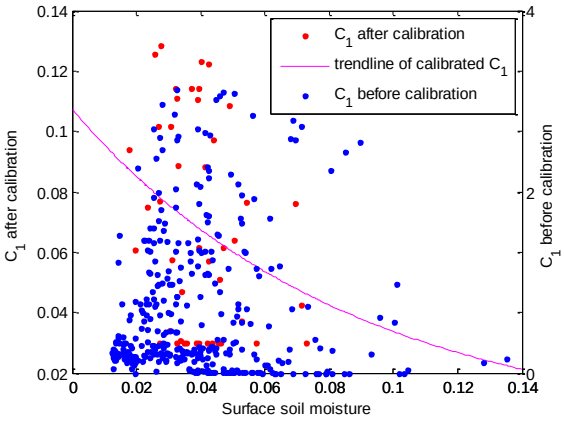


(a)

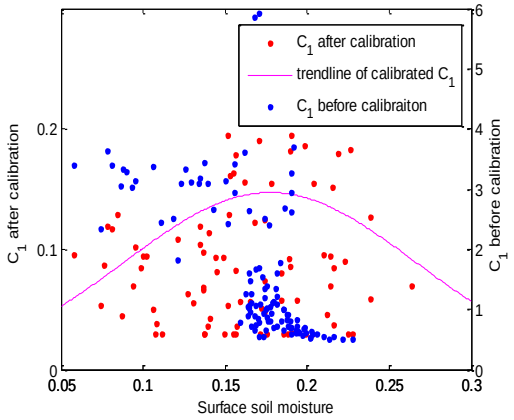


(b)

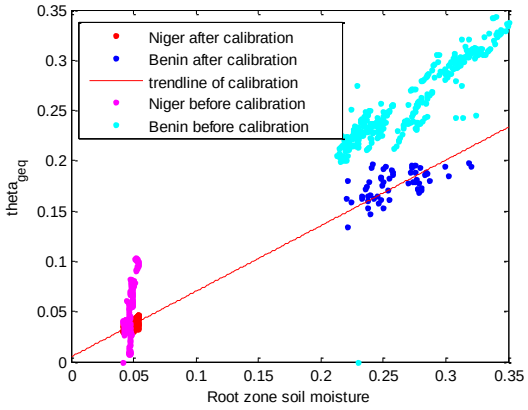


(c)

Figure 38. The relationships between parameters and soil moisture estimations (unit: $m^3m^{-3}$): (a) $C_1$ in Niger; (b) $C_1$ in Benin; (c) $\theta_{geq}$ in both sites

Before the inverse calibration, a distribution of $C_1$ estimated by soil maps-based PTFs was unevenly skewed, as shown in Figure 38-a and b. In both Niger and Benin sites, rather than the Gaussian distribution previously suggested by Braud et al. (1993) and Giordani et al. (1996), $C_1$ showed an inverse distribution that $C_1$ decreases as surface soil moisture increases. Furthermore, their mean and spread were much higher than the calibrated values, as shown in Table 14, consequently leading to overestimation in soil moisture estimation. In Niger, the mean of $C_1$ was much higher at 0.7598 before calibration and 0.0708 after calibration. The standard deviation of $C_1$ was higher at 0.9998 before calibration and 0.0385 after calibration. In Benin, the mean of $C_1$ was much higher at 0.71 before calibration and 0.0948 after calibration. The standard deviation of $C_1$ was higher at 1.3039 before calibration and 0.0651 after calibration. Additionally, with respect to the estimation of $\theta_{geq}$, as shown in Figure 38-c, before inverse calibration, $\theta_{geq}$ in sandy soils was just equal with the root zone soil moisture levels, failing to represent the effect of vertical gradient of hydraulic potential in sandy soils (Noilhan & Planton, 1989). In the Niger site, as shown in Table 14, the mean of $\theta_{geq}$ was higher at 0.052 $m^3/m^3$ before calibration and 0.0352 $m^3/m^3$ after calibration. The standard deviation of $\theta_{geq}$ was also higher at 0.0261 $m^3/m^3$ before calibration and much lower at 0.0046 $m^3/m^3$ after calibration. In the Benin site, the mean of $\theta_{geq}$ was higher at 0.2591 $m^3/m^3$ before calibration and lower at 0.1549 $m^3/m^3$ after calibration. The standard deviation of $\theta_{geq}$ was 0.0420 $m^3/m^3$ before calibration and similarly 0.0470 $m^3/m^3$ after calibration.

Table 14. Statistical comparison of parameter and corresponding soil moisture profile

| | | Niger | | Benin | |
|---|---|---|---|---|---|
| | | before calibration | after calibration | before calibration | after calibration |
| RMSE of $\theta_g$ [$m^3/m^3$] | | 0.0686 | 0.0169 | 0.1222 | 0.0347 |
| $C_1$ [ - ] | average | 0.7598 | 0.0708 | 0.7086 | 0.0948 |
| | std. | 0.9998 | 0.0385 | 1.3039 | 0.0651 |
| | max. | 11.4101 | 0.1283 | 11.1209 | 0.2743 |
| | min. | 0 | 0.0019 | 0 | 0.0028 |
| $\theta_{geq}$ [$m^3/m^3$] | average | 0.0520 | 0.0352 | 0.2591 | 0.1549 |
| | std. | 0.0261 | 0.0046 | 0.0420 | 0.0470 |
| | max. | 0.1030 | 0.0472 | 0.3436 | 0.2993 |
| | min. | 0 | 0.0255 | 0 | 0.1080 |

After the inverse calibration, inverted $C_1$ showed different distribution patterns, depending on their soil moisture levels and soil texture. In very dry and sandy soils (Figure 38-a), $C_1$ was in inverse proportion to surface soil moisture contents, as being consistent with equation (5-4). In moderately wet soils with less sand but higher clay fractions (Figure 38-b), $C_1$ was Gaussian-distributed with respect to surface soil moisture, as being consistent with Braud et al. (1993) and Giordani et al. (1996). Trend lines in Figure 38-a and b signify that

inverted $C_1$ appropriately expressed the relationship between $C_1$ and soil moisture (and soil texture) rather than random selection. In addition, by demonstrating lower $\theta_{geq}$ than root zone soil moisture levels, inverted $\theta_{geq}$ successfully characterized the soil hydraulic properties (i.e. $\theta_{geq} < \theta_{rz}$ for sandy soils) (Noilhan and Planton ,1989).

*Validation of inverted variables with soil moisture measurements*

Soil moisture contents estimated with inverted soil hydraulic variables were first validated with the AMMA super site data at a local scale and compared with the un-calibrated SVAT scheme using the soil maps-based PTFs. In Niger, as shown in Figure 39-a and Table 14, a Root-Mean-Square Difference (RMSD) between field measurement and SVAT scheme decreased from 0.0686 to 0.0169 $m^3/m^3$ after calibration. In Benin, as illustrated in Figure 6-b and Table 14, a RMSD significantly decreased from 0.1222 to 0.0347 $m^3/m^3$ after calibration. With respect to the root zone soil moisture, a change in RMSD before and after calibration was only marginal, as explained in a sensitivity analysis above. The high RMSD by the un-calibrated SVAT scheme is mainly attributed to uncertainty in $C_1$ and overestimated $\theta_{geq}$. More specifically, for the estimation of $C_1$, soil maps-based PTFs use (5-3) and (5-6) heavily relying on uncertatin $\theta_{wp}$, $\theta_{sat,}$ $C_{1sat}$ or other PTFs-based parameters (Brimelow et al., 2010; Juglea et al., 2010; Pellarin et al., 2009). Errors in these parameters can be largely propagated upto the estimation of $C_1$. For instance, according to the calibration of Pellarin et al. (2009), $\theta_{wp}$ was previously determined as 0.04 in Niger, while soil maps-based PTF estimates it at 0.105. By relationship (5-6), the error in $C_1$ is largely propagated by the error in $\theta_{wp}$, showing a large discrepancy in its estimation between 2.9252 (with calibrated $\theta_{wp}$ of 0.04) and 0.2954 (with default $\theta_{wp}$ of 0.105), and suggesting the potential mis-estimation of surface soil moisture as a consequence. Therefore, calibration is needed for various reasons such as error propagation from uncertainty of PTFs-based supplementary coefficients and imperfect formulation inappropriately assuming the vertical homogeneity or insufficiently characterizing the vertical water movement in sandy soils (Montaldo and Albertson, 2001).

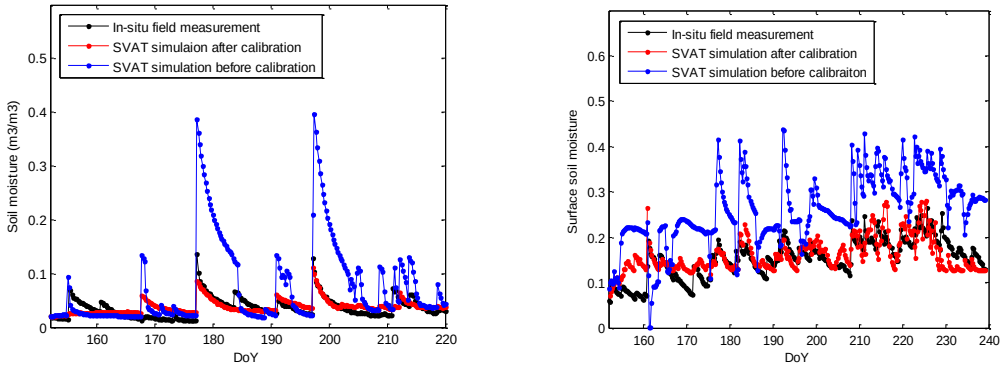


(a) (b)

Figure 39. Comparison of surface soil moisture before and after the calibration: (a) at Niger site and (b) Benin site. Unit: $m^3m^{-3}$

2.3.3.2. EnKF analysis of SMOS data

EnKF was implemented at each SVAT simulation time step (which also corresponds to the data acquisition time of 1 day SMOS products, approximately). It was considered that EnKF successfully solved the observation errors, taking account of reduced RMS error for field measurements after data assimilation. Detailed statistics of EnKF results are demonstrated in Table 15. The time-series comparisons at the point-local scale were demonstrated in Figure 41.

Table 15. Statistics of the EnKF results used for the spatial calibration. unit: $m^3m^{-3}$

| SVAT time step (DoY) | RMSE | RMSE in Niger (Before) | RMSE in Niger (After) | RMSE in Benin (Before) | RMSE in Benin (After) |
|---|---|---|---|---|---|
| 176.25 | 0.0493 | 0.0047 | 0.0006 | 0.0517 | 0.0421 |
| 177.25 | 0.0983 | - | - | - | - |
| 178.25 | 0.0759 | - | - | - | - |
| 179.25 | 0.0751 | 0.0496 | 0.0163 | 0.1390 | 0.0541 |
| 180.25 | 0.0718 | - | - | - | - |

| | | | | | |
|---|---|---|---|---|---|
| 181.25 | 0.0715 | 0.0343 | 0.0017 | 0.1486 | 0.0352 |
| 182.25 | 0.1009 | - | - | - | - |
| 183.25 | 0.0867 | - | - | - | - |
| 184.25 | 0.0986 | 0.0103 | 0.0097 | 0.1175 | 0.0319 |
| 185.25 | 0.0836 | - | - | - | - |
| 186.25 | 0.0703 | 0.0409 | 0.0312 | 0.2067 | 0.1129 |
| 187.25 | 0.0684 | 0.0221 | 0.0138 | - | - |
| 188.25 | 0.1241 | - | - | - | - |

All the estimations are the spatial average for the entire study domain on each DoY. The RMSD indicated in the 2nd column shows a difference between true field (i.e. SMOS data) and EnKF final analysis. Small RMSD may imply the successful convergence in data assimilation. Spread in the 3rd cloumn estimates the ensemble anomaly standard deviation, indicating a degree of model errors. Correlation is a relationship between ensemble mean and true field. All the correlations are higher than 0.7, impliying the better probability to be converged with the observations. The RMSD in the 5th to 6th column of Table 15 estimates a mismatch of SMOS L3 product (indicated by 'before') and of EnKF final analysis (indicated by 'after') for field measurements in the Niger site, respectively. The same caption is applied for the Benin site in the 7th to 8th column. Through the 5th to 8th column, it was demonstrated that the RMSD significantly decreased after data assimilation, sucessfully filtering out errors from the observations. The spatial average in the 9th column estimates a spatial average of the EnKF final analysis throughout the entire study domain. For example, 0.1627 on DoY 176.25 line in the 9th column estimates a spatial average of the EnKF final analysis shown in Figure 40-b. Overall, the errors associated with SMOS L3 products were considered to be mitigated after data assimilation (Reichle and Koster, 2004; Reichle et al., 2007; Reichle, 2008).

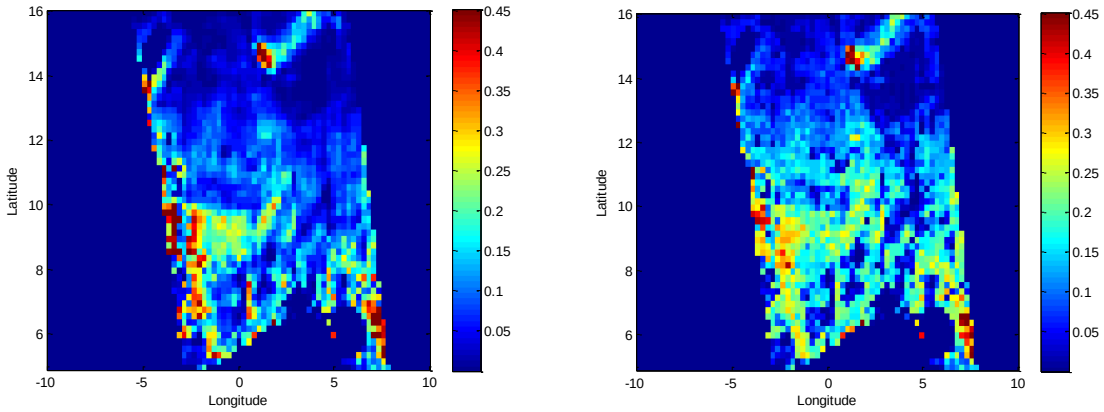


(a) (b)

Figure 40. (a) SMOS surface soil moisture; (b) EnKF final analysis. DoY 176. Unit: $m^3m^{-3}$

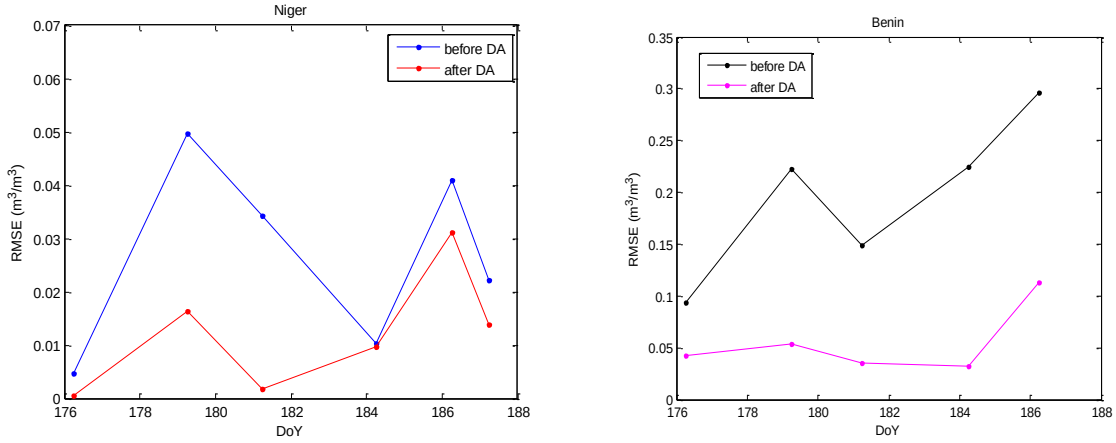


(a) (b)

Figure 41. Reduction in RMSE after data assimilation: (a) Niger, (b) Benin. Unit: $m^3/m^3$.

2.3.3.3. Meso-scale calibration of soil hydraulic variables

For a spatial comparison, the SVAT estimations simulated on a daily basis (also corresponding to 1 day SMOS data acquisition time) were assembled in line with 3 day SMOS L3 data acquisition time (i.e. DoY 186 to 188) in order to provide adequate spatial coverage throughout the study domain. Thus, at a spatial scale, a time difference between SVAT estimation time and SMOS data acquisition time is marginal.

*Characterization of inverted SVAT variables on dry and sandy conditions*

Inverted SVAT variables $C_1$ and $\theta_{geq}$ were demonstrated in Figure 42 and 43, respectively, and compared with the soil maps-based PTFs usually used in the original ISBA model (Noilhan &

Mahfouf, 1996). Before calibration, the soil maps-based PTFs showed the Gaussian distribution, estimating lower $C_1$ values in wet area by rain and clay soils suggesting slow infiltration rates (e.g. area around at a longitude of -5 to -7 and area at a longitude of 3 to 8 and a latitude of 10 to 15. (see Figure 16) but higher $C_1$ values in moderately wet area. On the other hand, the inversion calibration scheme showed different contrast and variability. It presented higher $C_1$ values in wet area by rain and clay soils but lower values in moderately wet area, suggesting a Gaussian distribution with different expected value and variance. In terms of a spatial variability, un-calibrated $C_1$ showed much higher average and spread than the soil maps-based PTFs, as shown in Table 16, suggesting the possibility for overestimation of soil moisture as a consequence. A spatial average of $C_1$ throughout the entire study domain was found to be lower at 0.1358 after calibration (Figure 42-a), but higher at 1.3726 before calibration (Figure 42-b). For a statistical comparison, a standard deviation of $C_1$ was found to be much lower at 0.1029 after calibration, but higher at 1.6822 before calibration, suggesting potentially over-estimated contrasts by the soil maps-based PTFs. In addition, as shown in Figure 43, inverted $\theta_{geq}$ was compared with the soil maps-based PTFs. As shown in Table 16, a spatial average of $\theta_{geq}$ was estimated at 0.0935 after calibrations and higher at 0.1406 before calibration. The standard deviation of $\theta_{geq}$ was estimated at 0.0679 after calibration and higher at 0.0992 before calibration. It was demonstrated that inverted $\theta_{geq}$ successfully characterized the soil hydraulic property of vertical contrasts in matric potentials, while the soil maps-based PTFs estimated $\theta_{geq}$ to be similar to the spatial distribution and magnitude of root zone soil moisture, and failed to express a factor of sandy soil texture (Noilhan & Planton, 1989; Montaldo and Albertson, 2001).

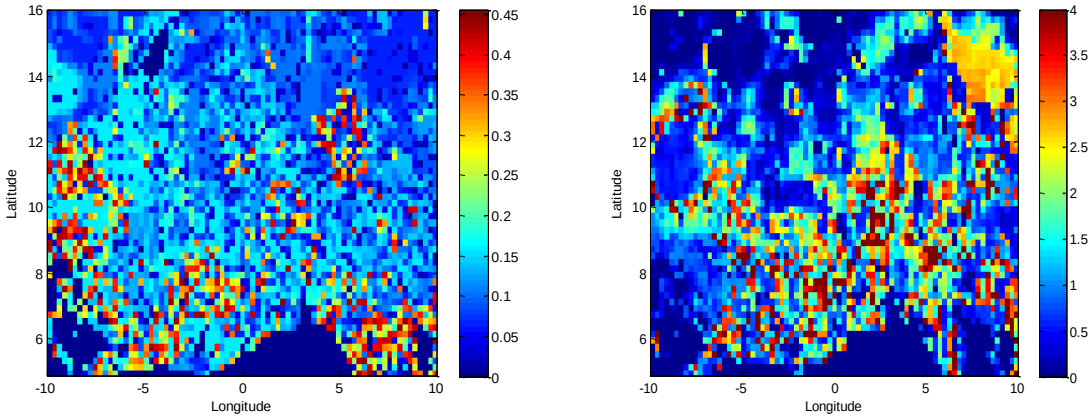


(a) (b)

Figure 42. $C_1$ estimated (a) after calibration and (b) before calibration.

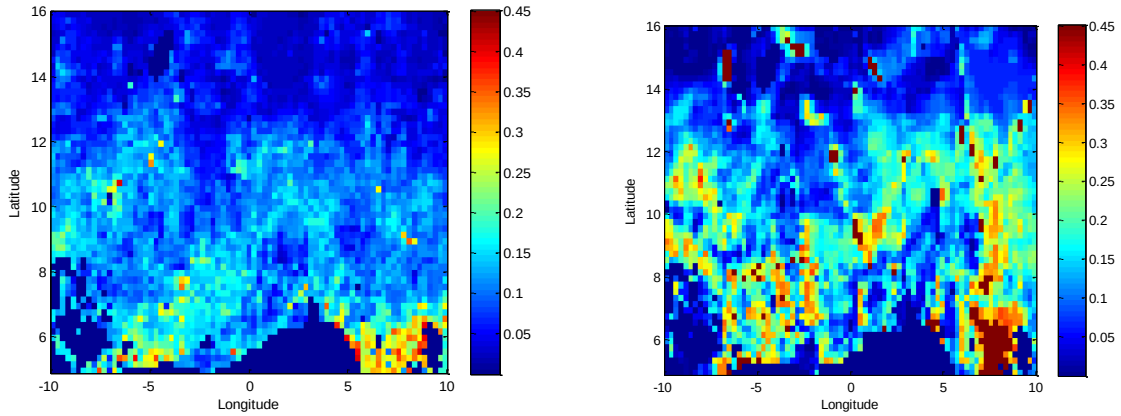


(a) (b)

Figure 43. $\theta_{geq}$ estimated (a) after calibration and (b) before calibration. Unit: $m^3m^{-3}$

Table 16. Spatial average comparison of parameter and corresponding soil moisture, unit: $m^3m^{-3}$.

| SVAT scheme | $C_1$ | $\theta_{geq}$ | $\theta_g$ | $\theta_{rz}$ |
|---|---|---|---|---|
| Inverse calibration | 0.1358 (Fig. 8-a) | 0.0935 (Fig. 9-a) | 0.1085 (Fig. 10-a) | 0.1357 (Fig. 11-a) |
| soil maps-based PTFs | 1.3726 (Fig. 8-b) | 0.1406 (Fig. 9-b) | 0.1478 (Fig. 10-b) | 0.1361 (Fig. 11-b) |

*Spatial distribution of soil moisture in the typically arid regions*

Surface soil moisture was determined by the calibrated SVAT scheme using inverted $C_1$ and $\theta_{geq}$ values and further compared with the un-calibrated SVAT scheme using the soil maps-based PTFs. Similarly to the results at a local scale, surface soil moisture in dry and sandy soils was overestimated by the un-calibrated SVAT scheme, as shown in Figure 44-b. This overestimation problem was previously reported by Juglea et al., (2010). This is also supported by comparison with the calibrated SVAT scheme (Figure 44-a) and SMOS L3 product (Figure 44-c) in this study. As illustrated in Table 4, a spatial average for surface soil moisture simulated with the un-calibrated SVAT scheme is higher at 0.1478 $m^3/m^3$ than the calibrated SVAT scheme at 0.1085 $m^3/m^3$. It was higher than that of SMOS data at 0.1337 $m^3/m^3$ that reported run-off (presumably radiometric errors) over the area (i.e. longitude of -5 to -7 in Figure 44-c) presumably in the presence of standing water caused by rainfall fallen on the clay surface (see Figure 34). In addition to the SMOS run-off area, the rainfall effect in another area (i.e. longitude of 3 to 8 and latitude of 10 to 15 in Figure 44-b) was also significantly overestimated by the un-calibrated SVAT scheme. Other than such rainfall effect, the un-calibrated SVAT scheme mostly reported the saturated soil moisture levels in other moderately wet regions with no rainfall events. This overestimation of the

un-calibrated SVAT scheme is attributed to the overestimated $\theta_{geq}$ and $C_1$ values (stemming from erroneous wilting point, saturated soil moisture, $C_{1sat}$, or b) by the soil maps-based PTFs as discussed above. In contrast, the wet area estimated by the calibrated SVAT scheme was spatially reasonably coincided with the area in the rain on the precedent day. No saturated soils were estimated. Table 17 shows the soil moisture spatial analysis that estimates a pixel nearest to each local station, for a point-scale validation. As shown in Table 17, in Benin, surface soil moisture estimated with the calibrated SVAT scheme is better matched with field measurement than SMOS data and the un-calibrated SVAT scheme. In Niger, it is just compared to the un-calibrated SVAT scheme but better than SMOS data.

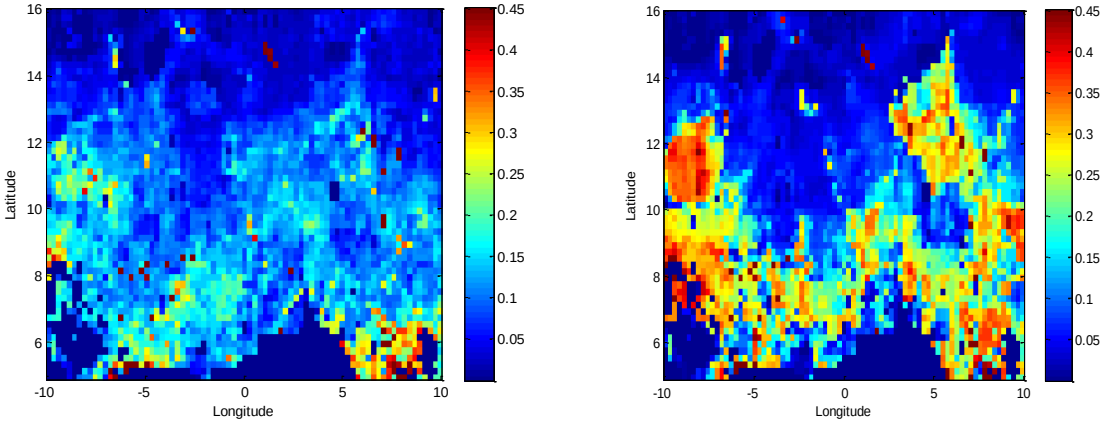


(a) (b)

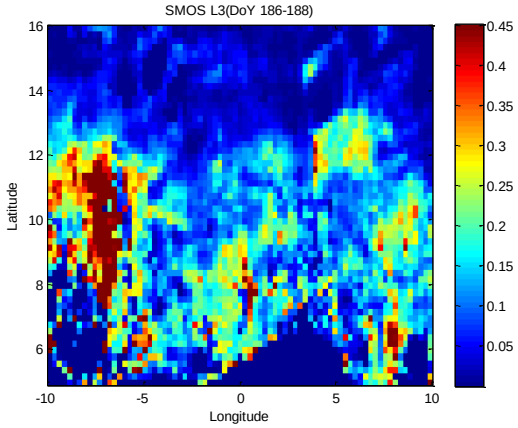


(c )

Figure 44. Surface soil moisture:
(a) after calibration; (b) before calibration; (c) SMOS L3 product. Unit: $m^3m^{-3}$

The root zone soil moisture was also illustrated in Figure 45. As discussed in sensitivity analysis at a local scale and shown in Table 17, root zone soil moisture did not show much change

after calibration. This is primarily due to the fact that inverted variables principally influence the surface layer than the root zone soil layer, according to (5-1). Unlike surface soil moisture, the root zone soil moisture showed wet soil conditions at area in the rain as well as at other areas without the rainfall events. Thus, by combining surface soil moisture with root zone, it was concluded that only the calibrated SVAT scheme could successfully capture a typical dry climatic soil profile, in which soil is dry in the surface layer but wet in the deeper layer (Escorihuela et al., 2010). It was also shown that root zone layer is independent from surface exchange activity such as surface soil evaporation and rainfall.

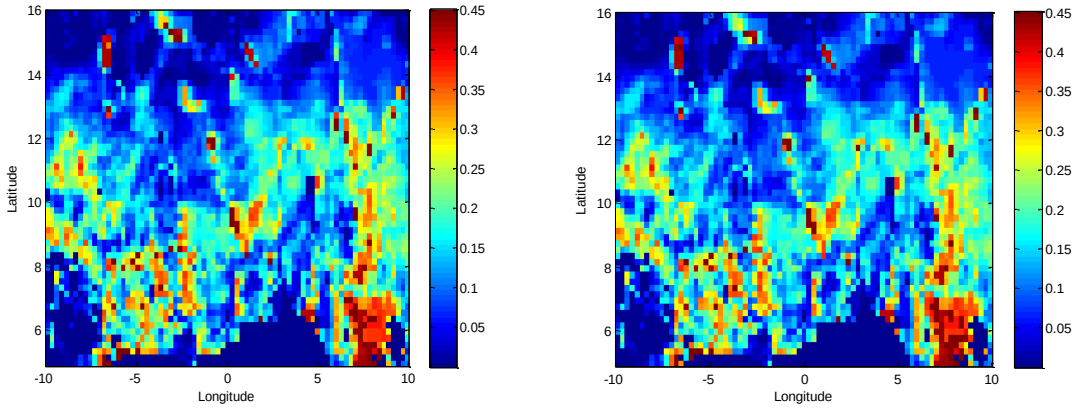


(a) (b)

Figure 45. Root zone soil moisture: (a) after calibration; (b) before calibration. Unit: $m^3m^{-3}$

Table 17. Point-scale comparison between field measurement and spatial analysis in the nearest pixel. unit: $m^3m^{-3}$.

| Methods | Surface soil moisture in Niger | Root zone soil moisture in Niger | Surface soil moisture in Benin | Root zone soil moisture in Benin |
|---|---|---|---|---|
| Field measurement | 0.0432 | 0.0468 | 0.1326 | 0.2434 |
| Calibrated SVAT | 0.0277 | 0.0634 | 0.1206 | 0.1989 |
| SMOS L3 product | 0.0022 | - | 0.3393 | - |
| Un-calibrated SVAT (soil maps-based PTFs) | 0.0346 | 0.0623 | 0.1864 | 0.1980 |

2.3.3.4. Conclusion and Summery

Because the soil maps-based PTFs are empirically defined and validated for limited sites, there is a limitation for widely applying it to the heterogeneous land surface conditions on the meso-scale. Thus, this paper suggested a meso-scale calibration framework of inverting the SVAT soil hydraulic variables from globally available SMOS surface soil moisture. The EnKF analysis of SMOS surface soil moisture was employed to mitigate any potential SMOS errors often found in dry and sandy soils during WAM and to adjust some structural discrepancy between SMOS instrument and land surface model physics (e.g. a change in penetration depth in SMOS instrument). At a local scale, the results indicated that the overestimation of $\theta_{geq}$ by imperfect formulation and $C_1$ by the soil maps-based PTFs was successfully resolved, consequently demonstrating a better match with field measurements and appropriately characterizing the soil hydraulic property in dry and sandy soils. At a spatial scale, the un-calibrated SVAT scheme showed the significant overestimation of surface soil moisture. Mostly, it is attributed to the overestimation of $\theta_{geq}$ inappropriately parameterized and $C_1$ heavily relying on erroneous associated coefficients such as wilting point or saturated soil moisture. By using inverted soil hydraulic variables in SVAT scheme, this overestimation of surface soil moisture by the soil maps-based PTFs was successfully resolved. Accordingly, it was concluded that one of the key determinants for the estimation of surface soil moisture is soil and hydraulic property. Additionally, only the calibrated SVAT scheme captured a typical dry climatic condition where the surface is dry but the root zone is wet, regardless of a spatial distribution of surface moisture or rainfall. The operational merit of this study is that there is no need to heavily rely on empirically defined PTFs or land surface parameterizations. Consequently, this approach is useful for meso-scale study. With respect to joint parameter-state estimation through EnKF, this approach is more flexible because this does not require thorough parameter error characterization and can be applied when parameter is highly uncertain.

CHAPTER 5

# Conclusions

In this thesis, the novel approach estimating the land surface properties on two different semi-arid regions was suggested. In sandy and dry soils such as Tibetan Plateau and West Africa, it is difficult to estimate the land surface properties with both satellite data and model estimates. Soil texture or global soil map-based PTFs often used in a SVAT model significantly misestimate soil coefficients. In addition, the main source of satellite retrieval errors usually come from sandy and dry conditions. Thus, in this thesis, the land surface properties were inverted from the EnKF analysis of satellite or field observations, instead of formulation or parameterization approach. It was very possible to invert the aerodynamic roughness from heat flux, due to their positive relationship for convective momentum characteristics. Similarly, it was also possible to invert the SVAT soil and hydraulic variables from soil moisture, because surface variables are formulated as a function of soil moisture.

Herefrom, instead of directly using the observations for inversion, the EnKF analysis was employed as reference data. Especially for the application of satellite data, it is required to filter out satellite errors, because their errors are often very large especially in sandy and dry regions. If the observation is contaminated, then its errors can be largely propagated through inversion to the estimation of geophysical parameters. Thus, various regimes were explored to optimize the EnKF. The stationary and sequential EnKF schemes were compared to assess the benefits coming from a sequentiality of EnKF. Because the stationary ensemble-based Ensemble Optimal Interpolation (EnOI) scheme is a computationally cost-effective but usually suboptimal approach, the two-step stationary EnKF scheme empirically defining the observation errors with a SMOS L2 processor

was assessed with respect to the sequential EnKF assuming the global constant *a priori* errors. The point-scale comparison results showed that the two-step stationary EnKF scheme was better matched with the field measurements at the AMMA sites than the original SMOS L3 data and sequential EnKF scheme. In specific, the spatial average of brightness temperature perturbation scheme of three stationary ensemble groups (i.e. brightness temperature, geophysical parameters, land use-based fraction factor) was similar to that of the sequential EnKF. At a spatial scale, it mitigated the rainfall-induced run-off errors, vegetation attenuation and underestimations by an inappropriate dielectric constant model in dry sandy soils. It was suggested that the sequential EnKF scheme consuming a longer record of satellite data may not be required if the SMOS brightness temperature errors in EnOI are empirically adjusted at a pixel scale. The operational merit of the two-step stationary EnKF scheme lies within a short analysis time step, when compared with the Cumulative Distribution Functions (CDF) and the sequential EnKF scheme. Additionally, there is no need to assume a slow evolution or a global constant for the observation error parameters in the observation operator of EnKF or to define the length of the localising function for reducing the sampling errors. In contrast, when defining the observation errors from *a priori* knowledge based upon the field measurements, the performance of sequential EnKF was better than the stationary EnOI because ensemble spread evolves with time.

These EnKF analyses were further employed as reference data for parameter inversion. First, the aerodynamic roughness height, a key input required for various models such as land surface model, energy balance model or weather prediction model, was inverted from the EnKF analysis of heat flux. The aerodynamic roughness height inverted was consistent with eddy covariance results and literature values. Consequently, this method rectified the sensible heat overestimated and latent heat flux underestimated by the original SEBS model, demonstrating better heat flux estimations especially during the summer Monsoon period in the Tibetan Plateau. The advantages of this method are that it is time-variant over vegetation growth, not affected by the saturation problem of remotely sensed vegetation index, and useful even when eddy covariance data are absent in the fields. In addition, two soil hydraulic input variables of SVAT model were also inverted from EnKF-analyzed SAR and SMOS surface soil moisture products over the Tibet-GAME datasets and the AMMA datasets, respectively. The results demonstrated that the calibrations of two soil hydraulic variables, soil surface variable $C_1$ and equilibrium soil moisture $\theta_{geq}$, solved the misestimation problem due to the vertical homogeneity assumption and empirical PTFs in the original SVAT scheme. The calibrated SVAT estimation was better matched with the field measurement than the satellite data and un-calibrated SVAT scheme using FAO soil maps-based PTFs. On the meso-scale, the calibrated SVAT scheme appropriately captured a non-linear relationship between surface and root zone soil moisture, showing a typical dry climatic condition, in which dry surface was spatially consistent with the rainfall events, while wet root zone showed low correlations with surface soil moisture dynamics and rainfall events. This finding was also applicable to highly stratified semi-arid soils as in Tibetan Plateau. In contrast, the un-calibrated

SVAT model significantly overestimated surface soil moisture and rainfall effect. Accordingly, it was concluded that one of the key determinants for soil moisture profile is soil and hydraulic property for the determinaton of soil moisture profile. This approach suggests several operational merits in that there is no need to heavily rely on site-specifically defined empirical PTFs, and this can be applied even when model input is highly uncertain. Future work may include the application of aerodynamic roughness inversion to satellite-estimated heat flux. Inversion approach may also be extended into the estimation of subsuface soil properties such as saturated hydraulic conductivity.

**Reference**

Anderson, J.L.. (2001). An Ensemble Adjustment Kalman Filter for Data Assimilation. Monthly Weather Review. Vol.129. 2884-2903

Á lvarez-Mozos, J., Verhoest, N.E., Larrañaga, A., Casalí, J., González-Audícana, M. (2009). Influence of Surface Roughness Spatial Variability and Temporal Dynamics on the Retrieval of Soil Moisture from SAR Observations. Sensors. 9, 463-489.

AMMA-ISSC. (2010). The International Science Plan for AMMA 2010-2020, www.amma-international.org/IMG/pdf/ISP2_v2.pdf, 136 pp. ISP Phase 2 Version 2.
Anderson, J.L.. 2001. An Ensemble Adjustment Kalman Filter for Data Assimilation. Monthly Weather Review. Vol.129. 2884-2903.

Baghdadi, N., King, C., Bourguignon, A., Remond, A. 2002. Potential of ERS and Radarsat data for surface roughness monitoring over bare agricultural fields: application to catchments in Northern France. Int. J. Remote Sens. 23, 3427-3442.

Baghdadi, N., Gherboudj, I., Zribi, M., Sahebi, M., King, C., Bonn, F. 2004. Semi-empirical calibration of the IEM backscattering model using radar images and moisture and roughness field measurements. Int. J. Remote Sensing. 25, 3593-3623.

Baghdadi, N., Holah, N., Zribi, M. 2006. Soil moisture estimation using multi-incidence and multipolarization ASAR SAR data. Int. J. Remote Sens. 27, 1907-1920.

Beljaars, A.C.M., Schotanus, P., Nieuwstadt, F.T.M. (1983). Surface layer similarity under nonuniform fetch conditions, Journal of Climate and Applied Meteorology, 22, 1800-1810.

Bindlisha, R, Barros, A.P. (2000). Parameterization of vegetation backscatter in radar-based, soil moisture estimation. Remote Sens. Environ., 76, 130-137.

Boone, A., Calvet, J.-C., Noilhan, J. (1999). The inclusion of a third soil layer in a Land Surface Scheme using the Force-Restore method., J. Appl. Meteorol., 38, 1611–1630.

Boulain, N., Cappelaere, B., Ramier, D., Issoufou, H. B. A., Halilou, O., Seghieri, J., Guillemin, F., Oï, M., Gignoux, J., Timouk, F.. (2009). Towards an understanding of coupled physical and biological processes in the cultivated Sahel - 2. Vegetation and carbon dynamics. Journal of Hydrology, 375. 190–203.

Boulet, G. , Braud, I. , Vauclin. M. (1997). Study of the mechanisms of evaporation under arid conditions using a detailed model of the soil–atmosphere continuum. Journal of Hydrology, 193, 114–141.

Braud, I., Noilhan, J., Bessemoulin, P., Mascart, P., (1993). Bare-ground surface heat and water exchange under dry conditions: observations and parameterization, Boundary-Layer Meteorology, 66, 173-200.

Brimelow, J.C., Hanesiak, J.M., Raddatz, R., 2010. Validation of soil moisture simulations from the PAMII model, and an assessment of their sensitivity to uncertainties in soil hydraulic parameters, Agricultural and Forest Meteorology, 150, 100-114.

Calvet, J.C., Noilhan, J. (2000). From near-surface to root-zone soil moisture using year-round data. Journal of Hydrometeorology 1 (5), 393-41.

Cammalleri, C., Agnese, C., Ciraolo, G., Minacapilli, M., Provenzano, G., Rallo, G.. (2010). Actual evapotranspiration assessment by means of a coupled energy/hydrologic balance model: Validation over an olive grove by means of scintillometry and measurements of soil water contents, Journal of Hydrology, 392 (1–2), pp 70-82, doi:10.1016/j.jhydrol.2010.07.046.

Cappelaere, B., Descroix, L., Lebel, T., Boulain, N., Ramier, D., Laurent, J.-P., Favreau, G., Boubkraoui, S., Boucher, M., Moussa, I. B., Chaffard, V., Hiernaux, P., Issoufou, H. B. A., Le Breton, E., Mamadou, I., Nazoumou, Y., Oï, M., Ottlé, C., Quantin, G.. (2009). The AMMA-CATCH experiment in the cultivated Sahelian area of south-west Niger - Investigating water cycle response to a fluctuating climate and changing environment. Journal of Hydrology, 375. 34–51.

Champeaux, L., Masson, V., Chauvin, F.. (2005). ECOCLIMAP: a global database of land surface parameters at 1 km resolution. Meteorol. Appl. 12, 29–32. doi:10.1017/S1350482705001519.

Chavez, J.L., Neale, C.M.U., Hipps, L.E., Prueger, J.H., Kustas, W.P. (2005). Comparing aircraft-based remotely sensed energy balance fluxes with eddy covariance tower data using heat flux source area functions. J. Hydromet., AMS, 6(6), 923–940.

Chen, K.S., Wu, T.D., Tsang, L., Li, Q., Shi, J., Fung, A.K. (2003). Emission of rough surfaces calculated by the integral Equation method with comparison to three-dimensional moment method simulations. IEEE Trans. Geosci. Remote Sens., 41,90-101.

Chen, R.K., Yang, C. M.. (2005). Determining the Optimal Timing for Using LAI and NDVI to Predict Rice Yield. Journal of Photogrammetry and Remote Sensing. 10(3): 239-254.

Choudhury, B. J., Monteith, J. L.. (1988). A four-layer model for the heat budget of homogeneous land surfaces, Q. J. Roy. Meteor. Soc., 114, 373–398.

Choi, T., Kim, J., Lee, H., Hong, J., Asanuma, J., Ishikawa, H., Gao, Z., Wang, J., Koike., T. (2004). Turbulent exchange of heat, water vapor, and momentum over a Tibetan prairie by eddy covariance and flux variance measurements, J. Geophys. Res., 109.

Clapp R.B., Hornberger G.M. (1978). Empirical equation for some soil hydraulic properties, Water Resources Research, 14(4), 601-604.

Cosby, B.J., Hornberger, G.M., Clapp, R.B., Ginn, T.R. (1984). A Statistical Exploration of the Relationships of Soil Moisture Characteristics to the Physical Properties of Soils. Water Resources Research., 20(6),682–690, doi:10.1029/WR020i006p00682.

Counillon F., Bertino L. (2009). Ensemble Optimal Interpolation: multivariate properties in the Gulf of Mexico, Tellus A, 61(2), 296-308, DOI: 10.1111/j.1600-0870.2008.00383.x.

Crow, W.T., Kustas, W.P., Prueger, J.H. (2008). Monitoring root-zone soil moisture through the assimilation of a thermal remote sensing-based soil moisture proxy into a water balance model. Remote Sens. Environ., 112 (4), 1268-128.

Crow, W. T., Ryu, D.. (2009). A new data assimilation approach for improving runoff prediction using remotely-sensed soil moisture retrievals, Hydrol. Earth Syst. Sci., 13, 1-16, doi:10.5194/hess-13-1-2009.

de Bruin, H.A.R., Verhoef, A.. (1997). A new method to determine the zero-plane displacement. Boundary Layer Meteor., 82,159-164.

de Lannoy, G., Houser, P., Verhoest, N., Pauwels, V.. (2009). Adaptive soil moisture profile filtering for horizontal information propagation in the independent column-based CLM2.0, Journal of Hydrometeorology, 10(3), 766–779.

de Rosnay P., Wigneron J. P.. (2005). Parameterizations of the effective temperature for L-band radiometry. Intercomparison and long term validation with SMOSREX field experiment, Radiative Transfer Models for Microwave Radiometry, C. Mätzler, Ed., ed Stevenage, UK: Institution of Electrical Engineers.

Dee, D. P., Da Silva, A. M.. (1998). Data assimilation in the presence of forecast bias. Q.J.R. Meteorol. Soc., 124: 269–295. doi: 10.1002/qj.49712454512.

Descroix, L., Mahé, G., Lebel, T., Favreau, G., Galle, S., Gautier, E., Olivry, J.-C., Albergel, J., Amogu, O., Cappelaere, B., Dessouassi, R., Diedhiou, A., Le Breton, E., Mamadou, I. & Sighomnou, D.. (2009). Spatio-temporal variability of hydrological regimes around the boundaries between Sahelian and Sudanian areas of West Africa: A synthesis. Journal of Hydrology, 375. 90–102.

Dunne, S., Entekhabi, D. (2006). Land surface state and flux estimation using the ensemble Kalman smoother during the Southern Great Plains 1997 field experiment. Water Resources Research., 42, W01407, DOI:10.1029/2005WR004334.

ECOWAS-SWAC/OECD. (2007). Rural areas and agricultural changes. The Atlas on regional integration in West Africa. www.oecd.org/swac/publications/38903590.pdf. Accessed on March 14, 2013.

Escorihuela, M.J., Kerr, Y., Wigneron, J.P., Calvet, J.C., Lemaître, F.. (2007). A simple model of the bare soil microwave emission at L- Band. IEEE Geosci. Remote Sens., 45, pp. 1978-1987.

Escorihuela, M.-J., Chanzy, A., Wigneron, J.-P., Kerr, Y.. (2010). Effective soil moisture sampling depth of L-band radiometry: A case study, Remote Sensing of Environment, vol. 114, pp. 995-1001.

Evensen, G. (2003). The ensemble Kalman filter: Theoretical formulation and practical implementation. Ocean Dynamics., 53, 343−367.

Evensen, G. (2004). Sampling strategies and square root analysis schemes for the EnKF. Ocean Dyn. 54,539-560.

FAO-SWAC. (2007). Rurality in motion in West Africa. FAO, Rome, Italy.

February, E.C., Higgins, S.I. (2010).The distribution of tree and grass roots in savannas in relation to soil nitrogen and water. South African Journal of Botany. 76, 517–523.

Fertig, E. J., Baek, S.-J., Hunt, B. R., OTT, E., Szunyogh, I., Aravéquia, J. A., Kalnay, E., LI, H. and LIU, J.. (2009). Observation bias correction with an ensemble Kalman filter. Tellus A, 61: 210–226. doi: 10.1111/j.1600-0870.2008.00378.x.

Foken, T.H. (2008). The energy balance closure problem: an overview. Ecological Applications 18:1351–1367. http://dx.doi.org/10.1890/06-0922.1

Foken, T.H., Wichura, B. (1996). Tools for quality assessment of surface-based flux measurements. Agr. Forest. Meteorol. 78, 83-105.

Fung, A.K. (1994).Microwave scattering and emission models and their applications, Boston: Artech House Publishers.

Galantowicz, J. F., Entekhabi, D., Njoku, E. G. (1999). Tests of sequential data assimilation for retrieving profile soil moisture and temperature from observed L-band radiobrightness. IEEE Trans. Geosci. Remote Sens., 37(4), 1860−1870.

Geman, S.,Bienenstock, E.,Doursat, R. (1992). Neural networks and the bias/variance dilemma. Neural Computation, 4, 1-58.

Giordani, H., Noilhan, J., Larrère, P., Bessemoulin, P. (1996). Modelling the surface processes and the atmospheric boundary layer for semi-arid conditions. Agricultural and Forest Meteorology., 80 (2–4), 263–287.

Goegebeur, M., Pauwels, V. R. N. (2007). Improvement of the PEST parameter estimation algorithm through Extended Kalman Filtering, J. of Hydrology, 337, 436— 451.

Gruhier, C., de Rosnay, P., Kerr, Y., Mougin, E., Ceschia, E., Calvet, J.-C., Richaume, P.. (2008). Evaluation of AMSR-E soil moisture product based on ground measurements over temperate and semi-arid regions, Geophys. Res. Lett., 35, L10405, doi:10.1029/2008GL033330.

Gutmann, E. D., Small, E. E. (2007). A comparison of land surface model soil hydraulic properties estimated by inverse modeling and pedotransfer functions, Water Resour. Res., 43, W05418, doi:10.1029/2006WR005135.

Hendricks-Franssen, H. J., Kinzelbach. W. (2009). Ensemble Kalman filtering versus sequential self-calibration for transient inverse modeling of dynamic groundwater flow systems, Journal of Hydrology 365, 261-274, doi:10.1016/j.jhydrol.2008.11.033.

Hoeben, R., Troch, P. A. (2000). Assimilation of active microwave obser- vation data for soil moisture profile estimation. Water Resources Research. 36(10), 2805−2819.

Holmes, T.R.H., Drusch, M., Wigneron, J. P., de Jeu, R.A.M.. (2008). A global simulation of microwave emission: error structures based on output from ECMWF's operational integrated forecast system," Geoscience and Remote Sensing, IEEE Transactions on , vol.46, no.3, pp.846,856, doi: 10.1109/TGRS.2007.914798.

Houser, P. R., Shuttleworth, W. J., Gupta, H. V. (1998). Integration of soil moisture remote sensing and hydrologic modeling using data assimilation. Water Resource Research. 34(12), 3405−3420.

Huang, C-h., Bradford, J.M. (1992). Applications of a laser scanner to quantify soil microtopography. Soil Sci. Soc. Am. J. 56, 14-21.

Huang, C., Li, X., Lu, L., Gu. J. (2008). Experiments of one-dimensional soil moisture assimilation system based on ensemble Kalman filter. Remote Sens. Environ. 112, 888-900.

Intsiful, J., Kunstmann, H. (2008). Upscaling of land-surface parameters through inverse. stochastic svat-modelling, Boundary-Layer Meteorol, 129, 137–158, doi 10.1007/s10546-008-9303-0.

Jackson, T. J., Bindlish, R., Cosh, M. H., Zhao, T., Starks, P. J., Bosch, D. D., Seyfried, M., Moran, M. S., Goodrich, D. C., Kerr, Y. H., Leroux, D.. (2012). Validation of Soil Moisture and Ocean Salinity (SMOS) Soil Moisture Over Watershed Networks in the US, IEEE T. Geosci. Remote Sens., 50, 1530–1543, doi:10.1109/tgrs.2011.2168533.

Jacquette, E., Al Bitar, A., Mialon, A., Kerr, Y., Quesney, A., Cabot, F., Richaume. P.. (2010). SMOS CATDS level 3 global products over land. Remote sensing for agriculture, ecosystems, and hydrology xii. doi:10.1117/12.865093.

Jarvis P.G. (1976). The interpretation of the variations in leaf water potential and stomatal conductance found in canopies in the field. Philos. Trans. Roy. Soc., B. 273, 593-610.

Juglea, S., Kerr, Y., Mialon, A., Wigneron, J.-P., Lopez-Baeza, E., Cano, A., Albitar, A., Millan-Scheiding, C., Carmen Antolin, M., Delwart, S. (2010). Modelling soil moisture at SMOS scale by use of a SVAT model over the Valencia Anchor Station, Hydrol. Earth Syst. Sci., 14, 831-846, doi:10.5194/hess-14-831-2010.

Jochum, M. A. O., de Bruin, H. A. R. Holtslag, A. A. M., Belmonte, A. C.. (2006). Area-Averaged Surface Fluxes in a Semiarid Region with Partly Irrigated Land Lessons Learned from EFEDA. Journal of Applied Meteorology and Climatology. 45, 856-874.

Keppenne, C. L., Rienecker, M.M., Kurkowski, N.P., Adamec, D.A.. (2005). Ensemble Kalman filter assimilation of temperature and altimeter data with bias correction and application to seasonal prediction. Nonlinear Proc Geophys,12, 491–503.

Kerr, Y., P. Waldteufel, P. Richaume, P. Ferrazzoli, J.-P. Wigneron. (2013). SMOS LEVEL 2 processor soil moisture algorithm theoretical basis document (ATBD) v1.3h. Toulouse, SM-ESL (CBSA): 141.

Kerr, Y.H., Waldteufel, P., Richaume, P., Wigneron, J.-P., Ferrazzoli, P., Mahmoodi, A., Al Bitar, A., Cabot, F., Gruhier, C., Juglea, S.E., Leroux, D., Mialon, A., Delwart, S.. (2012). The SMOS Soil Moisture Retrieval Algorithm. Geoscience and Remote Sensing, IEEE Transactions on , v. 50, no.5, pp.1384,1403, doi: 10.1109/TGRS.2012.2184548.

Kohsiek, W., de Bruin, H. A. R., The, H., van den Hurk, B.. (1993). Estimation of the sensible heat flux of a semi-arid area using surface radiative temperature measurements. Boundary Layer Meteor., 63, 213–230.

Kumar, S., Reichle, R., Peters-Lidard, C., Koster, R., Zhan, X., Crow, W., Eylander, J., Houser, P. (2008). A land surface data assimilation framework using the land information system: Description and applications. Advances in Water Resources. 31, 1419-1432.

Kunstmann, H. (2008). Effective SVAT-model parameters through inverse stochastic modelling and second-order first moment propagation, Journal of Hydrology, 348, 13-26.

Kurtz, W., Hendricks-Franssen, H.-J., Vereecken, H.. (2012). Identification of time-variant river bed properties with the ensemble Kalman filter. Water Resour. Res., 48, W10534. Doi:10.1029/2011WR011743.

Laur, H., Bally, P., Meadows, P., Sanchez, J.,Schaettler, B., Lopinto, E., Esteban, D. (2004). Derivation of the backscattering coefficient σ° in ESA ERS SAR PRI products. ESA publication. No: ES-TN-RS-PM-HL09, Issue 2, Rev. 5F.

Lebel, T., Cappelaere, B., Galle, S., Hanan, N. P., Kergoat, L., Levis, S., Vieux, B. E., Descroix, L., Gosset, M., Mougin, E., Peugeot, C., Séguis, L.. (2009). AMMA-CATCH studies in the Sahelian region of West-Africa: An overview. Journal of Hydrology, 375. 3–13.

Lebel, T., Parker, D. J., Flamant, C., Bourlès, B., Marticorena, B., Mougin, E., Peugeot, C., Diedhiou, A., Haywood, J. M., Ngamini, J. B., Polcher, J., Redelsperger, J.-L., Thorncroft, C. D..

(2010). The AMMA field campaigns: multiscale and multidisciplinary observations in the West African region. Q.J.R. Meteorol. Soc., 136: 8–33. doi: 10.1002/qj.486.

Lee, J. H., _____. To what extent can data assimilation reduce the SAR retrieval errors arising from a priori roughness information?, In Review.

Lee, J. H., _____. Spatial estimation of soil moisture profile in stratified soils on the Tibetan plateau using EnKF-analyzed SAR surface soil moisture, In Review.

Lee J.H., Pellarin, T., Kerr, Y. (2012a). Correlation between latent heat and SMOS surface soil moisture in West Africa region: Can latent heat be a proxy of soil moisture in data assimilation?, Proceedings of International conference African Association of Remote Sensing of the Environment (AARSE).

Lee, J.H., Pellarin, T., Kerr, Y. (2012b). Drought monitoring over the West Africa using SMOS soil moisture data. Invited oral session to African Association of Remote Sensing of the Environment (AARSE), 9th international conference. 29 Oct~2. Nov.

Lee J.H., Pellarin, T., Kerr. Y. (2014). Inversion of soil hydraulic properties from the EnKF analysis of SMOS soil moisture over West Africa, Agricultural and Forest Meteorology, doi:10.1016/j.agrformet.2013.12.009.

Lee, J.H., Pellarin, T., Kerr, Y. Comparison of sequential and stationary EnKF schemes for SMOS soil moisture over West Africa, In Review.

Lee, J.H., Ravazzani, G., Mancin, M., Su, Z. (2011). Land use-based estimation of aerodynamic roughness over the Piemonte basin in Italy using MODIS LAI. The 3rd Remote Sensing Symposium (RSS): 21st Century Challenges, Wageningen, Netherlands.

Lee, J.H., Su, Z., Ravazzani, G., Mancini. (2012c). Dynamics of aerodynamic roughness and root zone soil moisture in the Tibetan Plateau during the Asian Monsoon. The 4th AMMA international conference, Toulouse, France. 02~06, July.

Lee, J.H., Timmermans, J., Su, Z., Mancini, M. (2012d). Calibration of aerodynamic roughness over the Tibetan Plateau with Ensemble Kalman Filter analysed heat flux, Hydrol. Earth Syst. Sci., 16, 4291-4302, doi:10.5194/hess-16-4291-2012.

Li, F., Crow, W.T., Kustas, W.P. (2010). Estimating root-zone soil moisture via the simultaneous assimilation of thermal and microwave soil moisture retrievals. Advances in Water Resources, 33, 201-214.

Li, C., Ren, L.. (2011). Estimation of unsaturated soil hydraulic parameters using the ensemble Kalman filter. Vadose Zone J., 10, 1205-1227. Doi.10.2136/vjz2010.0159.

Li, L., Zhou, H., Gómez-Hernández, J. J., Hendricks Franssen, H.J. (2012). Jointly mapping hydraulic conductivity and porosity by assimilating concentration data via ensemble Kalman filter, Journal of Hydrology, 428–429, 152-169.

Lievens, H., Vernieuwe, H., Á lvarez-Mozos, J., De Baets, B., Verhoest, N.E. (2009). Error in Radar-Derived Soil Moisture due to Roughness Parameterization: An Analysis Based on Synthetical Surface Profiles. Sensors. 9, 1067-1093.

Liu, H., Foken, T. (2001). A modified Bowen ratio method to determine sensible and latent heat fluxes. Meteorologische Zeitschrift, 10, 71-80.

Loew, A., Schwank, M., Schlenz, F. (2009). Assimilation of an L-band microwave soil moisture proxy to compensate for uncertainties in precipitation data. IEEE Trans. Geosci. Remote Sens., 47, 2606 -2616.

Ma, J., Daggupaty, S.M..(1999). Using All Observed Information in a Variational Approach to Measuring z0m and z0t. American Meteorological Society, 1391-1401.

Ma, Y., Fan, S., Ishikawa, H., Tsukamoto, O., Yao, T., Koike, T., Zuo, H., Hu, Z., Su, Z.. (2005). Diurnal and inter-monthly variation of land surface heat fluxes over the central Tibetan Plateau area, Theoretical and Applied Climatology, 80, 259-273.

Ma,Y., Menenti, M., Feddes, R., Wang, J..(2008). Analysis of the land surface heterogeneity and its impact on atmospheric variables and aerodynamic and thermodynamic roughness lengths. J.Geophysical Research. 113.

Ma, Y., Tsukamoto, O., Wang, J., Ishikawa, H., Tamagawa, I.. (2002). Analysis of aerodynamic and thermodynamic parameters over the grassy marshland surface of Tibetan Plateau, Progress in Natural Sciences, 12(1), 36-40

Ma,Y.,Wang,Y.,Wu,R.,Hu,Z.,Yang,K.,Li,M.,Ma,W.,Zhong,L.,Sun,F.,Chen,X.,Zhu,Z.,Wang,S., Ishikawa. H. (2009). Recent advances on the study of atmosphere-land interaction observations on the Tibetan Plateau. Hydrol. Earth Syst. Sci., 13, 1103–1111.

Mahfouf, J.F., Noilhan, J. (1991). Comparative study of various formulations of evaporation from bare soil using in situ data. Journal of Applied Metrology. 30(9), 1354-1365.

Massman, W.J., (1997). An analytical one-dimensional model of momentum transfer by vegetation of arbitrary structure. Boundary Layer Meteor. 83, 407-421.

Mattia, F., Davidson, M.W.J., Le Toan, T., D'Haese, C.M.F., Verhoest, N.E.C., Gatti, A.M., Borgeaud, M. (2003). A comparison between soil roughness statistics used in surface scattering models derived from mechanical and laser profilers. IEEE Trans. Geosci. Remote Sens., 41, 1659-1671.

Mattia, F., Satalino, G., Dente, L., Pasquariello, G. (2006). Using a priori information to improve soil moisture retrieval from ENVISAT ASAR AP data in semiarid regions. IEEE Trans. Geosci. Remote Sens., 44, 900-912.

Margulis, S.A., McLaughlin, D., Entekhabi, D., Dunne, S. (2002). Land data assimilation and estimation of soil moisture using measurements from the Southern Great Plains 1997 Field Experiment. Water. Resour. Res., 38(12),1299, doi:10.1029/2001WR001114.

Marx., A., Kunstmann, H., Schuttemeyer, D., Moene. A.F.. (2008). Uncertainty analysis for satellite derived sensible heat fluxes and scintillometer measurements over Savannah environment and comparison to mesoscale meteorological simulation results. Agricultural and forest meteorology, 148, 656 – 667.

Mironov, V., Kerr, Y., Wigneron, J.-P., Kosolapova, L., Demontoux, F.. (2013). Temperature- and Texture-Dependent Dielectric Model for Moist Soils at 1.4 GHz, Geoscience and Remote Sensing Letters, IEEE , 10 (3), pp.419-423. doi: 10.1109/LGRS.2012.2207878.

Mironov, V., Bobrov, P. (2009). Spectroscopic microwave dielectric model of moist soils, Advances in Geoscience and Remote Sensing, Gary Jedlovec (Ed.), ISBN: 978-953-307-005-6,In Tech, www.intechopen.com/books/advances-in-geoscience-and-remotesensing /spectroscopic-microwavedielectric-model-of-moist-soils.

Montaldo, N., Albertson, J.D. (2001). On the Use of the Force–Restore SVAT Model Formulation for Stratified Soils. Journal of Hydrometeorology., 2,571–578, doi: http://dx.doi.org/10.1175/1525-7541(2001)002<0571:OTUOTF>2.0.CO;2

Montaldo,N.,Albertson, J.D.Mancini,M.(2007). Dynamic calibration with an Ensemble Kalman Filter based Data assimilation approach for root zone moisture predictions. Journal of hydrometeorology.

Montaldo, N., Albertson, J.D., Mancini, M., Kiely, G. (2001). Robust simulation of subsurface soil moisture with assimilation of surface soil moisture data. Water Resources Research, 37, 2889-2900.

Montzka, C., Moradkhani, H., Weihermüller, L., Hendricks Franssen, H.-J., Canty, M., Vereecken, H. (2011). Hydraulic parameter estimation by remotely-sensed top soil moisture observations with the particle filter. Journal of Hydrology, 399, 410-421.

Moradkhani, H., Sorooshian, S., Gupta, H.V., Houser.P.R.. (2005). Dual state–parameter estimation of hydrological models using ensemble Kalman filter. Advances in Water Resources, 28, 135–147.

Mougin, E., Hiernaux, P., Kergoat, L., Grippa, M., De Rosnay, P., Timouk, F., Le Dantec, V., Demarez, V., Lavenu, F., Arjounin, M., Lebel, T., Soumaguel, N., Ceschia, E., Mougenot, B., Baup, F., Frappart, F., Frison, P.-L., Gardelle, J., Gruhier, C., Jarlan, L., Mangiarotti, S., Sanou, B., Tracol, Y., Guichard, F., Trichon, V., Diarra, L., Soumaré, A., Koité, M., Dembele, F., Lloyd, C. R., Hanan, N. P., Damesin, C., Delon, C., Serça, D., Galy-Lacaux, C., Seghieri, J., Becerra, S., Diarra, B., Gangneron, F., Mazzega, P.. (2009). The AMMA-CATCH Gourma observatory site in Mali: Relating climatic variations to changes in vegetation, surface hydrology, fluxes and natural resources. Journal of Hydrology, 375. 14–33.

Nair, R.R.K. (2007). Optimization of polarization and incidence angles configuration for estimation of surface roughness in sloping areas using ENVISAT-1 ASAR data. Master thesis, Enschede, ITC.

Nguyen, H., Thorncroft, C. D., Zhang, C. (2011). Guinean coastal rainfall of the West African Monsoon, Q.J.R. Meteorol. Soc., 137, 1828–1840, doi: 10.1002/qj.867.

Nobel., P.S.. (1999). Physicochemical and environmental plant physiology. San Diego: Academic Press, 474.

Noilhan, J., Lacarrère, P.. (1995). GCM gridscale evaporation from mesoscale modeling. Journal of Climate, 8(2), 206-223.

Noilhan, J., Mahfouf, J.F. (1996). The ISBA land surface parameterization scheme. Global and Planetary Change, 13, 145-159.

Noilhan, J., Planton, S. (1989). A simple parameterization of land surface processes for meteorological models. Monthly Weather Review, 117, 536-549.

Norman, J.M., Kustas, W.P., Humes, K.S. (1995). A two-source approach for estimating soil and vegetation energy fluxes in observations of directional radiometric surface temperature. Agricultural and Forest Meteorology, 77, 263–93

Oke, P.R., Sakov, P., Corney, S. P. (2007). Impacts of localisation in the EnKF and EnOI: experiments with a small model. Ocean Dynamics. 57(1): 32-45. DOI: doi:10.1007/s10236-006-0088-8.

Olioso, A., Jacob, F., Hadjar, D., Lecharpentier, P. Hasager, C.B. (2002). Spatial distribution of evapotranspiration and aerodynamic roughness from optical remote sensing. In: Herman Debie & Koen de.

Ohmura, A..(1982). Objective criteria for rejecting data for Bowen ratio flux calculations.American Meteorological Society. 21, 595-598.

Pauwels, V.R.N., Verhoest, N.E.C., de Lannoy, G.J.M., Guissard, V., Lucau, C., Defourny, P.. (2007). Optimization of a coupled hydrology-crop growth model through the assimilation of observed soil moisture and leaf area index values using an ensemble Kalman filter. Water Resour. Res., 43, doi:10.1029/2006WR004942.

Pellarin, T., Laurent, J.-P., Decharme, B., Descroix, L., Cappelaere, B.. (2009). Hydrological modelling and associated microwave emission of a semi-arid region in South-western Niger. Journal of Hydrology. vol. 375, 1-2, 262-272.

Perez, P.J., Castellvi, F., Ibañez, M., Rosell. J.I. (1999). Assessment of reliability of Bowen ratio method for partitioning fluxes. Agricultural & Forest Meteorology, 97, 141–150.

Peugeot, C., Guichard, F., Bock, O., Bouniol, D., Chong, M., Boone, A., Cappelaere, B., Gosset, M., Besson, L., Lemaître, Y., Séguis, L., Zannou, A., Galle, S. and Redelsperger, J.-L.. (2011). Mesoscale water cycle within the West African Monsoon. Atmosph. Sci. Lett., 12: 45–50. doi: 10.1002/asl.309.

Pollacco, J.A.P. Mohanty, B.P.. 2012. Uncertainties of water fluxes in soil-vegetation-atmosphere transfer models: Inverting surface soil moisture and evapotranspiration retrieved from remote sensing. Vadose Zone J., doi:10.2136/vzj2011.0167.

Qin, J., Liang, S., Yang, K., Kaihotsu, I., Lui, R., Koike, T.. (2009). Simultaneous estimation of both soil moisture and model parameters using particle filtering method through the assimilation of microwave signal. Journal of Geophysical Research, 14, D15103. Doi:10.1029/2008JD011358.

Rahman, M.M., Moran, M.S.,Thoma, D.P., Bryant, R., Sano, E.E., Holifield Collins, C.D., Skirvin,S., Kershner, C., Orr, B.J. (2007). A derivation of roughness correlation length for parameterizing radar backscatter models. International Journal of Remote Sensing., 28, 3995-4012.

Ramier, D., Boulain, N., Cappelaere, B., Timouk, F., Rabanit, M., Lloyd, C. R., Boubkraoui, S., Métayer, F., Descroix, L., Wawrzyniak, V.. 2009. Towards an understanding of coupled physical and biological processes in the cultivated Sahel – 1. Energy and water. Journal of Hydrology, 375. 204–216.

Prueger, J.H., Kustat, W., Hipps, L.E., Hatfield. J. L.. (2004). Aerodynamic parameters and sensible heat flux estimates for a semi-arid ecosystem. J. of Arid Environments. 57, 87-100.

Reichle, R. H. (2008). Data assimilation methods in the Earth sciences, Advances in Water Resources, Vol. 31(11), 1411-1418, 10.1016/j.advwatres.2008.01.001.

Reichle, R. H., Koster, R. D..(2004). Bias reduction in short records of satellite soil moisture. Geophys Res Lett 2004;31:L19501. doi:10.1029/2004GL020938.

Reichle, R. H., Koster, R. D., Liu, P., Mahanama, S. P. P., Njoku, E. G., Owe. M. (2007). Comparison and assimilation of global soil moisture retrievals from the Advanced Microwave Scanning Radiometer for the Earth Observing System (AMSR-E) and the Scanning Multichannel Microwave Radiometer (SMMR), J. Geophys. Res., 112, D09108, doi:10.1029/2006JD008033.

Reichle, R., McLaughlin, D., Entekhabi, D.. (2002). Data assimilation using an ensemble Kalman filter technique, Mon. Weather Rev., 129, 123– 137.

Richter, K., Timmermans, J.. (2009). Physically based retrieval of crop characteristics for improved water use estimates. Hydrol. Earth Syst. Sci., 13, 663–674.

Sabater, J.M., Rudiger, C., Calvet, J.C., Fritz, N., Jarlan, L., Kerr, Y.. (2008). Joint assimilation of surface soil moisture and LAI observation into a land surface model. Agric. For. Meteorol., 148, 1362-1373.

Sakov, P., Oke, P.R. (2008). A deterministic formulation of the ensemble kalman filter:an alternative to ensemble sqaure root filters. Tellus. 60A, 361-371.

Sakov, P., Evensen,G., Bertino, L.. (2010). Asynchronous data assimilation with the EnKF. Tellus A 62:1, 24-29Asynchronous data assimilation with the EnKF. Tellus A 62:1, 24-29.

Saleh, K., Wigneron, J.-P., de Rosnay, P., Calvet, J.-C., Escorihuela, M. J., Kerr, Y., Waldteufel, P.. (2006). Impact of rain interception by vegetation and litter on the L-band emission of natural grasslands (SMOSREX Experiment), Remote Sensing of Environment, 101, 127 – 139.

Sano, E.E.; Huete, A.R.; Moran, M.S. Estimation of surface roughness in a semiarid region from C-band ERS-1 synthetic aperture radar data. Revista Brasileira de Ciencia do Solo. 1999, 23,903-908.

Satalino, G.; Mattia, F.; Davidson, M.; Le Toan, T.; Pasquariello, G.; Borgeaud, M. On current limits of soil moisture retrieval from ERS-SAR data. IEEE Trans. Geosci. Remote Sens. 2002, 40, 2438-2447, doi: 10.1109/TGRS.2002.803790.

Saux-Picart, S., Ottlé, C., Decharme, B., André, C., Zribi, M., Perrier, A., Coudert, B., Boulain N., Cappelaere, B., Descroix, L., Ramier, D. (2009). Water and energy budgets simulation over the AMMA-Niger super-site spatially constrained with remote sensing data. Journal of Hydrology, 375, 287-295.

Scanlon,T.M.,Albertson,J.D., Kustas,W.P. (2001). Scale effects in estimating large eddy-driven sensible heat fluxes over heterogenous terrain. Remote sensing and Hydrology 2000 (Proceedings of a symposium held at Santa Fe, USA,April 2000). IAHS Publ.no.267.

Schaap, M. G., Leij, F. J., van Genuchten, M. Th. (1998). Neural Network Analysis for Hierarchical prediction of Soil Hydraulic Properties, Soil Sci. Soc. Am. J, 62, 847– 855.

Scheel, M. L. M., Rohrer, M., Huggel, Ch., Santos Villar, D., Silvestre, E., Huffman, G. J. (2011). Evaluation of TRMM Multi-satellite Precipitation Analysis (TMPA) performance in the Central Andes region and its dependency on spatial and temporal resolution, Hydrol. Earth Syst. Sci., 15, 2649-2663, doi:10.5194/hess-15-2649-2011.

Schlenz, F., dall'Amico, J. T., Mauser, W., Loew, A.. (2012). Analysis of SMOS brightness temperature and vegetation optical depth data with coupled land surface and radiative transfer models in Southern Germany, Hydrol. Earth Syst. Sci., 16, 3517-3533, doi:10.5194/hess-16-3517-2012.

Scipal, K. (2002). Global Soil Moisture Retrieval from ERS Scatterometer Data. Ph.D. Thesis.

Séguis, L., Boulain, N., Cappelaere, B., Cohard, J.M., Favreau, G., Galle, S., Guyot, A., Hiernaux, P., Mougin, É., Peugeot, C., Ramier, D., Seghieri, J., Timouk, F., Demarez, V., Demarty, J., Descroix, L., Descloitres, M., Grippa, M., Guichard, F., Kamagaté, B., Kergoat, L., Lebel, T., Le Dantec, V., Le Lay, M., Massuel, S. and Trichon, V.. (2011). Contrasted land-surface processes along the West African rainfall gradient. Atmosph. Sci. Lett., 12: 31–37. doi: 10.1002/asl.327.

Sellers, P.J., Heiser, M.D., Hall, F.G. (1992). Relations between surface conductance and spectral vegetation indices at intermediate (100 m2 to 15 km2) length scales. J. Geophys. Res.., 97 (D17),19033–19059.

Shi, J.C., Wang, J., Hsu, A.Y., O′Neill, P.E., (1997). Engman, E.T. Estimation of bare surface Soil moisture and surface roughness parameter using L-Band SAR image data. IEEE Trans. Geosci. Remote Sens., 35,1254-1266.

Shin, D. B. (2011). Spatial information of high-frequency brightness temperatures for passive microwave rainfall retrievals. International Journal of Remote Sensing: 32(19).

Soet, M., Stricker, J. (2003). Functional behaviour of pedotransfer functions in soil water flow simulation, Hydrol. Processes, 17, 1659–1670.

Srivastava, H.S., Patel, P., Manchanda, M.L., Adiga, S. (2003). Use of multi-incidence angle RADARSAT-1 SAR data to incorporate the effects of surface roughness in soil moisture estimation. IEEE Trans. Geosci. Remote Sens. 41, 1638-1640.

Su, Z. (2002). The Surface Energy Balance System (SEBS) for estimation of turbulent heat fluxes. Hydrol. Earth Syst. Sci., 6, 85-99.

Su,Z.(2005) Estimation of the Surface Energy Balance. Encyclopedia of Hydrological Sciences. John Wiley & Sons, Ltd.

Su, Z., Schmugge, T., Kustas, W.P., Massman, W.J., (2001). An evaluation of two models for estimation of the roughness height for heat transfer between the land surface and the atmosphere. Journal of Applied Meteorology, 40, 1933-1951.

Su, Z., Troch, P.A., de Troch, F.P. (1997). Remote sensing of bare surface soil moisture using EMAC/ESAR data. International Journal of Remote Sensing. 35,1254–1266.

Su, Z., Wen, J., Dente, L., van der Velde, R., Wang, L., Ma, Y., Yang, K., Hu, Z. (2011).TheTibetan Plateau observatory of plateau scale soil moisture and soil temperature (Tibet-

Obs) for quantifying uncertainties in coarse resolution satellite and model products. Hydrology and Earth System Sciences. 2011, 15, 2303–2316.

Sun, J.. (1999). Diurnal variations of thermal roughness height over a grassland. Boundary-Layer Meteorology., 92, 407–427.

Sun, F., Ma, Y., Ma, W., Li, M..(2006). One observational study on atmospheric boundary layer structure in Mt. Qomolangma region, Plateau Meteorology, 25(6), 1014–1019.

Sun, F., Ma, Y., Li, M., Ma, W., Tian, H., and Metzge, S. (2007). Boundary layer effects above a Himalayan valley near Mount Everest, Geophys. Res. Lett., 34.

Sun, A. Y., Morris, A., Mohanty, S. (2009). Comparison of deterministic ensemble kalman flters for assimilating hydrogeological data. Adv. Water Resour., 32, 280-292.

Taconet, O., Vidal-Madjar, D., Emblanch, Ch., Normand, M. (1996). Taking into account vegetation effects to estimate soil moisture from C-band radar measurements, Remote Sens. Environ., 56, 52-56.

Taylor, C. M., Parker, D. J., Kalthoff, N., Gaertner, M. A., Philippon, N., Bastin, S., Harris, P. P., Boone, A., Guichard, F., Agusti-Panareda, A., Baldi, M., Cerlini, P., Descroix, L., Douville, H., Flamant, C., Grandpeix, J.Y., Polcher, J.. (2011). New perspectives on land–atmosphere feedbacks from the African Monsoon Multidisciplinary Analysis. Atmosph. Sci. Lett., 12: 38–44. doi: 10.1002/asl.336.

Timmermans, J., van der Tol, C, A. Verhoef, W. Verhoef, Z. Su, M. van Helvoirt, L. Wang. (2011) Quantifying the uncertainty in estimates of surface- atmosphere fluxes through joint evaluation of the SEBS and SCOPE models. Hydrol. Earth Syst. Sci. Discuss., 8, 2861-2893.

Tsuanga, B.J., Tsaia, J.L., Lina, M.D., Chen.C.L.. (2003). Determining aerodynamic roughness using tethersonde and heat flux measurements in an urban area over a complex terrain. Atmospheric Environment, 37, 1993–2003.

Ulaby, F.T., Batlivala, P.P. (1976). Optimum radar parameters for mapping soil moisture. IEEE Trans.Geosci. Remote Sens., 14, 81-93.

Ulaby, F.T., Moore, R.K., Fung, A.K. (1982).Microwave Remote Sensing: Active and Passive Volume II: Radar Remote Sensing and Surface Scattering and Emission Theory. Artech House Publishers: Norwood MA; 608.

van der Tol, C., van der Tol, S., Verhoef, A., Su, Z., Timmermans, J., Houldcroft, C. Gieske, A.S.M. (2009). A Bayesian approach to estimate sensible and latent heat over vegetated land surface. Hydrol. Earth Syst. Sci., 13, 749-758.

van der Velde, R.(2010). Soil moisture remote sensing using active microwaves and land surface modeling. Ph.D. thesis.

van der Velde, R., Su, Z., Ek, M. Rodell, M., Ma., Y. (2009). Influence of thermodynamic soil and vegetation parameterizations on the simulation of soil temperature states and surface fluxes by the Noah LSM over a Tibetan Plateau site. Hydrol. Earth Syst. Sci. Discuss., 6, 455-499.

van der Velde, R., Su, Z., van Oevelen, P., Wen, J., Ma, Y., Salama, M.S. (2012). Soil moisture mapping over the central part of the Tibetan Plateau using a series of ASAR WS images. Remote Sens. Environ. 120, 175-187.

Verhoest, N.E.C., De Baets, B., Mattia, F., Satalino, G., Lucau, C., Defourny, P. (2007). A possibilistic approach to soil moisture retrieval from ERS synthetic aperture radar backscattering under soil roughness uncertainty. Water Resour. Res. 43, W07435-WR005295.

Verhoest, N.E., Lievens, H., Wagner, W., Á lvarez-Mozos, J., Moran, M.S., Mattia, F. 2008. On the Soil Roughness Parameterization Problem in Soil Moisture Retrieval of Bare Surfaces from Synthetic Aperture Radar. Sensors. 8, 4213-4248.

Vrugt, J., Robinson, B.A., Vesselinov, V. 2005. Improved inverse modeling for flow and transport in subsurface media: Combined parameter and state estimation. Geophysical Research Letter, 13, L18408. Doi:10.1029/2009GL023940.

Wang, D., Y. Chen, X. Cai. (2009). State and parameter estimation of hydrologic models using the constrained ensemble Kalman filter, Water Resour. Res., 45, W11416, doi:10.1029/2008WR007401.

Weaver, H. L.. (1990). Temperature and humidity flux-variance relations determined by one-dimensional eddy correlation. Bound. Layer Meteor., 53, 77–91.

Wen, L., Cui, P., Li, Y., Wang, C., Liu, Y., Chen, N., Su, F. (2010).The influence of sensible heat on Monsoon precipitation in central and eastern Tibet. Meteorological Applications. 17, 452-462.

Verhoest, N.E., Lievens, H., Wagner, W., Á lvarez-Mozos, J., Moran, M.S., Mattia, F. (2008).On the Soil Roughness Parameterization Problem in Soil Moisture Retrieval of Bare Surfaces from Synthetic Aperture Radar. Sensors. 8, 4213-4248.

Wieringa, J. (1992). Updating the Davenport roughness classification, J. Wind Eng. Ind. Aerodyn. 41-44, 357-368.

Wigneron, J. P., Chanzy, A., Kerr, Y. H., Lawrence, H., Shi, J. C., Escorihuela, M. J., Mironov, V., Mialon, A., Demontoux, F., de Rosnay P., Saleh-Contell, K.. (2011). Evaluating an improved parameterization of the soil emission in L-MEB. IEEE Transactions on Geoscience and Remote Sensing 49(4): 1177-1189.

Wigneron, J. P., Kerr, Y. H., Chanzy, A., Jin, Y. Q. (1993). Inversion of surface parameters from passive microwave measurements over a soybean field, Remote Sens. Envir., 46, 61-72.

Wigneron, J. P., Kerr, Y., Waldteufel, P., Saleh, K., Escorihuela, M. J., Richaume, P., Ferrazzoli, P., de Rosnay, P., Gurney, R., Calvet, J. C., Grant, J. P., Guglielmetti, M., Hornbuckle, B., Matzler, C., Pellarin, T., Schwank, M. (2007). L-band microwave emission of the biosphere (L-MEB) model: Description and calibration against experimental data sets over crop fields, Remote Sens. Envir, 107(4), 639-655.

Whitaker, J.S., Hamill, T.M.. (2002). Ensemble data assimilation without perturbed observations. Mon. Wea. Rev. 132,1590-1605.

World Food Program. (2010). Hunger Crisis Deepens In Africa's Sahel Region. News. http://www.wfp.org/stories/hunger-season-looms-over-africa%E2%80%99s-sahel-region. Accessed on March 14, 2013.

Yang, P., Chen, Z., Zhou, Q., Zha, Y., Wu, W., Shibasaki, R.. (2006). Comparisons of MODIS LAI products and LAI estimates derived from Landsat TM. IEEE.

Yang, K., Koike, T., Yang, D.(2003). Surface flux parameterization in the Tibetan plateau. Boundary-Layer Meteorology. 116, 245-262.

Yang, K., Koike, T., Ishikawa, H., Kim, J. , Li., X. (2008). Turbulent flux transfer over bare-soil surfaces: Characteristics and parameterization. Journal of Applied Meteorology and Climatology. 47, 276.

Yao, Y., Liu, Q., Liu, Q., Li., X. (2008). LAI retrieval and uncertainty evaluations for typical low-planted crops at different growth stages. Remote Sensing of Environment. 112, 94–106.

Yuter, S. E., Stout, J., Wood, R., Kwiatkowski, J., Horn, D. (2005). Relative errors in TRMM satellite Version 5 and Version 6 products: Steps forward and backward. The 32st Conference on Radar Meteorology, American Meteorological Society, Albuquerque, NM, 24-29 October.

Zhang, S., Anderson J. L.. (2003). Impact of spatially and temporally varying estimates of error covariance on assimilation in a simple atmospheric model. Tellus , 55A, 126–147.

Zhou, H.. (2011). Stochastic inverse methods to identify non-Gaussian model parameters in heterogeneous aquifers, PhD thesis, University of Valencia, Spain.

Zribi, M., Dechambre, M. (2003). An new empirical model to retrieve soil moisture and roughness from Radar Data, Remote Sensing of Environment, Vol. 84, no. 1, 42-52.

Zribi, M., Pardé, M., De Rosnay, P., Baup, F., Boulain, N., Descroix, L., Pellarin, T., Mougin, E., Ottlé, C., Decharme. B..(2009). ERS Scatterometer surface soil moisture analysis of two sites in the south and north of the Sahel region of West Africa, Journal of Hydrology, vol. 375, 1-2, 253-261.